EPFL

Thèse n° 8584

# ON THE DESIGN AND OPTIMIZATION OF WIDE ANGLE DIFFRACTIVE OPTICAL ELEMENTS

Présentée le 1er février 2021

Faculté des sciences et techniques de l'ingénieur
Laboratoire de nanophotonique et métrologie
Programme doctoral en photonique

pour l'obtention du grade de Docteur ès Sciences

par

**Dong Cheon KIM**

Acceptée sur proposition du jury

Prof. C. Moser, président du jury
Dr T. Scharf, directeur de thèse
Dr A. Hermerschmidt, rapporteur
Prof. M. Beyerlein, rapporteur
Prof. H. P. Herzig, rapporteur

École polytechnique fédérale de Lausanne

2021

# Acknowledgements

This PhD project was made possible by a cooperation between École Polytechnique fédérale de Lausanne (EPFL) and Holoeye Photonics AG within the framework of the NOLOSS European Union (EU) project. Naturally, such a collaborative project involves many parties, I have plenty of people to thank for their support in making this project successful.

First and foremost, I would like to express my deep gratitude towards my thesis supervisor Dr. Toralf Scharf for giving me the opportunity to do a PhD thesis and guiding me through the whole PhD process. It has been a great honor to work with him over the last four years, he has encouraged me to settle in new field, i.e., micro-optics while also enabling the application of my background to this work.

I have spent the first six months and the last part of my PhD at Nanophotonics and Metrology Laboratory of EPFL. I am grateful to the head of the group Prof. Olivier Martin and group members for the warm welcome and all supports. I would like to acknowledge my colleagues at the NAM for the friendly interactions inside and outside of work as well as the great collaboration on teaching duties, especially thank Mintae Chung and Jeonghyeon Kim for measuring the SEM images, Dr. Kevin Müller for discussing the basis of adjoint method, (Dr.) Maryam Yousefi and (Dr.) Alessandro Grosso and Debdatta Ray for sharing nice office life, Dr. Karim Achouri for correcting the abstract of thesis, Mrs. Beatrice Raball and Mrs. Cathy Buchs for all administrative supports.

Within the corporate Holoeye Photonics AG, my supervisors were Dr. Andreas Hermerschmidt and Dr. Pavel Dyachenko. I owe them great thanks not only for the guidance and friendly work atmosphere but also for mentoring me for over 2 years and for continuing to support me to finish all publications as well as this thesis. I am grateful to Sven Plöger for all the technical supports on measuring the optical properties of samples and to Mika Gornig for administrative supports and to everyone else at corporate for their warm welcome.

I would like to express my appreciation to the members of the thesis committee, Prof. Hans Peter Herzig, Prof. Mathias Beyerlein, Dr. Andreas Hermerschmidt, and Prof. Christophe Moser for their time and efforts. Their questions and remarks have allowed me to improve my thesis.

I very much appreciated working in the framework of the NOLOSS project and I would like to thank again Dr. Toralf Scharf for organizing NOLOSS project as well as 15 fellows for the constructive discussions and workshops that we shared.

I would like to thank my friends who have made my life happy and enjoyable. It includes the Kyung-Hee squad (Jiho Yoon, Wonjong Kim, Heetae Park, Jejune Park) who have studied

together in Ecole Polytechnique, the Korean squad at EPFL, my friends in LMSC and LMGN, and the people from the Somang Gemeinde in Berlin. I especially thank Lucas Güniat for inviting nice parties, helping my moving, and correcting the abstract of my thesis.
Finally, I would strongly like to thank my wife Min Kyeong Jo, my parents, my brother, and parents-in-law for their unconditional support. Their encouragements and patience were vital in completing this thesis.

**Funding**: This research has been funded by the EU's Horizon 2020 research and innovation programme under the Marie Skłodowska-Curie grant agreement No. 675745.

*Lausanne, January 7, 2021* D. C. Kim

# Abstract

Diffractive optical elements (DOEs) which consist of microstructure surface relief permit the generation of the spatial distribution of light beams by using a single element. Due to their compact size, design flexibility, and mass productivity, they are used for a variety of applications, from optical metrology to biotechnology. However, the required wide angle DOEs have been elusive due to design challenges. Conventional design approaches such as iterative Fourier transform algorithm (ITFA) fail when applied to DOEs containing very small features or nanostructures. But it is exactly the small features that are required to create high performance wide diffraction angle diffractive optics. This thesis aims to extend the range of DOEs applications by developing designing and optimization algorithms for wide angle DOEs which is far beyond the limits of scalar paraxial diffraction model such as thin element approximation (TEA).

The development of inverse design, where computational optimization techniques are used to find the geometry needed for the desired functionality, has led to the discovery of superior and non-intuitive design. Among various approaches, gradient-based optimization methods have been one of the most important techniques to obtain the optimal structure described by a huge number of design variables. These methodologies are made possible when the gradient of a merit function with respect to all design parameters efficiently enables to be calculated. Here, two approaches are considered: optimization based on the step transition perturbation approach and the adjoint-state method.

The step transition perturbation approach (STPA) is based on the evaluation of local field perturbations due to sharp surface profile transitions. When we used the positions of transition points as design parameters in DOEs, it facilitates describing an analytical solution of the gradient of diffraction efficiency with respect to the positions of transition points. The gradient-based optimization with STPA creates various one-dimensional diffractive beam splitters generating wide angle spot arrays. The results of the experimental characterization confirm that this optimization tool is valid for wide angle DOEs.

We discuss the adjoint method with rigorous electromagnetic theory, for example, rigorous coupled-wave analysis (RCWA), to optimize the DOEs with small features for generating even wider angles. Due to the adjoint method, we can compute the gradient of the objective function with respect to all design parameters efficiently even using a rigorous electromagnetic calculation. Hence, the permittivity distribution in the geometry of DOEs is used as the design variable during the optimization. This method also is able to account for application-dependent target functions while ensuring compatibility with existing fabrication processes.

**Abstract**

Thus we design the various wide angle DOEs including two-dimensional diffractive beam splitters by adjoint method. The results of the experimental characterization confirm that this optimization tool is valid in wide angle beam splitters creating a square spot array with maximal diffraction angle up to 53° from the center to diagonal edges, which is far beyond the limit of any scalar paraxial diffraction regime.

**Keywords**: Diffractive optical element, diffractive beam splitter, fan-out grating, gradient-based optimization, inverse design, adjoint method, rigorous coupled-wave analysis, step transition perturbation approach.

# Résumé

Les éléments optiques diffractifs (EODs) sont des éléments à l'échelle micrométrique qui, ensemble, constituent un relief microstructuré permettant de générer une distribution spatiale des faisceaux lumineux. En raison de leur petite taille, de leur facilité de fabrication et de leur potentiel à être produits en masse, ils sont utilisés pour diverses applications allant de la métrologie optique à la biotechnologie. Toutefois, maints domaines requièrent des EODs grand angle, dont la conception pose encore plusieurs soucis. Les approches conventionnellement utilisées pour fabriquer des EODs, comme l'algorithme itératif de transformée de Fourier (ITFA -"Iterative Fourier transform algorithm"), échouent lorsqu'elles sont appliquées à des EODs grand angle : en effet, ces algorithmes sont inutiles pour l'élaboration d'éléments nanométriques nécessaires à la création d'optiques à grand angle de diffraction. Cette thèse vise à étendre la gamme d'applications des EODs en développant des algorithmes de conception et d'optimisation pour les EODs grand angle. Ces algorithmes ont pour but de dépasser les limites des modèles de diffraction paraxiale scalaire actuels, comme celui de l'approximation par éléments minces (TEA - "Thin element approximation").

Le développement de méthodes inverses, pour lesquelles des techniques d'optimisation permettent d'établir une géométrie optimale ayant les fonctionnalités désirées, nous a permis de découvrir des géométries fortement contre-intuitives, mais très performantes. Parmi les diverses approches utilisées, la méthode par gradient a été l'une des plus adaptées pour obtenir une géométrie optimale remplissant les nombreux critères de conception. La clé de ces méthodes est de calculer efficacement le gradient d'une fonction de mérite par rapport à toutes les variables de conception. Dans ce projet, nous envisageons deux approches différentes, à savoir : une méthode d'optimisation basée sur la " step-transition perturbation approach (STPA)" et la "adjoint state method (ASM)".

La STPA est basée sur l'évaluation des perturbations locales du champ électromagnétique dues à des transitions nettes de surface. Lorsque nous utilisons les positions des points de transition comme paramètres de conception dans les EODs, cela facilite la description d'une solution analytique du gradient d'efficacité de diffraction par rapport aux positions des points de transition. L'optimisation basée sur le gradient avec la STPA permet de créer divers séparateurs de faisceaux diffractifs unidimensionnels générant des réseaux de spots à grand angle. Les résultats de la caractérisation expérimentale confirment que cet outil d'optimisation est efficace pour le design d'EODs grand angle.

Dans cette thèse nous combinons également l'ASM avec des méthodes électromagnétiques rigoureuses, comme par exemple, l'analyse rigoureuse des ondes couplées (RCWA-"Rigorous

coupled-wave analysis"), pour optimiser les EODs avec de petites structures afin de générer des angles encore plus grands. Grâce à l'ASM, nous pouvons calculer efficacement le gradient de la fonction objectif par rapport à tous les paramètres de conception, même en utilisant un calcul électromagnétique rigoureux. Ainsi, nous utilisons la valeur de la permittivité comme variable pour l'optimisation de la géométrie des EODs.
Cette méthode permet également de prendre en compte diverses fonctions objectives pour une application spécifique tout en assurant la compatibilité avec les procédés de fabrication existants. Ceci nous a permis de concevoir différents EODs grand angle, y compris des séparateurs de faisceaux diffractifs bidimensionnels. Les résultats expérimentaux confirment que l'ASM fonctionne pour les diviseurs de faisceau à grand angle. Cette méthode nous a ainsi permis de créer un réseau de points carrés avec un angle de diffraction maximal allant jusqu'à 53° du centre aux bords diagonaux, ce qui est bien au-delà de la limite de tout régime de diffraction scalaire paraxiale.

**Mots-clés** : Éléments optiques diffractifs, séparateur de faisceau diffractif, réseau de diffraction en éventail, optimisation basée sur le gradient, conception inverse, adjoint method, rigorous coupled-wave analysis, step transition perturbation approach.

# Zusammenfassung

Diffraktive optische Elemente (DOE), die aus einem mikrostrukturellen Oberflächenrelief bestehen, ermöglichen die Erzeugung der räumlichen Verteilung von Lichtstrahlen indem ein einzelnes Element zu verwenden. Aufgrund ihrer kompakten Größe, Gestaltungsflexibilität und Massenproduktivität werden sie für eine Vielzahl von Anwendungen eingesetzt, von der optischen Messtechnik bis zur Biotechnologie. Die benötigten Weitwinkel-DOE waren jedoch aufgrund von Design-Herausforderungen schwer zu realisieren. Konventionelle Designansätze wie der « iterative Fourier transform algorithm (ITFA) » versagen, wenn sie auf DOE angewendet werden, die sehr kleine Merkmale oder Nanostrukturen enthalten. Es sind aber genau diese kleinen Strukturen, die benötigt werden, um hochleistungsfähige diffraktive Optiken mit großem Beugungswinkel zu erzeugen. Diese Arbeit zielt darauf ab, den Anwendungsbereich von DOE zu erweitern, indem Design- und Optimierungsalgorithmen für DOE mit großem Beugungswinkel entwickelt werden, die weit über die Grenzen des skalaren paraxialen Beugungsmodells wie z.B. der « thin element approximation (TEA) » hinausgehen. Die Entwicklung des inversen Designs, bei dem computergestützte Optimierungstechniken zum Auffinden der für die gewünschte Funktionalität erforderlichen Geometrie eingesetzt werden hat zur Entdeckung eines überlegenen und nicht-intuitiven Designs geführt. Unter verschiedenen Ansätzen waren gradientenbasierte Optimierungsmethoden eine der wichtigsten Techniken zum Erhalt der optimalen Struktur, die durch eine große Anzahl von Designvariablen beschrieben wird. Diese Methodologien werden ermöglicht, wenn der Gradient einer Merit-Funktion in Bezug auf alle Designparameter effizient berechnet werden kann. Hier werden zwei Ansätze betrachtet: die Optimierung basierend auf dem « step-transition perturbation approach (STPA) » und « Adjoint state method (ASM) ».

Der STPA basiert auf der Auswertung von lokalen Feldstörungen aufgrund von scharfen Oberflächenprofilübergängen. Wenn wir die Positionen der Übergangspunkte als Designparameter in DOE verwenden, erleichtert dies die Beschreibung einer analytischen Lösung des Gradienten der Beugungseffizienz in Bezug auf die Positionen der Übergangspunkte. Die gradientenbasierte Optimierung mit STPA erzeugt verschiedene eindimensionale diffraktive Strahlteiler, die weitwinklige Punktraster erzeugen. Die Ergebnisse der experimentellen Charakterisierung bestätigen, dass dieses Optimierungswerkzeug für Weitwinkel-DOE gültig ist.

Wir diskutieren die ASM mit der rigorosen elektromagnetischen Theorie, z. B. der « rigorous coupled-wave analysis (RCWA) », um zur Erzeugung des noch größeren Winkels anhand von kleinen Merkmalen die DOE zu optimieren. Bei der ASM können wir mit einer rigorosen elek-

tromagnetischen Berechnung den Gradienten der Zielfunktion in Bezug auf alle Designparameter effizient bestimmen. Daher wird die Permittivitätsverteilung in der Geometrie der DOE als Designvariable während der Optimierung verwendet. Die verschiedenen Weitwinkel-DOE, einschließlich zweidimensionaler diffraktiver Strahlteiler, wurden durch ein gradientenbasiertes Optimierungsverfahren auf der Grundlage einer ASM entworfen, das in der Lage ist, anwendungsabhängige Zielfunktionen zu berücksichtigen und gleichzeitig die Kompatibilität mit bestehenden Fertigungsprozessen zu gewährleisten. Die Ergebnisse der experimentellen Charakterisierung bestätigen, dass dieses Optimierungswerkzeug in Weitwinkel-Strahlteilern gültig ist, die ein quadratisches Punktraster mit maximalem Beugungswinkel bis zu 53° von der Mitte zu den diagonalen Kanten erzeugen, was weit jenseits der Grenze jedes skalaren paraxialen Beugungsregimes liegt.

**Stichwörter**: Diffraktives optisches Element, diffraktiver Strahlteiler, Fan-Out Gitter, gradientenbasierte Optimierung, inverses Design, adjoint state method, rigorous coupled wave analysis, step-transition perturbation approach.

# Contents

**Acknowledgements** **i**

**Abstract** **iii**

**1 Introduction** **1**
1.1 History and state-of-the-art . . . . . 1
1.2 Motivation . . . . . 4
1.3 Outline of thesis . . . . . 5

**2 Background** **7**
2.1 Electromagnetic theory of light . . . . . 7
2.2 Wave propagation . . . . . 9
2.2.1 Angular spectrum representation . . . . . 9
2.2.2 Rayleigh-Sommerfeld representation . . . . . 11
2.2.3 Paraxial approximation . . . . . 12
2.2.4 Fresnel representation . . . . . 13
2.2.5 Fraunhofer representation . . . . . 13
2.3 Thin element approximation . . . . . 14
2.3.1 Diffraction at binary gratings . . . . . 15
2.3.2 Limit of the TEA . . . . . 17
2.4 Rigorous coupled-wave analysis . . . . . 20
2.4.1 Historical overview . . . . . 20
2.4.2 Incident plane wave . . . . . 21
2.4.3 Floque-Bloch wave and Rayleigh expansion . . . . . 22
2.4.4 Fourier factorization . . . . . 23
2.4.5 Computation of Eigenmode . . . . . 24
2.4.6 Calculating the field distribution . . . . . 26
2.4.7 Truncation procedure . . . . . 27
2.5 Inverse design methods . . . . . 29
2.5.1 Evaluation of diffractive beam splitters . . . . . 29
2.5.2 Iterative Fourier transform algorithm . . . . . 30
2.5.3 Limitation of IFTA . . . . . 31
2.5.4 Gradient-based optimization . . . . . 32

**3 Optimization based on Perturbation Approach** **35**
3.1 Step transition perturbation approach . . . 35
3.1.1 Field perturbations . . . 36
3.1.2 Perturbations in the Fourier domain . . . 38
3.1.3 Diffraction efficiency . . . 39
3.2 Inverse design based on STPA . . . 40
3.3 Optimization results : one dimensional (1D) diffractive fan-out elements . . . 43
3.3.1 Initial design and parameters . . . 43
3.3.2 Objective function and evaluation . . . 45
3.3.3 Optimized performances . . . 45
3.3.4 Comparison with the gradient from RCWA . . . 48
3.3.5 Experimental results . . . 50
3.4 Discussion of optimization based on STPA . . . 52
3.4.1 The feature size and accuracy of optimization based on STPA . . . 52
3.4.2 Fabrication errors . . . 54
3.5 Summary . . . 56

**4 Optimization based on Adjoint State Method** **57**
4.1 Adjoint state method . . . 57
4.1.1 Mathematical introduction . . . 57
4.1.2 Adjoint method for diffractive optical elements . . . 58
4.2 Topology optimization . . . 60
4.3 Inverse design of 1D fan-out gratings . . . 63
4.3.1 Even-numbered spot array illuminator . . . 63
4.3.2 Optimization results . . . 64
4.4 Inverse design of 2D diffractive beam splitters . . . 66
4.4.1 Fan-out elements with uniform intensity distribution . . . 67
4.4.2 Fan-out elements with tailored intensity distribution . . . 71
4.4.3 Experimental results . . . 74
4.5 Summary . . . 77

**5 Conclusion** **79**
5.1 Summary . . . 79
5.2 Outlook . . . 80

**Publications** **83**

**Bibliography** **85**

**Curriculum Vitae** **97**

# 1 Introduction

This thesis include the material which is adapted with permission from [1] ©2020 Optical Society of America, from [2] ©2020 Walter de Gruyter GmbH, and from [3, 4] ©2020 SPIE, ©2019 SPIE .

During the past few decades, diffractive optical elements (DOEs) have gained a great deal of attention because of their high design flexibility, compact size, and mass production as well as relatively spatial invariant focusing behavior [5–13]. For example, DOEs have been used as beam shapers for laser welding and cutting, beam splitters for optical telecommunications couplers, pattern generators for machine vision, anti-fraud protection for security documents, and optical disc read-heads in DVD and Blue-ray. DOEs consist of surface reliefs with dimensions in micrometer ranges. The micro-structure permits the generation of a spatial distribution of light beams by modulating and transforming the amplitude and/or phase of the light propagated through them. However, traditional theory, which is the scalar paraxial diffraction model based on thin element approximation, is only valid for modeling small diffraction angle DOEs. Nowadays, wide diffraction angle DOEs are increasingly being used in a promising field of applications with recent developments in fabrication technology realizing nanoscale features. This leads to the need for new design algorithms to build and optimize DOEs operating in complex diffraction regimes beyond the scalar paraxial diffraction model. In this work, we propose the different design strategies based on the gradient based optimization to overcome the present limitations and realize wide diffraction angle DOEs.

## 1.1 History and state-of-the-art

Optics which is the study of light is one of the oldest fields of human inquiry: 'What is light?', 'What are its properties?', and 'how can we manipulate it?' Efforts to answer these enquiries date back a few thousand years. The ancient Greek philosophers well known to us such as Plato, Aristotle and Pythagoras, developed various theories of light. In Alexandria, the emerging center of learning after Greece's Golden Age, Euclid was one of the first to realize that light travels in straight lines [14]. In the following millennium, very little happened until

Ibn al-Haytham [15] who was an Arab physicist of the Islamic Golden Age wrote numerous books of Optics. Ibn al-Haytham was the first to explain that vision occurs when light reflects from an object and then passes to one's eyes.

Diffraction effect was first scientifically studied by Francesco Maria Grimaldi in 1665 [16]. Grimaldi had observed a gradual transition from light to dark at the boundary of the shadow of a small aperture illuminated by a light source. In $17^{th}$ century, during the Renaissance, there were some early attempts at a wave theory. Robert Hooke thought that light have a wave-like nature from observing the phenomenon of diffraction in colored films [17]. Christiaan Huygens developed a wave theory of light involving "wavelets" which is each point of a wavefront is a spherical source [18]. The wave model was also supported by Thomas Young [19] who performed the double slit experiment demonstrating interference of light, and by Augustin Fresnel [20] and François Arago [21] who extended Huygens' approach, and Gustav Kirchhoff [22] who developed strong mathematical basis of wave theory. From the work of many scientists over the decades, James Clerk Maxwell unified the known relationships between electric and magnetic fields in Maxwell's equation [23], which become the heart of the rigorous electromagnetic simulation.

The first mention of fabricated diffractive optical elements refers to the studies of David Rittenhouse in the late $18^{th}$ century [24]. Joseph von Fraunhofer independently introduced the idea of the diffraction grating for scientific applications in 1821 [25]. Since then, Lord Rayleigh, Arnold Sommerfeld, and many ohter contributors developed the theory and manufacture of diffraction gratings and used these in spectroscopic applications.

In 1948, the discovery of holography by Dennis Gabor opened up new possibilities for practical realization of DOEs [26, 27]. Gabor showed that an interference pattern was generated and written into a photographic plate using a coherent electron beam [28]. But the reconstructed object waves were poor visibility and low contrast due to lack of strong coherent light sources. With the invention of the laser, Emmett Leith and Juris Upatnieks recorded the first high quality holograms with an off-axis geometry, i.e. spatially filtering out the zeroth order [29]. A drawback of the optically recorded holography is the difficulty of producing arbitrary phase functions for the optical element. To circumvent this limitation, Adolf Lohmann and Byron Brown proposed computer generated holograms (CGHs) and fabricated them using ink as an amplitude absorbing material [30, 31]. It was soon realized that phase-only CGHs have high transmission efficiency [32, 33]. However, the CGHs with continuous profile are difficult to fabricate accurately so that fabricated elements performance are significantly degraded. Joseph W. Goodman showed that the fabrication introduced quantization of the phase and the amplitude in the hologram [34]. In order to optimize the reconstruction in the presence of quantization, new design algorithms were developed [35–41]. In addition, developments in microfabrication technology, e.g. direct laser writing [42, 43], diamond turning [44], Electron Beam Lithography [45] inspired a significant advances in the DOE and allowed for manufacturing structures with nanoscale feature sizes [46]. Owing to the developments in fabrication technology, DOEs generating wide-angle spot arrays are used in a promising field

of applications such as structured light projection [47, 48], and camera calibration [49].

As long as only small diffraction angles are required, the iterative Fourier transform algorithm (IFTA) [50–52] based on the thin element approach (TEA) [53, 54] is widely and successfully used for the design of the microstructure surface of the DOEs. However, when larger angles are required, this approach suffers from several severe shortcomings and effectively gets unusable. Among those shortcomings, the limited choice of diffraction angles and the geometric distortions can be corrected for most easily, and IFTA's computation scheme can be still be used with moderate extensions and modifications [55, 56]. A significantly more severe problem is the insufficient modeling of the light field transmission through the DOE by the TEA approximation [57, 58]. A precise modeling can be obtained only by rigorous electromagnetic diffraction theory, such as rigorous coupled-wave analysis (RCWA) [59–64].

This significantly increases the computation time, triggering efforts to improve the computation speed [65] and to find faster alternatives with similar accuracy [66]. However, for iterative computations schemes, a projection operator in the DOE domain for the far-field-adapted and back-propagated field is required, but cannot be derived in a similar manner using the rigorous electromagnetic methods.

Some groups employed genetic algorithms or gradient-based algorithms based on the finite-difference time-domain (FDTD) method to optimize the DOEs [67–69]. FDTD requires high computational effort and thus have been applied only to the one-dimensional domain. Parametric optimization is another option and was used for design and analysis of only two dimensional (2D) fan-out DOEs with low complexity, e.g. $3 \times 3$ array beam-splitters [70]. The correspondingly significantly larger number of parameters poses a practical limitation to parametric optimization for those scenarios due to resulting very large computational efforts also, even if such microstructures and corresponding initial parameters can be found at all.

Other design approaches recently combined a genetic algorithm with the RCWA method to design large-angle 2D fan-out DOEs [71, 72]. The experimental results of the fabricated DOEs verified the method is reliable, but the improvements were comparatively insignificant during the optimization so that the obtained elements still have a rather low performance with respect to uniformity error. Data-driven photonics inverse design approaches have also been investigated for binary fan-out DOEs in the non-paraxial domain, but again only for elements with low complexity [73].

In recent years, inverse design methods using the adjoint variable method [74–79], have attracted attention due to their successful application to the optimization of photonic devices. In the adjoint method, one can calculate the gradient with respect to a figure of merit based on only two rigorous simulations, no matter how many design parameters are utilized to describe the device. This approach resolves the mentioned problem of the missing projection operator for computational schemes in the non-paraxial domain.

In summary, DOEs has become mature over the last decades with scalar paraxial diffraction

model. Fabrication technology developments now enables manufacturing of wide diffraction angle DOEs (i.e., with nanoscale features), leading to the needs for new design methods.

## 1.2 Motivation

We require mathematical models for calculating the diffracted wave, and optimization algorithms based on these models to design the DOEs. The TEA-based IFTA has proved a powerful design approach that can easily be adapted for a variety of different design problems [80]. However, TEA does not take into account the actual physical process and it is only valid in the structures which are much bigger compared to the wavelength of incident wave. Some cases which have structures with feature sizes in the range of wavelength can still be described by TEA [41]. In general, the feature size is about 10 times greater than wavelength to ensure an accurate approximation [57, 81, 82]. This work aims to develop optimization tools for wide angle DOEs which required analysis of more complex diffraction regimes than TEA. We go beyond the limitations and realize the design and fabrication of new generations of DOEs for a wider range of applications.

To overcome the limitations, we used a rigorous electromagnetic approach, especially RCWA, in this work. This method is particularly well suited for the analysis of gratings due to periodic structure. However, the use of parametric optimization based on the rigorous analysis is often computationally heavy because the gratings with many parameters, especially 2D gratings are leading to high dimensional optimization problems. We thus introduce stable and fast design approach for wide angle DOEs using gradient-based algorithms based on two different methods: step-transition perturbation approach (STPA) and adjoint-variable method [74]. The STPA is an approximate method based on local field perturbations generated by sharp transitions of the surface profile of diffractive elements. We describe a design approach based on STPA for wide-angle DOEs in Chapter 3. Adjoint method allow to calculate the gradient of the figure of merit with respect to the design parameters efficiently even using rigorous diffraction theory. The implementation of adjoint method with RCWA is provided in Chapter 4.

In this work, we focus on diffractive beam splitters, often also referred to as fan-out gratings, as various applications use elements of this type from optical interconnects [83], multifocal microscopy [84, 85], camera calibration [86], optical system distortion measurement [87] to structured light projectors [48, 88] in which the spot array will be useful for the verification of diffraction efficiency. We also focus our efforts to designing binary (i.e. 2-level) microstructures because these are considerably easier to fabricate than multilevel or continuous-relief elements and thus obviously are very attractive for optical systems. Despite the advancement in lithography technologies, high cost and fabrication errors are inevitable for fabrication of multilevel gratings. A schematic of a binary fan-out grating creating 7 X 7 spot array is shown in Fig. 1.1. The grating period and the smallest feature size, i.e., critical dimension (CD) is represents in the inset. It is designed by TEA-based IFTA, not surprisingly the performance of the element become degraded when the grating is shrunk, i.e., the size of structures in the

gratings becomes comparable with the wavelength of the incident light. The diffraction angle is proportional to the ratio of the wavelength. Thus, we show new strategies to optimize wide angle diffractive optical elements in Fig. 1.1(b). We hope this framework for new inverse design methods contributes to improving design methods for various diffractive optical elements.

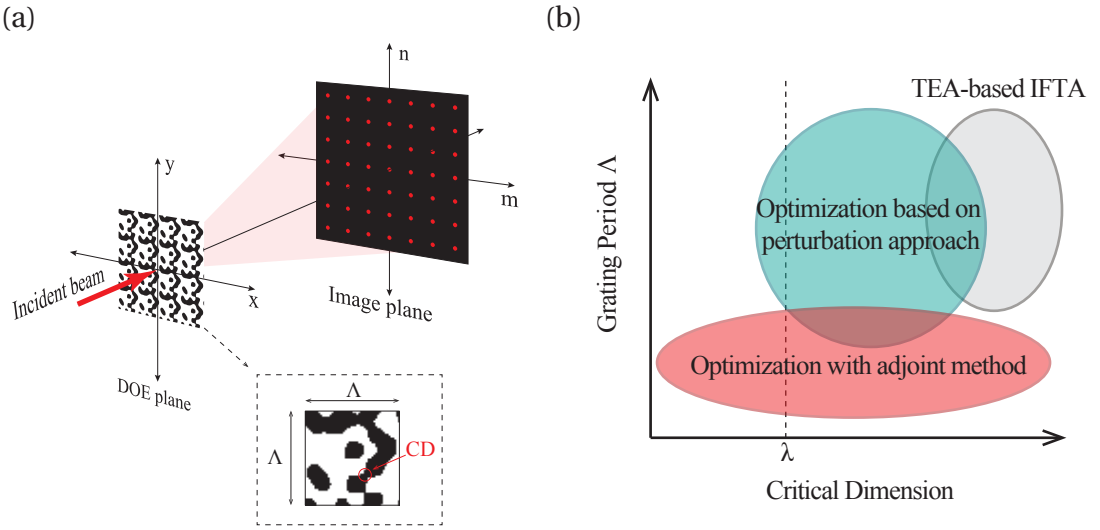


Figure 1.1 – (a) Scheme of two-dimension diffractive beam splitter generating 7 X 7 spot array designed by IFTA. The insets show the layout of the single unit cell with grating period Λ and critical dimension (CD). Black represents dielectric material and white represents air. (b) Validity region of different optimization methods in the domain of grating period and critical dimension. dash line indicates the wavelength $\lambda$ scale of feature size.

## 1.3 Outline of thesis

The upcoming Chapter 2 reviews relevant theories and methods of diffraction models and inverse design. The focus in that chapter is on identifying the scalar diffraction theory, i.e., TEA and rigorous electromagnetic theory such as RCWA and introduce gradient-based optimization.

Chapter 3 proposes an optimization based on perturbation approach to overcome the limit of scalar diffraction theory. This framework is formulated through a mathematical foundation of Fourier coefficient with local perturbation caused by sharp step transitions in structures. An important feature of this methodology is to calculate the gradient of diffraction efficiency with respect to transition points analytically. Also, the simulated and experimental results of 1D diffractive beam splitters optimized by this approach are presented.

Chapter 4 builds inverse design with adjoint method. The procedure to obtain the gradient of objective function with respect to design parameter using adjoint method with RCWA are introduced. The inverse design tool incorporates solutions for wide diffraction angle DOEs

and efficient gradient calculation into a method that allows to optimize 1D and 2D fan-out gratings creating wide diffraction angle arrays.

The findings of inverse design methods and evaluations are then summarized in Chapter 5. The inverse design framework presented in this work may be applied to a wide variety of applications, potentially figuring out new structures and functionalities. Whereas the current lead of electromagnetic computation is the quick solution of the response to a given structure, the inverse problem of computing the structure for a given response may prove much more powerful in the future.

# 2 Background

In this chapter, we introduce methods and theories of diffraction models and inverse design that are required to understand the following chapters. The validity regions and computational constraints will be analyzed in detail to identify the practical limits of different diffraction models.

## 2.1 Electromagnetic theory of light

All phenomena of light and its propagation in free space and interactions with structured matter can be explained by Maxwell's equations (excluding quantum level interactions), partial differential equations describing the behavior of electromagnetic field vectors. Considering monochromatic stationary time harmonic fields which is usually used in ideal cases, we have functions of the form

$$\boldsymbol{A}(\boldsymbol{r},t) = \mathrm{Re}\left\{\boldsymbol{A}(\boldsymbol{r})\exp(-i\omega t)\right\} \tag{2.1}$$

where $\boldsymbol{A}(\boldsymbol{r})$ is the complex amplitude of the real part $\boldsymbol{A}(\boldsymbol{r},t)$ and can be replaced with $\boldsymbol{E}(\boldsymbol{r})$, $\boldsymbol{H}(\boldsymbol{r})$, $\boldsymbol{D}(\boldsymbol{r})$, $\boldsymbol{B}(\boldsymbol{r})$, or $\boldsymbol{J}(\boldsymbol{r})$ which are the electric field, magnetic field, electric displacement, magnetic induction and electric current density, respectively. The $\boldsymbol{r}$ represents position vector, $t$ is time, and $\omega$ is angular frequency.

We thus express the differential form of Maxwell's equation [23] in the frequency domain using Eq. (2.1) as,

$$\boldsymbol{\nabla}\cdot\boldsymbol{D}(\boldsymbol{r}) = \rho(\boldsymbol{r}) \tag{2.2a}$$

$$\boldsymbol{\nabla}\cdot\boldsymbol{B}(\boldsymbol{r}) = 0 \tag{2.2b}$$

$$\boldsymbol{\nabla}\times\boldsymbol{E}(\boldsymbol{r}) = i\omega\boldsymbol{B}(\boldsymbol{r}) \tag{2.2c}$$

$$\boldsymbol{\nabla}\times\boldsymbol{H}(\boldsymbol{r}) = \boldsymbol{J}(\boldsymbol{r}) - i\omega\boldsymbol{D}(\boldsymbol{r}), \tag{2.2d}$$

where $\rho$ is the electric charge density. This time-harmonic Maxwell's equations are valid in

vacuum and in any continuous medium, especially, in linear, isotropic, and nondispersive media, we have the constitutive relation

$$\boldsymbol{D}(\boldsymbol{r}) = \epsilon(\boldsymbol{r})\boldsymbol{E}(\boldsymbol{r}) \tag{2.3a}$$

$$\boldsymbol{B}(\boldsymbol{r}) = \mu(\boldsymbol{r})\boldsymbol{H}(\boldsymbol{r}) \tag{2.3b}$$

$$\boldsymbol{J}(\boldsymbol{r}) = \sigma(\boldsymbol{r})\boldsymbol{E}(\boldsymbol{r}), \tag{2.3c}$$

where $\epsilon(\boldsymbol{r}) = \epsilon_0\epsilon_r(\boldsymbol{r})$, $\mu(\boldsymbol{r}) = \mu_0\mu_r(\boldsymbol{r})$, and $\sigma(\boldsymbol{r})$, which are in respective order the permittivity, magnetic permeability, and conductivity. The parameters $\epsilon_0$ and $\epsilon_r(\boldsymbol{r})$ denote the permittivity of vacuum and the relative permittivity. In this work, non-conductive (i.e., dielectric), non-magnetic , and homogeneous media are considered, in which case $\rho(\boldsymbol{r})$, $\sigma(\boldsymbol{r})$, $\boldsymbol{J}(\boldsymbol{r})$ is vanished, $\mu_r(\boldsymbol{r}) = 1$,and $\mu$ and $\epsilon$ do not vary with position in the material. In this case, we define the refractive index as $n = \sqrt{\epsilon_r}$. Additionally, we define the complex relative permittivity as $\epsilon_r^* = n^2 = \epsilon_r + i\frac{\sigma}{\omega\epsilon_0}$ where $n$ is assumed a complex value.

Maxwell's equations Eq. (2.2) are valid only in continuous matter, but diffractive elements are practically always interfaces between two media. Therefore we need boundary conditions relating the field components across the discontinuity. Denoting the unit normal vector of the boundary between media 1 and 2 by $\vec{u}_{12}$, we can describe the electromagnetic boundary conditions in the form

$$\vec{u}_{12} \cdot (\boldsymbol{D}_2 - \boldsymbol{D}_1) = \sigma_s = 0 \tag{2.4a}$$

$$\vec{u}_{12} \cdot (\boldsymbol{B}_2 - \boldsymbol{B}_1) = 0 \tag{2.4b}$$

$$\vec{u}_{12} \times (\boldsymbol{E}_2 - \boldsymbol{E}_1) = \boldsymbol{0} \tag{2.4c}$$

$$\vec{u}_{12} \times (\boldsymbol{H}_2 - \boldsymbol{H}_1) = \boldsymbol{J_s} = \boldsymbol{0}, \tag{2.4d}$$

where $\sigma_s$ is surface charge density between media and $\boldsymbol{J_s}$ is surface current density. In both media 1 and 2 are dielectrics, there are no charges nor surface currents at the interface so that the tangential component of electric field and all the component of he magnetic field should be continuous across the boundary.

In optics, it is not practical to measure the exact magnitudes of the electromagnetic field due to its high frequency. As a measure of the direction of energy flow, we have the Poynting vector $\boldsymbol{S} = \boldsymbol{E} \times \boldsymbol{H}$, and the intensity of the field is obtained from the time average Poynting vector

$$\langle \boldsymbol{S}(\boldsymbol{r}, t) \rangle = \frac{1}{2} \operatorname{Re}\left\{ \boldsymbol{E}(\boldsymbol{r}) \times \boldsymbol{H}^*(\boldsymbol{r}) \right\}, \tag{2.5}$$

which is often considered as a measured of intensity and the direction of the electromagnetic field flow.

## 2.2 Wave propagation

By substituting the constitutive relations and taking the curl of both side of Eq. (2.2)(c) one obtains, after using Eq. (2.2)(d), the following equation for the electric field in a homogenous medium

$$\nabla^2 \boldsymbol{E}(\boldsymbol{r}) + k^2 \boldsymbol{E}(\boldsymbol{r}) = 0, \tag{2.6}$$

where the wave number $k$ is absolute value of wave vector $\boldsymbol{k}$,which is defined by $k = (\omega/c)n = 2\pi n/\lambda$. Here, $\lambda$ and $c$ are the vacuum wavelength of the field and the speed of light in vacuum and $n$ is refractive index of medium. This is referred to as Helmholtz equation, and can also be applied for magnetic field $\boldsymbol{H}(\boldsymbol{r})$. The simplest solution to this is the harmonic plane wave

$$\boldsymbol{E}(\boldsymbol{r}) = \boldsymbol{E_0} \exp(i\boldsymbol{k}\cdot\boldsymbol{r}). \tag{2.7}$$

Since the Helmholtz equation is linear, any superposition of plane waves is also a solution, and obviously the equation is valid for all the cartesian components(i.e., $x$, $y$, $z$-axis components) of the electric and magnetic field separately.

### 2.2.1 Angular spectrum representation

The angular spectrum representation is a mathematical technique to describe optical fields in homogeneous media. Optical fields are described as a superposition of plane waves and evanescent waves which are physically intuitive solutions of Maxwell's equations.

Assuming the electric field $\boldsymbol{E}(\boldsymbol{r})$ at any point $\boldsymbol{r} = (x, y, z)$ in space, we chose an arbitrary axis $z$ and consider the field $\boldsymbol{E}$ in a plane $z = z$ transverse to the chosen axis. In this plane we can evaluate the two-dimensional Fourier transform of the complex field $\boldsymbol{E}(\boldsymbol{r}) = \boldsymbol{E}(x, y; z)$ as

$$\hat{\boldsymbol{E}}(k_x, k_y; z) = \frac{1}{4\pi^2} \iint_{-\infty}^{+\infty} \boldsymbol{E}(x, y; z) \exp\left\{-i(k_x x + k_y y)\right\} \mathrm{d}x\, \mathrm{d}y\,, \tag{2.8}$$

where $x$ , $y$ are the Cartesian transverse coordinates and $k_x$, $k_y$ is the corresponding spatial frequencies. Similarly, the inverse Fourier transform is expressed as

$$\boldsymbol{E}(x, y; z) = \frac{1}{4\pi^2} \iint_{-\infty}^{+\infty} \hat{\boldsymbol{E}}(k_x, k_y; z) \exp\left\{i(k_x x + k_y y)\right\} \mathrm{d}k_x\, \mathrm{d}k_y\,. \tag{2.9}$$

In notation of Eqs. (2.8) and (2.9), the field $\boldsymbol{E} = (E_x, E_y, E_z)$ and its Fourier transform $\hat{\boldsymbol{E}} = (\hat{E}_x, \hat{E}_y, \hat{E}_z)$ represent vectors. The Fourier integrals thus hold separately for each vector component. If the medium is homogeneous, isotropic, linear and source-free in the transverse plane, the optical field with angular frequency $\omega$ has to satisfy the field $\boldsymbol{E}$ in Eq. (2.7). Inserting the Fourier representation of $\boldsymbol{E}(x, y; z)$ in Eq. (2.8) into the in the Helmholtz equation Eq. (2.6),

we obtain that the Fourier spectrum $\hat{\boldsymbol{E}}$ propagates along the $z$-axis as

$$\hat{\boldsymbol{E}}(k_x, k_y;\, z) = \hat{\boldsymbol{E}}\big(k_x, k_y;\, 0\big) \exp(\pm i k_z z) \tag{2.10}$$

where $k_z \equiv \sqrt{k^2 - (k_x^2 + k_y^2)}$. It shows that the Fourier spectrum of $E$ in an arbitrary image plane located at $z = z$ can be calculated by multiplying the spectrum in the object plane at $z = 0$ by the transfer function $\exp(\pm i k_z z)$. The $\pm$ sign specifies that we have two solutions that need to be superimposed: the + sign refers to a wave propagating into the half-space $z > 0$ whereas the − sign denotes a wave propagating into $z < 0$. Finally, we find for arbitrary $z$ substituting the result of Eq. (2.10) into Eq. (2.9)

$$\boldsymbol{E}(x, y;\, z) = \frac{1}{4\pi^2} \iint_{-\infty}^{+\infty} \hat{\boldsymbol{E}}(k_x, k_y;\, 0) \exp\big\{i(k_x x + k_y y)\big\} \exp(\pm i k_z z)\, \mathrm{d}k_x\, \mathrm{d}k_y\,. \tag{2.11}$$

which is referred to the angular spectrum representation. Similarly, we can also represent the magnetic field $\boldsymbol{H}$ by an angular spectrum. It is general solutions of the wave propagation problem [89].

For the case of a purely dielectric medium with no losses, the refractive index $n$ is a real and positive value. The wavenumber $k_z$ is then either real or imaginary value and turns the factor $\exp(\pm i k_z z)$ into an oscillatory or exponentially decaying function. Then, when $k_x^2 + k_y^2 > k^2$, we have exponentially decaying fields, which are named as evanescent waves, whereas $k_x^2 + k_y^2 \leq k^2$ yields propagating waves.

Let us now determine how the fields themselves are related. We denote the transverse coordinates in the object plane at $z = 0$ as $(x', y')$ and in the image plane at $z = z$ as $(x, y)$. The fields in the image plane can be described by the angular spectrum Eq. (2.11) We just represent the Fourier spectrum $\hat{\boldsymbol{E}}(k_x, k_y;\, 0)$ in term of the field in object plane $z = 0$ using Eq. (2.8) as

$$\hat{\boldsymbol{E}}(k_x, k_y;\, 0) = \frac{1}{4\pi^2} \iint_{-\infty}^{+\infty} \boldsymbol{E}(x', y';\, 0) \exp\big\{-i(k_x x' + k_y y')\big\}\, \mathrm{d}x'\, \mathrm{d}y'\,. \tag{2.12}$$

We obtain the following expression for the field $\boldsymbol{E}$ in the image plane $z = z$, applying Eq. (2.12) into Eq. (2.11),

$$\begin{aligned} \boldsymbol{E}(x, y;\, z) &= \frac{1}{4\pi^2} \iint_{-\infty}^{+\infty} \boldsymbol{E}(x', y';\, 0) \iint_{-\infty}^{+\infty} \exp\big\{i\big[k_x(x - x') + k_y(y - y') \pm k_z z\big]\big\}\, \mathrm{d}x'\, \mathrm{d}y'\, \mathrm{d}k_x\, \mathrm{d}k_y \\ &= \boldsymbol{E}(x, y;\, 0) \otimes h(x, y;\, z). \end{aligned} \tag{2.13}$$

This equation describes an invariant filter with the impulse response

$$h(x,y;z) = \iint_{-\infty}^{+\infty} \exp\{i(k_x x + k_y y)\} \exp(\pm i k_z z)\, \mathrm{d}k_x\, \mathrm{d}k_y\,, \tag{2.14}$$

where $h$ is the inverse Fourier transform of the transfer function in spatial frequency domain $\hat{h}(k_x, k_y;\ z)$, i.e., $\exp(\pm i k_z z)$) in Eq. (2.10). Thus, the field at $z = z$ is calculated by the convolution of the impulse response $h$ with the field at $z = 0$.

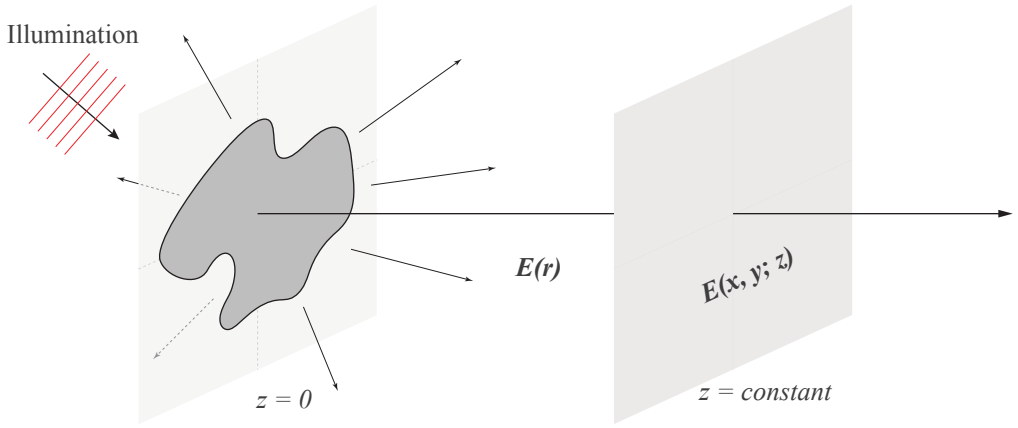


Figure 2.1 – Propagation of the angular spectrum. The fields are evaluated in planes ($z = z$) perpendicular to an arbitrarily chosen $z$-axis.

### 2.2.2 Rayleigh-Sommerfeld representation

The angular spectrum representation which is a solution of the Helmholtz equation, but the Rayleigh-Sommerfeld representation is a mathematical model of the Huygens principle. The observed field $\boldsymbol{E}(x,y,z)$ is considered as a superposition of diverging spherical waves originating from every secondary point source within the aperture plane $\boldsymbol{E}(x',y',0)$. Figure 2.2 illustrate the situation geometrically. $r$ is the distance between source point $(x',y',0)$ and the observation point $(x,y,z)$

$$r^2 = (x-x')^2 + (y-y')^2 + z^2 \tag{2.15}$$

The Rayleigh-Sommerfeld diffraction formula is given in as:

$$E(x,y;z) = -\frac{1}{2\pi} \iint_{-\infty}^{+\infty} E(x',y';0) \frac{\exp(-ikr)}{r} \frac{z}{r} \left(ik + \frac{1}{r}\right) \mathrm{d}x'\, \mathrm{d}y'\,, \tag{2.16}$$

Despite the apparent differences of their approaches, the angular spectrum representation and the Rayleigh-Sommerfeld solution yield identical descriptions of diffracted fields [87]. Equation (2.16) can be seen as a convolution of the source-plane field $\boldsymbol{E}(x',y';0)$ with an

impulse response $h$,

$$h(x,y,z) = \frac{1}{2\pi}\left(ik - \frac{1}{r}\right)\frac{z}{r}\frac{\exp(ikr)}{r}. \tag{2.17}$$

If the distance from the aperture plane to the observation plane is large compared with the wavelength,i.e., $r \gg \lambda$, the Rayleigh-Sommerfeld representation can be rewritten,

$$E(x,y;z) = \frac{1}{i\lambda}\iint_{-\infty}^{+\infty} E(x',y';0)\frac{\exp(ikr)}{r}\frac{z}{r}\,\mathrm{d}x'\,\mathrm{d}y'. \tag{2.18}$$

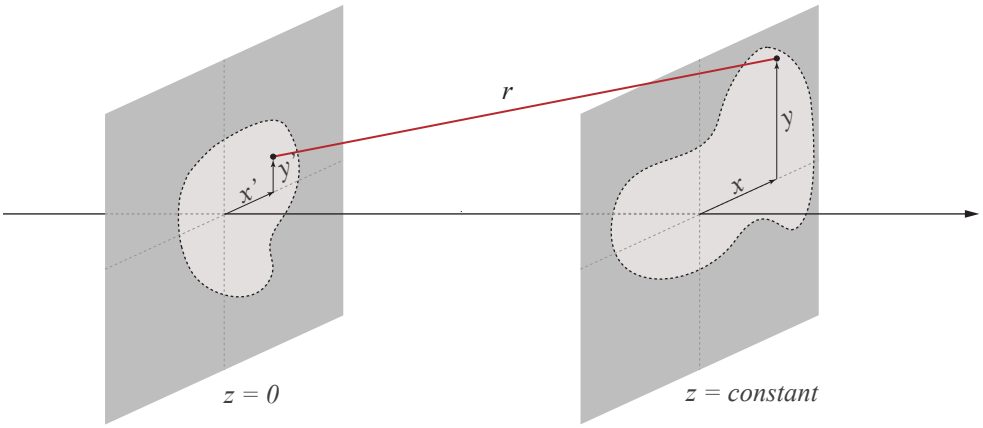


Figure 2.2 – Coordinates used in of Rayleigh-Sommerfeld representation and the geometry of the model

### 2.2.3 Paraxial approximation

In many optical problems, the light field propagates along a certain direction, e.g., $z$-axis but spread out slowly in a transverse direction, i.e., $x$ and $y$-axis, for instance, laser beam propagation. In this case, the wave vector in the angular spectrum is almost parallel to the $z$-axis, and transverse wave numbers $(k_x, k_y)$ are significantly small compared to $k$. Then we may employ the following approximation,

$$k_z = k\sqrt{1 - \frac{(k_x^2 + k_y^2)}{k^2}} \approx k - \frac{k_x^2 + k_y^2}{2k}. \tag{2.19}$$

This is referred to as the paraxial approximation and it considerably simplifies the analytical integration of the Fourier integrals.

### 2.2.4 Fresnel representation

Applying the paraxial approximation in the situation illustrated in Fig. 2.2. The $R$ is the observation distance defined as the distance from the origin in the source plane (e.g., center of an aperture) to the observation point. On the other hand, $r$ is the true distance between source point $(x', y', 0)$ and the observation point $(x, y, z)$. The $r$ is represented as

$$\begin{aligned} r &= \sqrt{(x-x')^2 + (y-y')^2 + z^2} = z\sqrt{1 + \frac{(x-x')^2}{z^2} + \frac{(y-y')^2}{z^2}} \\ &\approx z\left[1 + \frac{(x-x')^2}{2z^2} + \frac{(y-y')^2}{2z^2}\right] \end{aligned} \tag{2.20}$$

Inserting Eq. (2.20) into Eq. (2.18), we can obtain the following equation,

$$E(x, y; z) = \frac{\exp(ikz)}{i\lambda z} \iint_{-\infty}^{+\infty} E(x', y'; 0) \exp\left\{\frac{ik}{2z}\left[(x-x')^2 + (y-y')^2\right]\right\} \mathrm{d}x'\,\mathrm{d}y'. \tag{2.21}$$

which is a convolution of the field in aperture plane $E(x', y', 0)$ with an impulse response $h(x, y; z) = \exp\left[\frac{ik}{2z}(x^2 + y^2)\right]$. Extracting the constant phase term out of the integrals, we obtain the formula:

$$\begin{aligned} E(x, y; z) = &\frac{\exp\left[ikz + \frac{ik}{2z}(x^2 + y^2)\right]}{i\lambda z} \\ &\iint_{-\infty}^{+\infty} E(x', y'; 0) \exp\left[\frac{ik}{2z}(x'^2 + y'^2)\right] \exp\left[-i2\pi(k_x x' + k_y y')\right] \mathrm{d}x'\,\mathrm{d}y'. \end{aligned} \tag{2.22}$$

where $k_x = \frac{x}{\lambda z}$ and $k_y = \frac{y}{\lambda z}$. Fresnel approximation can be written as a Fourier transform:

$$E(x, y; z) = \frac{1}{i\lambda z} \exp\left[ikz + \frac{ik}{2z}(x^2 + y^2)\right] \mathrm{FT}\left\{E(x', y'; 0) \exp\left[\frac{ik}{2z}(x'^2 + y'^2)\right]\right\}. \tag{2.23}$$

The Fresnel representation covers the common situation in which the observation plane is at a finite distance behind the object. This is the Fresnel representation often used in derivations since it gives many analytical results [90].

### 2.2.5 Fraunhofer representation

The Fraunhofer diffraction is a special case and analytically a simplification of the Fresnel diffraction, which is valid for large distances. Equation (2.22) for large values of $z$ reduces to just a Fourier transform operation

$$E(x, y; z) = \frac{\exp(ikz)}{i\lambda z} \mathrm{FT}\left\{E(x', y'; 0)\right\}, \tag{2.24}$$

which is valid only for very large distances given by $z \gg \frac{k(x^2+y^2)}{2}$.

## 2.3 Thin element approximation

The easiest method available for determining the response of diffractive structures is the thin element. This approximation is very useful provided that not only minimum features of the structure are at least $10\lambda$ but also the thickness of the element is of the order of the wavelength. Then, the optical path calculation yields sufficient accuracy for the field distribution after the element.

Let us consider the plane wave through the structure consist of the material with different refractive index from air. The scheme of this situation as shown in the Fig. 2.3. Assuming a scalar incident field $U_0(x, y, 0)$ arriving at the structure, which has a complex refractive index $n(x, y, z)$ and depth $d$, we can propagate the field through the diffractive structure by using the complex amplitude transmittance approach. The transmitted field

$$U_T(x, y; d) = t(x, y) \cdot U_0(x, y; 0) \tag{2.25}$$

where the complex amplitude transmittance function $t(x, y)$ is given by

$$t(x, y) = \exp\left[ik \int_0^d n^*(x, y, z)\,\mathrm{d}z\right] \tag{2.26}$$

where $n^*$ is the complex refractive index of the element. The complex refractive index is consist of

$$n^* = n + i\kappa \tag{2.27}$$

where $n$ is the real refractive index and $\kappa$ is the absorption coefficient. If the material is non-conductive, i.e., $\kappa = 0$, the element only affects the phase of the incident field.

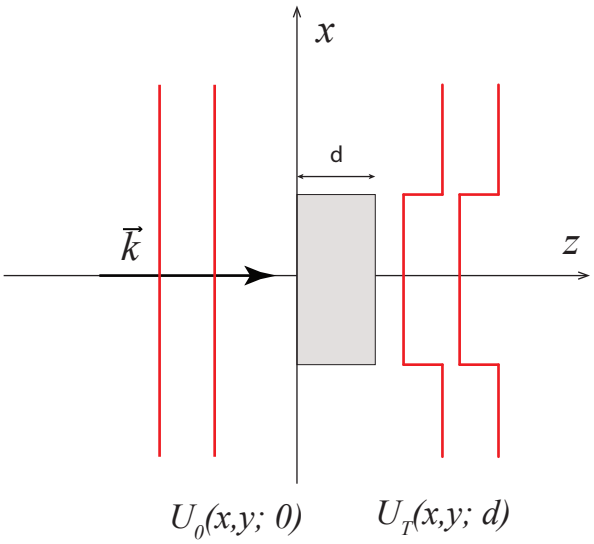


Figure 2.3 – Scheme of the propagation through the element using complex amplitude transmittance

### 2.3.1 Diffraction at binary gratings

If the structure is periodic,e.g., gratings, its spatial frequency spectrum is consists of discrete frequencies. We assume a unit-amplitude plane wave illumination from the substrate of grating. Thus, the gratings show a discrete far-field diffraction pattern, in contrast to the spatially continuous diffraction patterns of spatially aperiodic objects. The field through the structure $U_T$ can be expanded in a Fourier series,

$$U_T(x,y,d) = \sum_{m,n} T_{mn} \exp\left[i2\pi\left(\frac{mx}{\Lambda_x} + \frac{nx}{\Lambda_y}\right)\right] \tag{2.28}$$

where the Fourier coefficients $T_{mn}$ are obtained from

$$T_{mn} = \frac{1}{\Lambda_x \Lambda_y} \int_0^{\Lambda_x} \int_0^{\Lambda_y} U_T(x,y;d) \exp\left[-i2\pi\left(\frac{mx}{\Lambda_x} + \frac{ny}{\Lambda_y}\right)\right] \mathrm{d}x\,\mathrm{d}y \tag{2.29a}$$

$$= \frac{T_{in}}{\Lambda_x \Lambda_y} \int_0^{\Lambda_x} \int_0^{\Lambda_y} t(x,y) \exp\left[-i2\pi\left(\frac{mx}{\Lambda_x} + \frac{ny}{\Lambda_y}\right)\right] \mathrm{d}x\,\mathrm{d}y \tag{2.29b}$$

and the periods along the $x$ and $y$-axis are denoted by $\Lambda_x$ and $\Lambda_y$. The Fourier coefficients $T_{mn}$ means the complex-valued amplitudes of the diffracted waves in the far-field. $T_{in}$ means the complex amplitude of incident wave and it become 1 when we set the unit-amplitude plane wave illumination.

Let us consider the Fourier coefficient in one-dimensional binary grating in Fig. 2.4. The phase profile of a binary grating period consists of $K$ grooves of equal depth but different width. The coordinates $x_1, \cdots, x_{2K}$ of the grooves represent phase transitions positions. Then we

represent the transmittance function as

$$t(x) = \begin{cases} \exp(i\Phi_1) = \exp(ikn_1 d), & \text{for } x_k = x_1, x_3, \cdots, x_{2K-1} \\ \exp(i\Phi_2) = \exp(ikn_2 d), & \text{for } x_k = x_2, x_4, \cdots, x_{2K} \end{cases} \tag{2.30}$$

where $\Phi_1$ and $\Phi_2$ is the phase shift by optical path of depth $d$ with refractive of $n_1$ and $n_2$. Then, we express the Fourier coefficient as

$$T_m = \frac{\sin(\Delta\Phi/2)}{m\pi d} \sum_{k=1}^{2K} (-1)^k \exp(-i2\pi m x_k/d), \qquad \text{for} \quad m \neq 0 \tag{2.31a}$$

$$T_0 = \exp(i\Phi_1) - \frac{2\sin(\Delta\Phi/2)}{d} \left[ i \exp\left( i \frac{\Phi_1 + \Phi_2}{2} \right) \right] \sum_{k=1}^{2K} (-1)^k \cdot x_k \tag{2.31b}$$

where $\Delta\Phi$ is the difference of $\Phi_1$ and $\Phi_2$. Using the diffraction efficiency $\eta_m$ is $|T_m|^2$, we can find the analytical form as following

$$\eta_m = \frac{\sin^2(\Delta\Phi/2)}{(m\pi)^2} (C_k^2 + S_k^2) \tag{2.32a}$$

$$\eta_0 = 1 - 4Q(1-Q)\sin^2(\Delta\Phi/2) \tag{2.32b}$$

where

$$C_k = \sum_{k=1}^{2K} (-1)^k \cos(2\pi m x_k) \tag{2.33a}$$

$$S_k = \sum_{k=1}^{2K} (-1)^k \sin(2\pi m x_k) \tag{2.33b}$$

$$Q = \sum_{k=1}^{2K} (-1)^k x_k \tag{2.33c}$$

We observe the fact $\eta_m = \eta_{-m}$ from the Eqs. (2.32) and (2.33). Hence, the diffraction patterns of binary gratings have always symmetry by simulation of TEA.

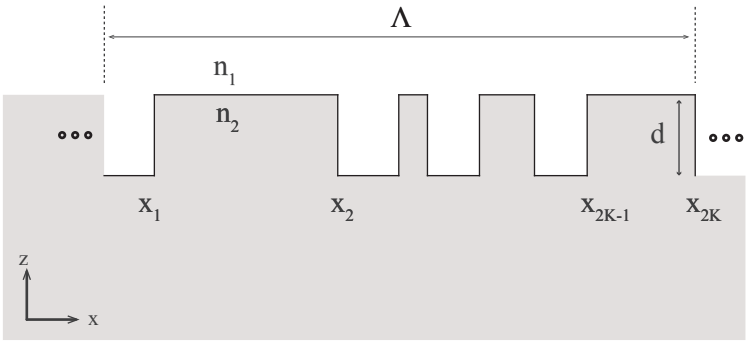


Figure 2.4 – Surface profile of the one-dimensional binary grating

### 2.3.2 Limit of the TEA

One of the most discernible examples of the limits of the TEA is the prediction in the direction of the diffracted field after the structure. To observe this limitation, let us consider simple one dimensional (1D) binary grating consist of one ridge, which is illuminated by a linear transverse electric (TE)-polarized plane wave,i.e., the illumination wave consists of two components: $E_y$and $H_x$. If we apply the TEA to this grating to calculate its transmitted fields, the fields through the structure will consist of only the two components $E_y$ and $H_x$, with a phase shift $\Delta\Phi$ due to the optical path length difference $E_y \exp(i\Delta\Phi)$ and $H_x \exp(i\Delta\Phi)$. However, This is not true according to Maxwell's equation. Eq. (2.2)

If we compute the fields in the same grating using rigorous electromagnetic solver such as RCWA, there are three components $E_y$, $H_x$, and $H_z$ as shown in Fig. 2.5. In the simulation, we use the parameters which are $\lambda = 633\,\text{nm}$ of wavelength, $\Lambda = 8\,\mu\text{m}$ of grating period, $4\,\mu\text{m}$ width of one ridge. The depth is corresponding to $\pi$ phase shift so that the depth is $d = 693\,\text{nm}$, where the refractive index of dielectric material is $n = 1.46$. In Fig. 2.5, we can observe the boundary of the grating structure indicated by the black and white lines. The plane wave illuminates from the bottom to the top. The RCWA simulation is run with a sufficiently large number of Fourier modes. Its details will be discussed in the next section.

This result in Fig. 2.5(e) and (f) show that there are generation of $H_z$ component during the propagation according to Eq. (2.2),i.e., $H_x \propto \frac{\partial E_y}{\partial x}$, $H_z \propto \frac{\partial E_y}{\partial z}$, which is rigorous in the vectorial domain. This can be explained due to the oscillation of $E_y$ in Fig. 2.5(a) and (b) in the direction perpendicular to the ridge, leading to the diffraction of the magnetic field into the $z$-direction at the interface between different media. However, the TEA fails to predict the diffraction of the electromagnetic component perpendicular to the direction, i.e., the generation of the $H_z$ component after the structure. The phenomenon is similar for the case of linear transverse magnetic (TM)-polarized plane waves, where the illumination has only two components $H_y$, $E_x$ but the transmitted field contains three components $H_y$, $E_x$, $E_z$.

To assess the error of the TEA, we compare the amplitude and phase distribution of the fields on the plane after the grating, which is simulated by RCWA and TEA as represented in Fig. 2.6. In Fig. 2.6(a) and (b), the field $E_y$ from TE-polarized illumination and in (c) and (d) the field $H_y$ from the case of TM-polarized illumination is presented. The amplitude and phase of the field in a ridged surface profile determined by TEA indicated by the blue dash line in Fig. 2.6. The field obtained by the RCWA simulation is complex comparing to a result as predicted by the TEA. In sharp transition points, the perturbations are observed by RCWA, even though TEA yields the constant amplitude and phase and no difference between TE- and TM-polarized illumination. This omission of perturbation in TEA makes computing inaccurate within wavelength-scale structures, so call non-paraxial domain or resonance domain.

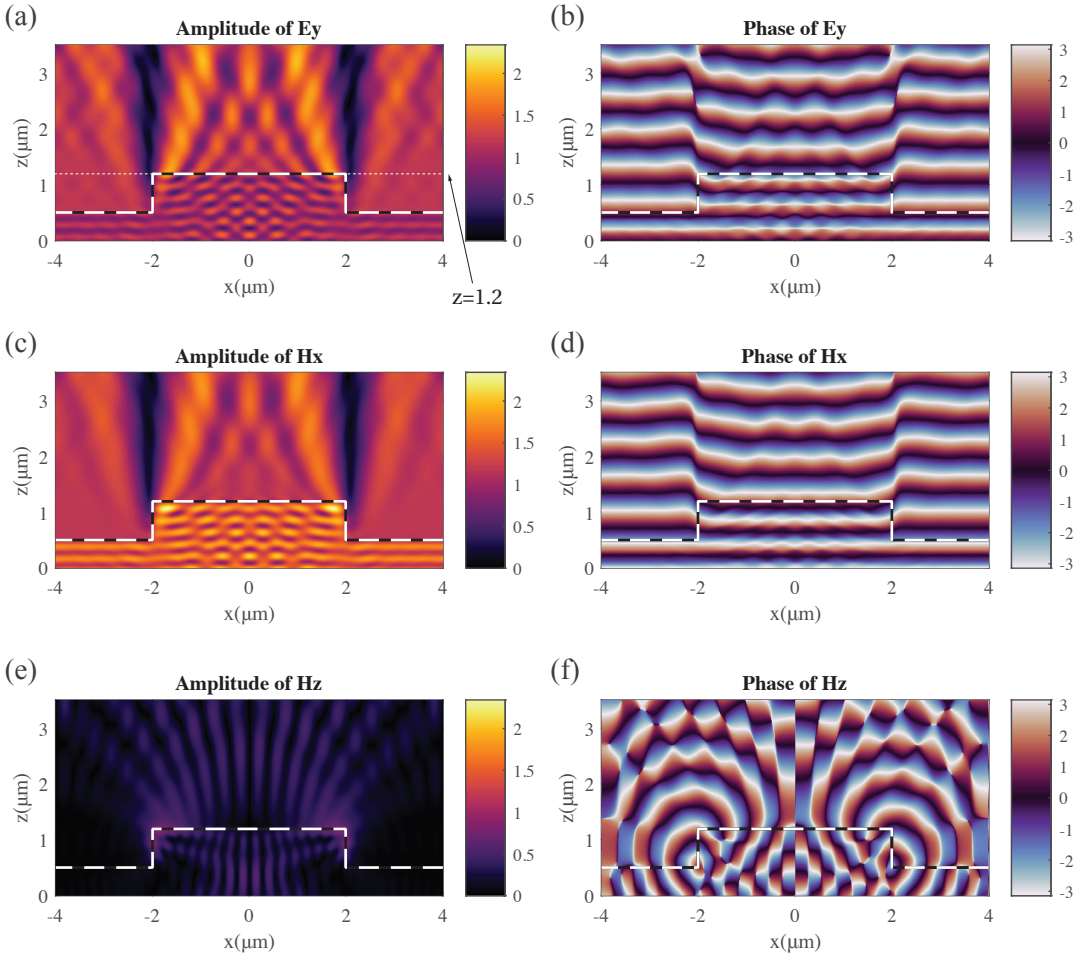


Figure 2.5 – Electromagnetic fields in periodic 1D binary grating illuminated by a TE-polarized plane wave simulated by rigorous coupled-wave analysis (RCWA). (a) The amplitude and (b) phase of $E_y$ component in the structure. (c) The amplitude and (d) phase of $H_x$ component and (e) the amplitude and (f) phase of $H_z$ component. The illumination propagates from the plane $z = 0$ to the top. The boundary of the grating is indicated by the black and white lines. The field distribution in the plane $z = 1.2$ is given by Fig. 2.6

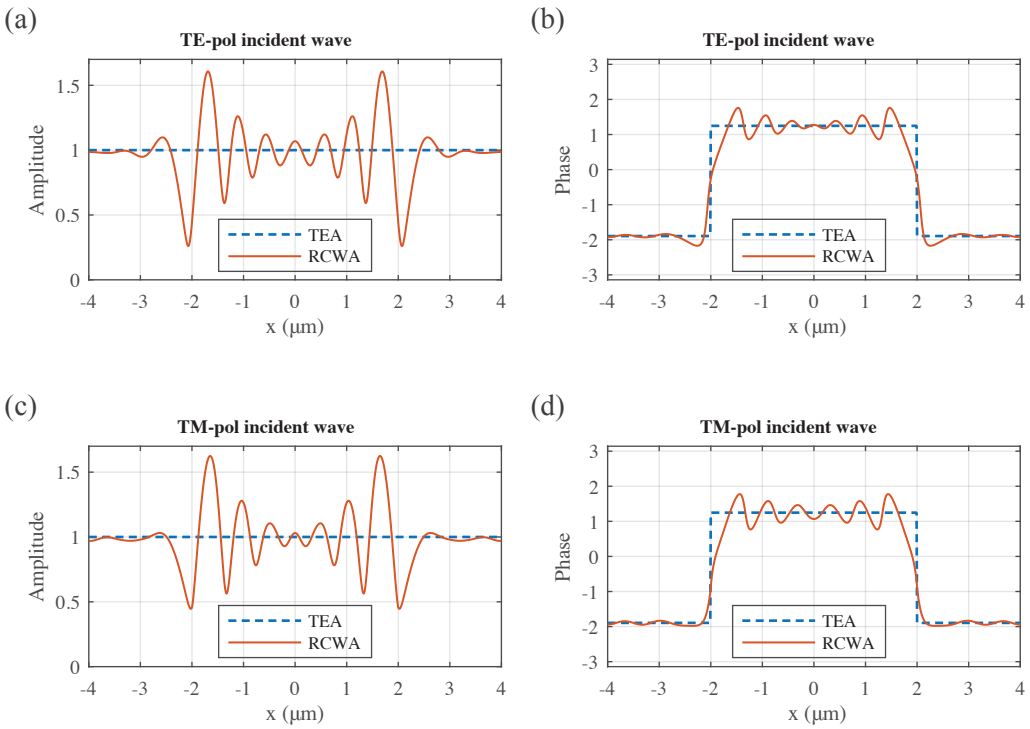


Figure 2.6 – The field distribution in the plane after the grating, i.e., the plane $z = 1.2$ in Fig. 2.5. (a) Amplitude and (b) phase of the electric field $E_y$ in TE-polarized illumination and (c) the amplitude and (d) phase of the magnetic field $H_y$ in TM-polarized illumination. The fields are calculated by RCWA (red line) and TEA ( blue dashed line)

## 2.4 Rigorous coupled-wave analysis

Scalar diffraction theories such as thin element approximation are well established in the paraxial domain, in which the electromagnetic nature of light may often be neglected. However, in the non-paraxial domain, multiple scattering and the effects of polarization appear. As a result, the scalar theory fails and it becomes necessary to apply rigorous electromagnetic theory to simulate correctly the behavior of light in the structure. Different rigorous methods can be used to simulate wide-angle DOEs. The well-known methods include the Finite-Difference Time-Domain method (FDTD) [91, 92], the Finite Element Method (FEM) [93–95], the Finite-Difference Frequency-Domain method (FDFD) [96], Method of Moments [97], and the Rigorous Coupled Wave Analysis (RCWA) [63, 70, 98–104] also known as the Fourier Modal Method (FMM).

### 2.4.1 Historical overview

One of the first numerical methods for gratings has been the differential method [105, 106]. The method is mainly applied to describe the interaction of light with gratings. The grating system can be divided into three regions: the homogeneous substrate region, the structured grating region, and the homogeneous layer above the grating as shown in Fig. 2.7(a). Due to the periodicity of the grating, the description of fields in the homogeneous layer upward and downward grating are given by the Rayleigh expansion [107]. The fields in the grating region can be expanded in Fourier series along with the periodic directions according to the Floque-Bloch theorem. By inserting the expansion for the grating region in Maxwell's equations, we obtain a set of differential equations for the coefficients which determine the propagation of the light perpendicular to the grating plane. Together with the Rayleigh expansions in the outside of the grating region, the differential equations build a boundary value problem. Then it can be solved via the so-called shooting method which is a method for solving initial and boundary value problems in the classical differential method. When these problems are solved with computers, the infinite series of the expansions have to be truncated. This can cause convergence problems that already arise for purely two-dimensional metallic gratings in TM-polarization. Additionally, the method becomes unstable for deep gratings [106]. As an alternative, new methods such as the Rigorous coupled-wave analysis[59, 60], have been proposed. In RCWA, the grating profile is approximated by a stack of lamellar gratings as illustrated in Fig. 2.7(b) and each lamellar layer can be solved independently by an eigenvalue technique. Besides, there are many efforts for stable and reliable results by introducing the scattering matrix algorithm [108, 109], improving the convergence in metallic gratings[62, 110]. It was explained by the convergence behavior of the truncated Fourier series for continuous and discontinuous functions and it is named correct Fourier factorization [111, 112]. Using this technique a new formulation of the RCWA for crossed gratings is called the Fourier modal method [63]. In the following, we briefly present the Fourier Modal Method as developed with the correct Fourier factorization.

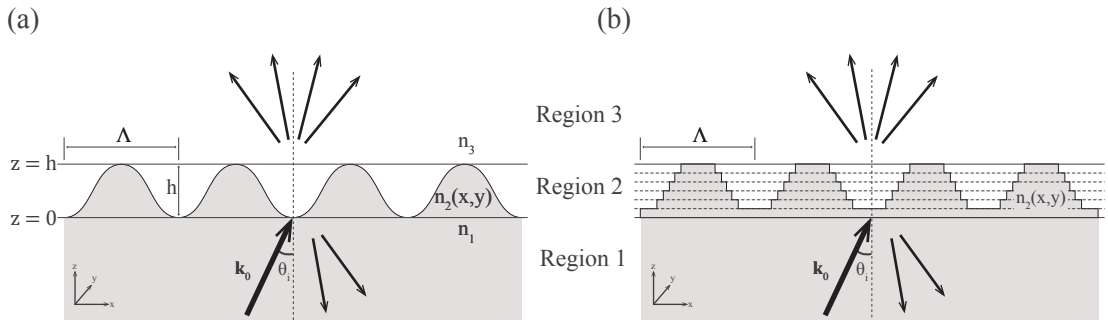


Figure 2.7 – (a) Grating with homogeneous upward region, structured grating region, and the homogeneous substrate. (b) Approximation of the structure of (a) into a stacked lamellar structures that can be simulated using the Fourier modal method.

### 2.4.2 Incident plane wave

There are two homogeneous regions denoted by region 1 and region 3 with refractive index $n_1$ and $n_3$ in the above Fig. 2.7(b). In the middle, stacked layers in region 2 located between $0 \le z \le h$. A periodic modulation of region 2, which is divided into $z$-invariant layers, for example $0 \le h_1 \le h_2 \le \cdots \le h$, and $n_j(x,y)$ is the distribution of the refractive index between the boundaries $h_j$ and $h_{j+1}$. The unit-amplitude plane wave illuminated from the negative direction of $z$-axis. The wave vector $\boldsymbol{k}_0$ of incident wave have an angle $\theta$ with respect to the $z$-axis the azimuthal angel is denoted by $\phi$. The parameter $\psi$ defined the angle between the incident plane and the polarization vector $\boldsymbol{u}$.

Thus we can represent the incident field as

$$\boldsymbol{E}_0(x,y,z) = \boldsymbol{u}\exp\big[i(k_{x,0}+k_{y,0}+\gamma_{00})\big], \tag{2.34}$$

where $k_{x,0} = kn_1\sin\theta\cos\phi$, $k_{y,0} = kn_1\sin\theta\sin\phi$, and $\gamma_{00} = kn_1\cos\theta$. The values $k_{x,0}$, $k_{y,0}$, and $\gamma_{00}$ form

$$\boldsymbol{k}_0 = k_{x,0}\boldsymbol{x} + k_{y,0}\boldsymbol{y} + \gamma_{00}\boldsymbol{z}, \tag{2.35}$$

which is the wave vector of the incident field. And the polarization vector $\boldsymbol{u}$ is expressed by

$$\begin{aligned}\boldsymbol{u} =& (\cos\psi\cos\theta\cos\phi - \sin\psi\sin\phi)\boldsymbol{x} \\ &+ (\cos\psi\cos\theta\sin\phi + \sin\psi\cos\phi)\boldsymbol{y} \\ &- \cos\psi\sin\theta\boldsymbol{z}.\end{aligned} \tag{2.36}$$

The geometry of incident vector is illustrate in Fig. 2.8(a).

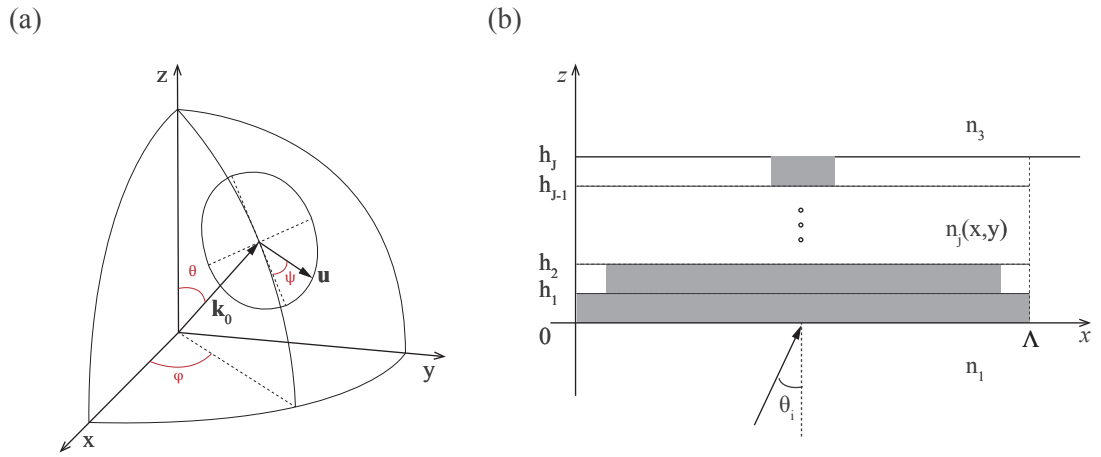


Figure 2.8 – (a) Scheme of geometry of incident vector (b) surface profile of grating with lamellar layers

### 2.4.3 Floque-Bloch wave and Rayleigh expansion

In above Fig. 2.7(b), each lamellar layer in region 2 has a periodic permittivity distribution

$$\epsilon(x,y,z) = \epsilon(x+\Lambda_x, y+\Lambda_y, z), \tag{2.37}$$

where $\Lambda_x$, $\Lambda_y$ is grating period along $x$ and $y$-axis. Considering the plane wave in Eq. (2.34) illuminate the medium of this permittivity distribution with the assumption of lossless medium, we can represent each field component satisfies the Floque-Bloch theorem everywhere in space:

$$U(x+\Lambda_x, y+\Lambda_y, z) = U(x,y,z)\exp\left[i(k_{x,0}\Lambda_x + k_{y,0}\Lambda_y)\right]. \tag{2.38}$$

The field is thus laterally periodic with period $\Lambda_x$ and $\Lambda_y$ apart from a phase factor determined by the constant $k_{x,0}$ and $k_{y,0}$, and is called pseudo-periodic. Substitution of Eq. (2.38) into the angular spectrum representation of Eq. (2.11) leads to the following condition for the lateral propagation coefficient of the pseudo-periodic field

$$k_{x,m} = k_{x,0} + \frac{2\pi m}{\Lambda_x} \tag{2.39a}$$

$$k_{y,n} = k_{y,0} + \frac{2\pi n}{\Lambda_y}, \tag{2.39b}$$

where $m$, $n$ are integers. The pseudo-periodicity of the field discretizes the angular spectrum, i.e., the diffracted plane waves only have a discrete set of allowed propagation directions. Therefore the angular spectrum is reduced to the Rayleigh expansion of the scattered field in homogeneous regions. The reflected and transmitted electric field in region 1 and 3 is given

by

$$\boldsymbol{E}_R(x,y,z) = \sum_{m,n=-\infty}^{\infty} \boldsymbol{R}_{mn} \exp\left[i(k_{x,m}x + k_{y,n}y - i\gamma^R_{mn}z)\right] \qquad \text{if} \quad z \le 0 \tag{2.40a}$$

$$\boldsymbol{E}_T(x,y,z) = \sum_{m,n=-\infty}^{\infty} \boldsymbol{T}_{mn} \exp\left\{i\left[k_{x,m}x + k_{y,n}y + i\gamma^T_{mn}(z-h)\right]\right\} \qquad \text{if} \quad z \ge h \tag{2.40b}$$

where the $\gamma^R_{mn} = \sqrt{(n_1 k)^2 - {k_{x,m}}^2 - {k_{y,n}}^2}$ and $\gamma^T_{mn} = \sqrt{(n_3 k)^2 - {k_{x,m}}^2 - {k_{y,n}}^2}$ and $\boldsymbol{R}_{mn}$ and $\boldsymbol{T}_{mn}$ denote the complex amplitudes vector of the reflected and transmitted fields, respectively. Imaginary values of $\gamma^R_{mn}$ and $\gamma^T_{mn}$ indicate evanescent waves which decays exponentially. Corresponding magnetic fields $\boldsymbol{H}$ in regions 1 and 3 can be solved from the relation in Eq. (2.2)(c) and (d).

Let us consider the propagation directions of the plane waves of Rayleigh expansion. We can obtain the propagation angle of each order by $\theta_m$ using the condition $\gamma^T_{mn} = n_3 k\cos(\theta_{mn})$. The propagation angle $\theta_{mn}$ of the $mn$-th transmitted diffraction order thus can be represent the following equation

$$(n_3 k\sin\theta_{mn})^2 = \left(n_1 k\sin\theta\cos\phi + \frac{2m\pi}{\Lambda_x}\right)^2 + \left(n_1 k\sin\theta\sin\phi + \frac{2n\pi}{\Lambda_y}\right)^2, \tag{2.41}$$

which drives the one-dimensional grating equation if the period $\Lambda_y$ is towards infinity and $\phi = 0$. while for the reflected diffraction angles, one replaces $n_3$ with $n_1$ in Eq. (2.41). It means that the diffraction angle $\theta_{mn}$ in Eq. (2.41) only depend on the grating period $\Lambda_x$ and $\Lambda_y$ and wavelength $\lambda$ of incident light. The structure design in period only controls the distribution of diffraction intensity between the diffraction orders.

### 2.4.4 Fourier factorization

Let us briefly outline the correct Fourier factorization by taking into account the behavior of partial sums at the points of discontinuity [63, 111]. In order to obtain fast convergence, a truncated expansion has to be performed by carefully considering Fourier Factorization rules.

Considering a periodic permittivity distribution that is discontinuous in both $x$ and $y$ directions, $E_s(x,y,z)$ denote an arbitrary scalar component of electric field and $\boldsymbol{E_s}$ denote the vector consisting of its Fourier coefficients. The Fourier vectors are composed of the Fourier coefficients $E_{mn}$ according to the rule in [70]

$$[\boldsymbol{E}_s]_{m'n} = E_{mn}, \tag{2.42}$$

where $m'$ is $m' = m + 2M + 1$ with M is trancated Fourier number $-M : M$. We define $[\![\epsilon]\!]$,

$[\![\epsilon_x(y)]\!]$ $[\![\epsilon_y(x)]\!]$ as Toeplitz matrice builded form the Fourier coefficient

$$\epsilon_{mn} = \frac{1}{\Lambda_x \Lambda_y} \int_0^{\Lambda_x} \int_0^{\Lambda_y} \epsilon(x,y) \exp\left[-i2\pi(mx/\Lambda_x + ny/\Lambda_y)\right] \mathrm{d}x\,\mathrm{d}y \tag{2.43a}$$

$$\epsilon_{x,m}(y) = \frac{1}{\Lambda_x} \int_0^{\Lambda_x} \frac{1}{\epsilon(x,y)} \exp[-i2\pi(mx/\Lambda_x)]\,\mathrm{d}x \tag{2.43b}$$

$$\epsilon_{y,n}(x) = \frac{1}{\Lambda_y} \int_0^{\Lambda_y} \frac{1}{\epsilon(x,y)} \exp\left[-i2\pi(my/\Lambda_y)\right] \mathrm{d}y, \tag{2.43c}$$

and $[\![\epsilon_{xy}]\!]$ and $[\![\epsilon_{yx}]\!]$ composed of the following elements:

$$\epsilon_{xy,mn} = \frac{1}{\Lambda_y} \int_0^{\Lambda_y} [\![\epsilon_x(y)]\!]^{-1} \exp\left[-i2\pi(my/\Lambda_y)\right] \mathrm{d}y \tag{2.44a}$$

$$\epsilon_{yx,mn} = \frac{1}{\Lambda_x} \int_0^{\Lambda_x} [\![\epsilon_y(x)]\!]^{-1} \exp\left[-i2\pi(my/\Lambda_x)\right] \mathrm{d}x. \tag{2.44b}$$

Using the expression in Eq. (2.42), the Fourier coefficient of the product of permittivity and electric field, which is the dielectric displacement $D_p(x,y,z) = \epsilon(x,y)E_s(x,y;z)$ represented by correct factorization rules:

$$\boldsymbol{D}_p = [\![\epsilon]\!]\boldsymbol{E}_s \tag{2.45a}$$

$$\boldsymbol{D}_p = [\![\epsilon_{xy}]\!]\boldsymbol{E}_s \tag{2.45b}$$

$$\boldsymbol{D}_p = [\![\epsilon_{yx}]\!]\boldsymbol{E}_s. \tag{2.45c}$$

where $\boldsymbol{D}_p$ is the vector containing the Fourier coefficients of $D_p(x,y,z)$. If $E_s(x,y,z)$ and $\epsilon(x,y,z)$ have no concurrent discontinuities, the Fourier coefficients of the product $D_p(x,y,z) = \epsilon(x,y)E_s(x,y;z)$ obtained from Laurent's rule in Eq. (2.45)a. If both $E_s(x,y,z)$ and $\epsilon(x,y,z)$ have complementary concurrent discontinuities in $x$-direaction,i.e., $D_p$ is still continuous, applying Eq. (2.45)b in the Fourier factorization. Similarly, wehn the complementary concurrent discontinuities take place in the $y$-direaction, we use Eq. (2.45)c. This is called inverse rule in Eq. (2.45)b, c. Furthermore, if the functions are discontinuous in both directions, we use the inverse matrix of the coefficients $[\![\epsilon]\!]^{-1}$ of the function $1/\epsilon(x,y)$. A detailed description of the problem can be found in these article [63].

### 2.4.5 Computation of Eigenmode

In order to represent in the structured region, we need to consider only four field components and thus we eliminate the $z$-components of the magnetic and electric field. According to the Floque-Bloch theorem, the fields are pseudo-periodic in two dimensions and each field can be expressed as

$$U_s(x,y,z) = \sum_n \sum_m U_{s,mn} \exp\left[i k_{x,m} x + k_{y,n} y + \gamma z\right], \tag{2.46}$$

where $U_s$ become any scalar component of the electric and magnetic field, e.g., $E_x$, $H_x$, $E_y$, $H_y$. Here, we confine our attention only to the electric field. Operating with the divergence operator to Eq. (2.2)(d) and using the relation $\boldsymbol{\nabla}\cdot(\boldsymbol{\nabla}\times\mathbf{A})=0$, we may express

$$\boldsymbol{\nabla}\cdot(\boldsymbol{\nabla}\times\boldsymbol{H}) = -i\omega\boldsymbol{\nabla}\cdot\left[\epsilon(x,y)\boldsymbol{E}\right] = 0. \tag{2.47}$$

Thus, we find

$$\frac{\partial E_z}{\partial z} = -\frac{1}{\epsilon(x,y)}\left\{\frac{\partial}{\partial x}[\epsilon(x,y)E_x] + \frac{\partial}{\partial y}[\epsilon(x,y)E_y]\right\}. \tag{2.48}$$

By applying the curl operation to Eq. (2.2)(c), then we have

$$\boldsymbol{\nabla}\times(\boldsymbol{\nabla}\times\boldsymbol{E}) = i\omega\boldsymbol{\nabla}\times\boldsymbol{H} = k^2\epsilon(x,y)\boldsymbol{E} \tag{2.49}$$

Using $\boldsymbol{\nabla}\times(\boldsymbol{\nabla}\times\mathbf{A}) = \boldsymbol{\nabla}(\boldsymbol{\nabla}\cdot\mathbf{A}) - \boldsymbol{\nabla}^2\mathbf{A}$ we drive the inhomogeneous wave equation

$$\begin{aligned}\left[k^2\epsilon(x,y)+\boldsymbol{\nabla}^2\right]\boldsymbol{E} &= \boldsymbol{\nabla}(\boldsymbol{\nabla}\cdot\boldsymbol{E})\\ &= \boldsymbol{\nabla}\left(\frac{\partial E_x}{\partial x}+\frac{\partial E_y}{\partial y}+\frac{\partial E_z}{\partial z}\right)\end{aligned} \tag{2.50}$$

Inserting the Eq. (2.48) into Eq. (2.50), the relations between the x and y-components of the electric field are represented in the forms

$$-\frac{\partial^2 E_x}{\partial z^2} = \left[k^2\epsilon(x,y)+\frac{\partial^2}{\partial x^2}+\frac{\partial}{\partial x}\frac{1}{\epsilon(x,y)}\frac{\partial}{\partial x}\epsilon(x,y)\right]E_x + \left[\frac{\partial}{\partial x}\frac{1}{\epsilon(x,y)}\frac{\partial}{\partial y}\epsilon(x,y) - \frac{\partial}{\partial x}\frac{\partial}{\partial y}\right]E_y \tag{2.51a}$$

$$-\frac{\partial^2 E_y}{\partial z^2} = \left[\frac{\partial}{\partial y}\frac{1}{\epsilon(x,y)}\frac{\partial}{\partial x}\epsilon(x,y) - \frac{\partial}{\partial y}\frac{\partial}{\partial x}\right]E_x + \left[k^2\epsilon(x,y)+\frac{\partial^2}{\partial x^2}+\frac{\partial}{\partial y}\frac{1}{\epsilon(x,y)}\frac{\partial}{\partial y}\epsilon(x,y)\right]E_y \tag{2.51b}$$

Applying the representation in Eq. (2.46), the Eq. (2.51) can be represented in the form of a matrix eigenvalue problem

$$\gamma^2\begin{bmatrix}\hat{\boldsymbol{E}}_x\\ \hat{\boldsymbol{E}}_y\end{bmatrix} = \begin{bmatrix}\hat{\boldsymbol{M}}_{xx} & \hat{\boldsymbol{M}}_{xx}\\ \hat{\boldsymbol{M}}_{yx} & \hat{\boldsymbol{M}}_{yy}\end{bmatrix}\begin{bmatrix}\hat{\boldsymbol{E}}_x\\ \hat{\boldsymbol{E}}_y\end{bmatrix}, \tag{2.52}$$

where $\hat{\boldsymbol{E}}_x$ and $\hat{\boldsymbol{E}}_y$ denote the vectors containing the Fourier coefficient $E_{x,mn}$ and $E_{y,mn}$. Taking account to Laurent's rule and inverse rule for calculating the products of the Fourier

coefficients, we develop the following equations for the elements of the matrix $\boldsymbol{M}$

$$\hat{\boldsymbol{M}}_{xx} = k^2[\![\epsilon_{xy}]\!] - \mathrm{diag}(\hat{\boldsymbol{k}}_y)\mathrm{diag}(\hat{\boldsymbol{k}}_y) - \mathrm{diag}(\hat{\boldsymbol{k}}_x)[\![\epsilon]\!]^{-1}\mathrm{diag}(\hat{\boldsymbol{k}}_x)[\![\epsilon_{xy}]\!] \tag{2.53a}$$

$$\hat{\boldsymbol{M}}_{yy} = k^2[\![\epsilon_{yx}]\!] - \mathrm{diag}(\hat{\boldsymbol{k}}_x)\mathrm{diag}(\hat{\boldsymbol{k}}_x) - \mathrm{diag}(\hat{\boldsymbol{k}}_y)[\![\epsilon]\!]^{-1}\mathrm{diag}(\hat{\boldsymbol{k}}_y)[\![\epsilon_{yx}]\!] \tag{2.53b}$$

$$\hat{\boldsymbol{M}}_{xy} = \mathrm{diag}(\hat{\boldsymbol{k}}_x)\mathrm{diag}(\hat{\boldsymbol{k}}_y) - \mathrm{diag}(\hat{\boldsymbol{k}}_x)[\![\epsilon]\!]^{-1}\mathrm{diag}(\hat{\boldsymbol{k}}_y)[\![\epsilon_{yx}]\!] \tag{2.53c}$$

$$\hat{\boldsymbol{M}}_{yx} = \mathrm{diag}(\hat{\boldsymbol{k}}_y)\mathrm{diag}(\hat{\boldsymbol{k}}_x) - \mathrm{diag}(\hat{\boldsymbol{k}}_y)[\![\epsilon]\!]^{-1}\mathrm{diag}(\hat{\boldsymbol{k}}_x)[\![\epsilon_{xy}]\!]. \tag{2.53d}$$

The variables $k_{x,m}$ and $k_{y,n}$ constitute the elements of the diagonal matrices $\mathrm{diag}(\hat{\boldsymbol{k}}_x)$ and $\mathrm{diag}(\hat{\boldsymbol{k}}_y)$ and the Toeplitz matrices $[\![\epsilon]\!]$ contain the Fourier coefficiencts of the complex relative permittivity calculated with the Laurent's rule and inverse rule [63]. Applying the boundary conditions of electromagnetic in Eq. (2.4) we find that the permittivity is discontinuous in the both $x$ and $y$-directions, $E_x$ has discontinuities in the x-direction and the $E_y$ is discontinuous in the y-direction. The fact is that the inverse rule should be applied in the electric field calculation in Fourier domain.

By solving the eigenmodes from Eq. (2.52), we can represent the electric field in the $j$-th layer as

$$E_x,\, j(x,y,z) = \sum_l A_{l,j}\exp\big[i\gamma_{l,j}(z-h_{j-1})\big] + B_{l,j}\exp\big[-i\gamma_{l,j}(z-h_j)\big] \tag{2.54a}$$
$$\times \sum_{m,n} E^j_{x,mnl}\exp\big[i(k_{x,m}x + k_{y,n}y)\big]$$

$$E_y,\, j(x,y,z) = \sum_l A_{l,j}\exp\big[i\gamma_{l,j}(z-h_{j-1})\big] + B_{l,j}\exp\big[-i\gamma_{l,j}(z-h_j)\big] \tag{2.54b}$$
$$\times \sum_{m,n} E^j_{y,mnl}\exp\big[i(k_{x,m}x + k_{y,n}y)\big]$$

Corresponding representations of the magnetic field inside the stacked layer are obtained from Maxwell's equation.

### 2.4.6 Calculating the field distribution

The Equation (2.4) shows that $x$ and $y$- components electric field and magnetic field $E_x$, $E_y$, $H_x$, and $H_y$ are continuous across the boundary $h_j$. Hence, we arrive at the matrix equation

$$\begin{bmatrix} \boldsymbol{E}_{j+1} & -\boldsymbol{E}_j \\ \boldsymbol{H}_{j+1} & \boldsymbol{H}_j \end{bmatrix}\begin{bmatrix} \boldsymbol{A}_{j+1} \\ \boldsymbol{B}_j \end{bmatrix} = \begin{bmatrix} \boldsymbol{E}_{j+1}\boldsymbol{X}_{j+1} & -\boldsymbol{E}_j\boldsymbol{X}_j \\ \boldsymbol{H}_{j+1}\boldsymbol{X}_{j+1} & \boldsymbol{H}_j\boldsymbol{X}_j \end{bmatrix}\begin{bmatrix} \boldsymbol{A}_j \\ \boldsymbol{B}_{j+1} \end{bmatrix}, \tag{2.55}$$

where $\boldsymbol{X}_k$ is a diagonal matrix with elements $\exp\big[i\gamma_{j,l}(h_{j+1}-h_j)\big]$ and the vectors $\boldsymbol{A}_j$ and $\boldsymbol{B}_j$ contain the complex amplitudes of the modes. The $\boldsymbol{E}_j$ and $\boldsymbol{H}_j$ consist of the eigenvectors of the electric and magnetic fields for both $x$- and $y$-components. To simulate evanescent waves at the boundaries with numerically stable treatment, we use the S-matrix algorithm. We presented the scattered field as a function of the illuminating field in Eq. (2.55) which yields a

local S-matrix

$$\boldsymbol{S}^{(j)} = \begin{bmatrix} \boldsymbol{E}_{j+1} & -\boldsymbol{E}_j \\ \boldsymbol{H}_{j+1} & \boldsymbol{H}_j \end{bmatrix}^{-1} \begin{bmatrix} \boldsymbol{E}_{j+1}\boldsymbol{X}_{j+1} & -\boldsymbol{E}_j\boldsymbol{X}_j \\ \boldsymbol{H}_{j+1}\boldsymbol{X}_{j+1} & \boldsymbol{H}_j\boldsymbol{X}_j \end{bmatrix} \tag{2.56}$$

We can compose an S matrix related to each boundary and if only the reflected and transmitted amplitudes are interested, one may combine the local $S^{(j)}$ matrices to form the global scattering matrix $\boldsymbol{S}$ by using the recursion formula known as Redheffer's star product [109, 113] by

$$\boldsymbol{S} = \boldsymbol{S}^{(2)} * \boldsymbol{S}^{(1)} * \cdots \boldsymbol{S}^{(J-1)} * \boldsymbol{S}^{(J)} \tag{2.57}$$

where the star product is defined as

$$\begin{aligned} \mathbf{A} * \mathbf{B} &= \begin{bmatrix} \mathbf{a}_{11} & \mathbf{a}_{12} \\ \mathbf{a}_{21} & \mathbf{a}_{22} \end{bmatrix} * \begin{bmatrix} \mathbf{b}_{11} & \mathbf{b}_{12} \\ \mathbf{b}_{21} & \mathbf{b}_{22} \end{bmatrix} \\ &= \begin{bmatrix} \mathbf{b}_{11}(\mathbf{I}-\mathbf{a}_{12}\mathbf{b}_{21})^{-1}\mathbf{a}_{11} & \mathbf{b}_{12}+\mathbf{b}_{11}\mathbf{a}_{12}(\mathbf{I}-\mathbf{b}_{21}\mathbf{a}_{12})^{-1}\mathbf{b}_{22} \\ \mathbf{a}_{21}+\mathbf{a}_{22}\mathbf{b}_{21}(\mathbf{I}-\mathbf{a}_{12}\mathbf{b}_{21})^{-1}\mathbf{a}_{11} & \mathbf{a}_{22}(\mathbf{I}-\mathbf{b}_{21}\mathbf{a}_{12})^{-1}\mathbf{b}_{22} \end{bmatrix}, \end{aligned} \tag{2.58}$$

where $\mathbf{a}_{11}$ and $\mathbf{b}_{11}$, etc, are also square matrices. Having constructed the matrix $\boldsymbol{S}$, we can write the relation between the incident and the scattered field in the form

$$\begin{bmatrix} \boldsymbol{T} \\ \boldsymbol{R} \end{bmatrix} = \boldsymbol{S} \begin{bmatrix} \boldsymbol{\delta} \\ \mathbf{0} \end{bmatrix} \tag{2.59}$$

where $T$ and $R$ contain the complex amplitudes related to the x and y-components of the transmitted and reflected electric fields, and $\delta$ denotes the angular spectrum of the illuminating plane wave. The difracion efficiencies of the scttered field are commonly the matter of main interest with diffraction gratings. The time averaged z-component of the Poynting vector gives the relations

$$\eta_{R_{mn}} = \mathrm{Re}(\gamma^R_{mn}/\gamma_{00})|\boldsymbol{R}_{mn}|^2 \tag{2.60a}$$

$$\eta_{T_{mn}} = \mathrm{Re}(\gamma^T_{mn}/\gamma_{00})|\boldsymbol{T}_{mn}|^2 \tag{2.60b}$$

for the reflected ad transmitted efficiencies.

### 2.4.7 Truncation procedure

Choosing a suitable truncation order, one should carefully keep in view some fundamental aspects of FMM. Increasing the truncation parameter $N$, i.e., the Fourier coefficients included in the analysis are between $-N$ and $N$) to value $2N+1$, we observe that the computation time may easily even double since the number of the elements in the matrices is approximately comparable to the fourth power of $N$. Thus all improvements in convergence, even small

ones, are of major interest with gratings. Usually, the Fourier coefficients taken into account form a rectangular area, but Li et al. showed that the convergence is enhanced when a circular truncation is utilized.

The electromagnetic fields are represented by Fourier expansions in our system. The numerical inaccuracies of calculation mainly occur due to the inevitable truncation of the Fourier series. To evaluate the accuracy of our numerical results, we analyze the convergence of simulation in our grating generating $7 \times 7$ spot array from the main text with incrementally increasing the number of Fourier modes. This defines the set of Fourier harmonics retained in x and y-axis from $-N$ to $N$, respectively. In other words, the number of Fourier modes is $2N+1$ in each axis. The plot in Fig. 2.9 present the diffraction efficiency in $[0,0]^{\text{th}}$ and $[3,3]^{\text{th}}$ order of grating with different number of modes $N$. The zeroth-order normally indicate slower convergence than off-axis orders. In the Fig. 2.9, when $N$ is large enough ( e.g. $N > 10$), all of the simulations converge to within 1 % of same value. To obtain accurate converged calculation, we thus use this value for the optimization process and final calculation of optimized devices reproduces with a enough high number of modes, e.g., in this case $N = 25$. All theoretical results presented in this work use enough high number of modes to show equivalent numerical accuracies.

In summary, the principle of the method is to present the refractive index profile and the field inside the grating region as a Fourier series. The eigenvalue equation is solved for the waveguide modes in each slice. Finally, the resulting field expansion is matched at the interfaces of the slices with the boundary conditions under considering polarization of incident wave. The number of eigenmodes taken into count needs to be chosen to sufficiently large [63]. The parameter is defined as $N$, which is referred to as Fourier orders $-N:N$. The accuracy of the simulation depends on this parameter [61]. The convergence of the calculations has to be checked by simulating the diffraction efficiency as a function of the number of Fourier orders. If the efficiency reaches a stable value, the number of Fourier orders is high enough to ensure reliable results.

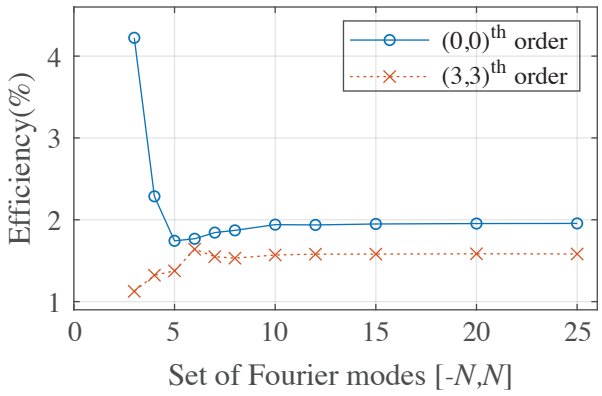


Figure 2.9 – Convergence analysis for diffraction efficiency of two-dimensional grating generating 7 x 7 spot array

## 2.5 Inverse design methods

In previous sections, we briefly reviewed the methods to predicting the electromagnetic phenomena in diffrative elements such as TEA and RCWA. They are all meant to solve the "forward problem", which is to calculate the fields for a given structure. However, one is typically more interested in "inverse problem", which is to find the geometry for a desired electromagnetic response. Normally, the inverse problem is more difficult than the forward problem. In the forward problem case, there is obviously only one solution with a given geometry and sources. But, for the inverse problem, most of case we cannot expect the unique geometry for specified fields , or there may be no exact solution. Hence, in general, we try to find a structure that satisfies the desired electromagnetic field the most closely. From this viewpoint, inverse design problems may called optimization problems.

To optimize an optical element, the element parameterized by several design variables, such as geometric or material parameters. The desired performance of the optical element is defined mathematically through an figure of merit (FOM), also known as merit function, we then find the set of design parameters either minimizing or maximizing FOM using mathematical and computational optimization techniques. There are many possible approaches to the inverse design problem. The measure of optimization tool chain is its ability to efficiently search such a large design parameter space. In general, the most time-consuming part of the inverse design is the solution of the forward problem, which is generally repeated for many different set of design parameters ,e.g., stochastic algorithms [81, 114–118] , genetic algorithms [119–123]. But, if optical propagation model from the input source to the output field can be inverted, the number of simulations required by the approach is significant less than general case. Otherwise, we have no choice but to rely on the gradient-based optimization. We briefly introduce to these two cases.

### 2.5.1 Evaluation of diffractive beam splitters

For many applications, the goal is to propagate to all the light in the desired orders and avoid losses. To quantify the amount of light that propagates in the desired diffraction orders, we define the diffraction efficiency $\eta_{mn}$ as the ratio of the sum of the intensities of all desired orders to the total intensity of the incident beam,

$$\eta_{\text{total}} = \sum_{m,n} \frac{I_{m,n}}{I_{\text{in}}} = \sum_{m,n} \eta_{mn}. \tag{2.61}$$

The $\eta_{mn}$ is the diffraction efficiency in orders on 2D array and $m$,$n$ is the diffraction order along horizontal and vertical axis, respectively (see Fig. 1.1(a)) . Diffractive fan-out elements which produce a set of uniformly illuminated diffraction orders, are commonly used to various cases, while some applications potentially require diffractive beam splitters with various intensity distributions. To evaluate diffractive beam spiltter with various diffraction efficiency distribution, we define uniformity error (UE) and normalized root-mean-square error (NRMS)

$\sigma$ as follows:

$$UE = \frac{\eta_{\max} - \eta_{\min}}{\eta_{\max} + \eta_{\min}} \tag{2.62}$$

$$\sigma = \sqrt{\frac{1}{T}\sum_{m,n}\left(\frac{\eta_{mn} - \eta_{\text{obj}}}{\eta_{\text{obj}}}\right)^2} \tag{2.63}$$

where $\eta_{\max}$ and $\eta_{\min}$ represent the maximal and minimum intensity of the diffraction efficiency. $T$ is the total number of target diffraction orders. The spot energy distribution can be designed for any distribution meeting the application's requirements. The NRMS with scaled diffraction efficiency $\tilde{\eta}$ is preferable to with normal diffraction efficiency $\eta$ because normalizing root-mean square error facilitates the comparison among various diffraction efficiency distributions with different scales from diverse DOEs. Lower values of both UE and NRMS indicate less residual variance so that our objective is to minimize UE and NRMS of a DOE design given certain diffraction efficiency distribution.

### 2.5.2 Iterative Fourier transform algorithm

In the far-field region, the spatial or angular region where the properties of the signal are specified is called signal area. And the plane immediately after the diffractive element is named as the element plane. The IFTA is one of the most common inverse methods for designing the diffractive elements in paraxial domain [36, 50, 124–127]. The basic idea behind the IFTA is based on TEA as shown in Section 2.3, which is a Fourier transform pair between the field in the element plane and the diffraction orders of the field in far-field region. The field is propagated forward and backward between the domains applying suitable constraints during the iterative process as shown in Fig. 2.10.

Starting from the distribution of target diffraction amplitudes in signal area, we define the complex amplitude of the field by adding some initial phase to amplitude information. The generated diffraction amplitudes can be used to calculate the field in the element plane by inverse Fourier transform in Eq. (2.28). This obtained field is a complex valued function with freely fluctuating amplitude and phase, but an element generating such a field cannot be fabricated with normal methods and thus the fabrication constraints such as quantization and minimum feature size are considered. Then the complex amplitudes of the diffraction orders in far-field are calculated by Fourier transform. There will be some noise which are the signals in unwanted diffraction orders, and we remove it by resetting the field amplitude to the goal diffraction distribution. By continuing the iteration this way the algorithm eventually converges to a local minimum representing the element phase which produces the target intensity distribution at the signal area. In order to avoid stagnation of the iteration process, some modification of the algorithm have to be made. For instance, by allowing the intensity outside of signal area, it will be enhance the convergence so that obtain improved uniformity,

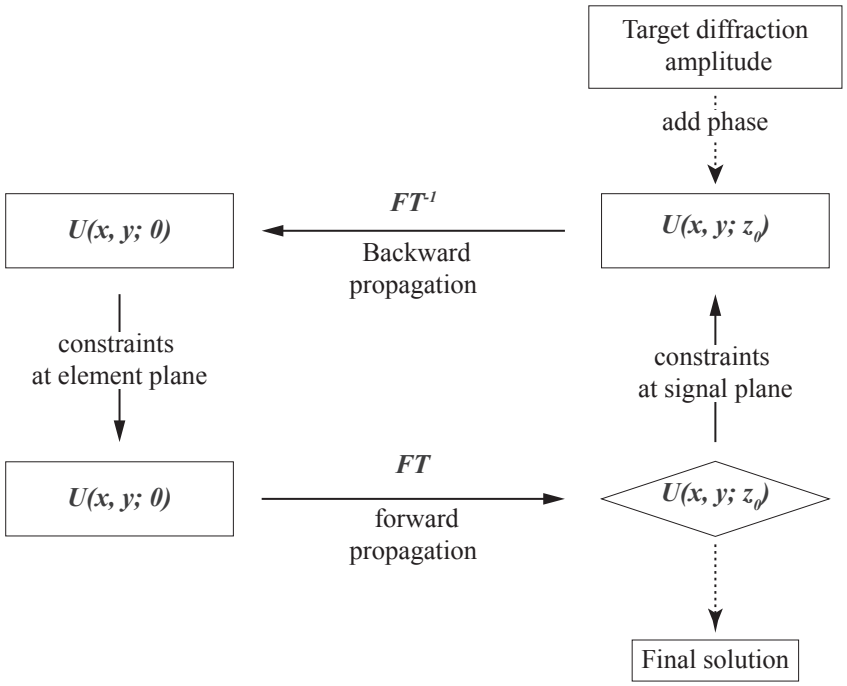


Figure 2.10 – Flowchart of iterative Foureir transform algorithm. The left-hand column represent the element plane and the signal plane is on the right.

although the total diffraction efficiency is slightly decreased. Also, the choice of initial phase can have an effect on the quality of the results because the method converges to the nearest solution.

The method is very computationally efficient due to the use of the fast Fourier transform algorithm, and versatile because concerning possible constraints imposed by both the element plane and the diffraction orders. However, one should keep in mind that, as a method based on the TEA, IFTA is valid only when the geometry is paraxial.

### 2.5.3 Limitation of IFTA

IFTA does not take into account the actual physical process, resulting in the inaccuracy of the calculating for the diffraction efficiency of devices with small features. To evaluate the performance of DOEs designed by IFTA in the non-paraxial domain, we prepared a $7 \times 7$ diffractive beam splitter generated by IFTA (see Fig. 2.11 inset). The plot in Fig. 2.11 show the UE and NRMS of grating with the different grating period. In Fig. 2.11, the maximum diffraction angle indicate the angle from $0^{th}$ order to the highest target diffraction order. To analyze the diffraction efficiencies in orders, we calculated the UE in off-axis, i.e. excluding the zeroth-order which has usually the largest intensity variation with respect to the change of grating period. In these simulations, we use the RCWA to calculate the diffraction efficiency with an incident beam of 940 nm wavelength. when the grating is shrunk, i.e. the size of

structures in the gratings becomes comparable with the wavelength of the incident light, the device designed by IFTA is no more valid. The diffraction angle is proportional to the ratio of the wavelength of the incident light as given by Eq. (2.41). Thus, we need to the adjoint method based on rigorous diffraction theory to optimize wide angle DOEs in the non-paraxial domain.

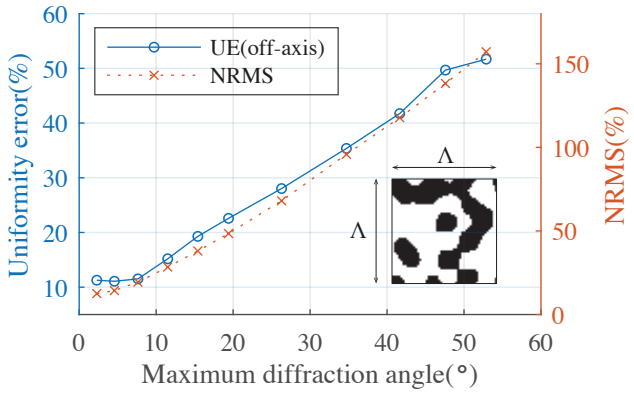


Figure 2.11 – Uniformity of 7 × 7 diffractive beam splitter designed by IFTA as a function of grating period Λ. The insets show the layout of the single unit cell. Black represents dielectric material and white represents air.

### 2.5.4 Gradient-based optimization

If the diffractive elements features are below the wavelength scale, the rigorous diffraction theory is used and the design has to be made by parametric optimization. Typically, this is performed using gradient-based optimization techniques, which use local gradient information to iteratively progress through the design space. In inverse design problems with several degrees of freedom, gradient-based methods generally converge on local minima much faster than global optimization techniques such as particle swarm optimization [114] or genetic algorithms[119], which typically do not use local gradient information.

To achieve an optimal diffractive beam splitter generating the desired target distribution,e.g., often the uniform array , we define the FOM as

$$F\left(s(\mathbf{p})\right) = \sum_{m,n} \left[\eta_{mn}\left(s(\mathbf{p})\right) - \eta_{\text{obj}}\right]^2, \tag{2.64}$$

where $s(\mathbf{p})$ is shape function described by the set of design parameter, for example, the position of the transition points or the pixel of the geometry.

Through the gradient-based optimization, one updates from an old structure as described by a set of design parameters $s^{\text{old}}\left(\mathbf{p}\right)$ to a new structure as described as a set of design parameters

$s^{\text{new}}(\mathbf{p})$ with in each iteration,

$$s^{\text{new}}(\mathbf{p}) = s^{\text{old}}(\mathbf{p}) + \alpha \cdot \Delta s(\mathbf{p}), \tag{2.65}$$

where $\alpha$ is the learning rate which is an important value determining how big of an update which is often referred to as a line search [128]. The process of finding appropriate value of $\alpha$ is therefore a good measure of various gradient-based approach's efficiency. In this work, we perform updates of the design variables using the limited-memory Broyden-Fletcher-Goldfarb-Shanno (L-BFGS) algorithm [129, 130] because it produces superior convergence compared to the other method such as steepest decent [131, 132] and conjugate gradient method [133].

In this Eq. (2.65), $\Delta s(\mathbf{p})$ is the search direction which is related to the gradient of the FOM $\boldsymbol{\nabla}_{s(\mathbf{p})} F$ with respect to $s(\mathbf{p})$. If we calculate the gradient of FOM efficiently, for instance, accessing the analytical solution of the gradient or computing the gradient using adjoint method, we would have optimization tools for wide angle DOEs using gradient-based methods.

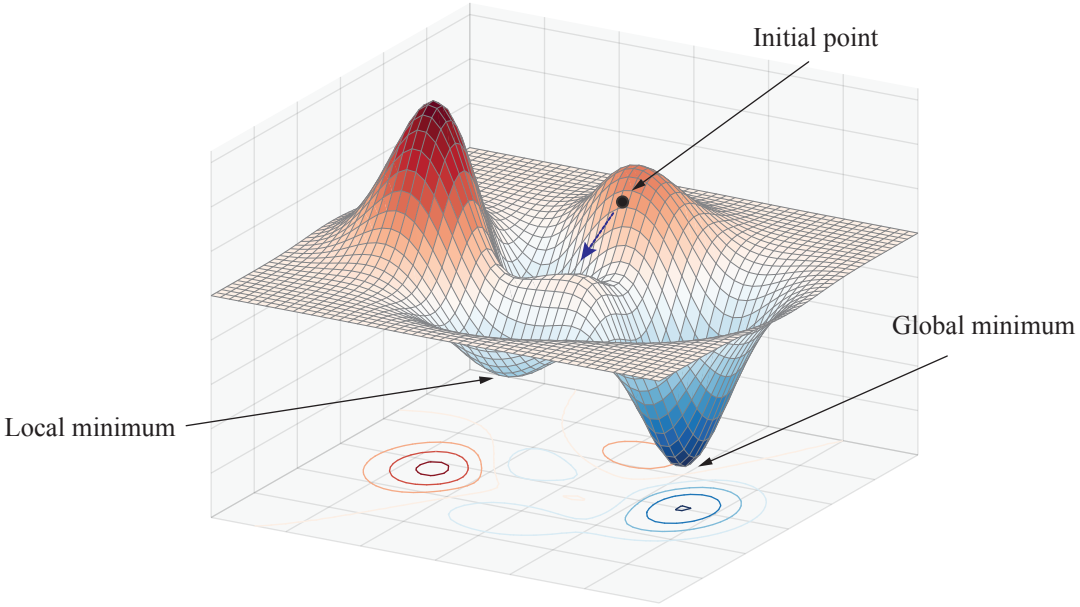


Figure 2.12 – Scheme of gradient-based optimization

# 3 Optimization based on Perturbation Approach

In this chapter, we introduce the gradient-based optimization method for wide angle DOEs operating in the complex diffraction regimes beyond scalar paraxial theory, e.g., thin element approximation. It will allow us to calculate the gradient of FOM efficiently with an analytical solution. For this purpose, a diffraction model is required that permits to describe analytically the gradient of diffraction efficiency with respect to the design variables as well as efficient diffraction analysis of DOEs in the non-paraxial domain. We introduce such a diffraction model: step transition perturbation approach (STPA) [134]. The STPA is an approximate method based on local field perturbations generated by sharp transitions of the surface profile of diffractive elements.

Here, we discuss a design approach based on STPA for wide angle one-dimensional gratings, yielding improvements in the uniformity of the generated patterns while maintaining the total diffraction efficiency. Section 3.1 describes the fundamental diffractive geometry and the basic principle of the method. The method with a precise mathematical description and minimum requirements for the accuracy of calculation is also given. Section 3.2 then explains the process of optimization based on STPA. We can describe analytically the gradient of diffraction efficiency with respect to the design variables of optical elements using STPA. Thus, we use gradient-based optimization using the gradient of the figure of merit (FOM) calculated by STPA. With this computational implementation, Section 3.3 shows the optimization results of diffractive fan-out grating creating a one-dimensional spot array. The results of the experimental characterization are also discussed.

## 3.1 Step transition perturbation approach

An important aspect of the optimization process is to parameterize the shape of the optical elements, which can significantly affect the performance and computational cost. In the previous chapter, the Figure 2.4 illustrates a cross-section view of a part of a general surface profile of binary (i.e., 2-level) grating with $2K$ transitions in position $x_k$ within a single grating period. We use these positions of transition points as the set of design parameters $\mathbf{x}_k$ =

$[x_1 \cdots x_k \cdots x_{2K}]$.

This approximative method has been introduced by Kettunen et al. [135] and later reformulated by Vallius et al. [58, 134, 136] that in fact the approximated method based on local field perturbations from sharp step-transitions enables rapid calculation of diffraction patterns of DOEs in the non-paraxial domain.

### 3.1.1 Field perturbations

The surface profile of binary grating clearly consists of locally sharp transitions between different height levels. Let us consider the effect of a single step transition on the amplitude and phase of a normally incident plane wave illumination as shown in Fig. 3.1. In Fig. 3.1, the TE-polarized plane wave is illuminated from bottom $z = 0$ and the observation plane in the plane $z = 4$. A significant perturbation is observed in the phase and amplitude of the field distribution directly after a sharp vertical transition determined by rigorous electromagnetic theory. The TEA calculation, however, yields a constant amplitude and phase corresponding to the phase shift by the height of the step transition. In Fig. 3.1(b) and (c), the normalized amplitude and phase of the field distribution after the step transition determined by TEA and RCWA is presented. The phase and amplitude modulation and function form of both calculated by RCWA depends on the step height and also on the state of polarization of the incident wave. This omission of perturbations in TEA makes computing inaccurate especially gratings with wavelength-scale structures, i.e., the gratings creating the wide angle arrays. Thus, we can accurately calculate the diffraction efficiency using the model which combines the TEA with field disturbances caused by sharp transitions in the surface profile calculated by RCWA. We define the field perturbation behind the $k$:th sharp transition located at the point $x_k$ in the surface profile as

$$p_k(x) = \begin{cases} U_k^R(x) - U_k^T(x) & \text{if } |x| < \Delta_T \\ 0 & \text{elsewhere} \end{cases} \tag{3.1}$$

where $U_k^R(x)$ and $U_k^T(x)$ are field calculated by RCWA and TEA, respectively and truncation parameter $\Delta_T = 10\lambda$ is chosen in the calculations [136]. If adjacent transitions in the optical elements are sufficiently distant (approximately one optical wavelength [135]), the field perturbation caused by them can be added coherently without making a considerable error.

The field perturbations of binary diffractive elements consist of only two kinds of oscillation corresponding to left-side and right-side transition point in a ridge. Therefore, the constructed field $U(x)$ behind a binary grating with many transition points is described by the coherent sum of two kinds field perturbations $p_1(x)$ and $p_2(x)$ added to the transmitted field given by

TEA in the following expression:

$$\begin{aligned} U(x) &= U^T(x) + \sum_{k=1}^{2K} p_k(x) \\ &= U^T(x) + \sum_{k=1}^{K} p_1(x - x_{2k-1}) + \sum_{k=1}^{K} p_2(x - x_{2k}) \end{aligned} \tag{3.2}$$

where $2K$ is the total number of the transitions. The amplitude and phase of the field perturbation of right-side of a ridge $p_2(x)$ is represented in Fig. 3.1(d) and (f). Then, the diffraction pattern behind the surface profile can be obtained by propagating the resulting field $U(x)$ with the use of standard algorithms such as the angular spectrum representation of the electromagnetic field. We can calculate the diffraction efficiency more efficiently using the Fourier shift theorem.

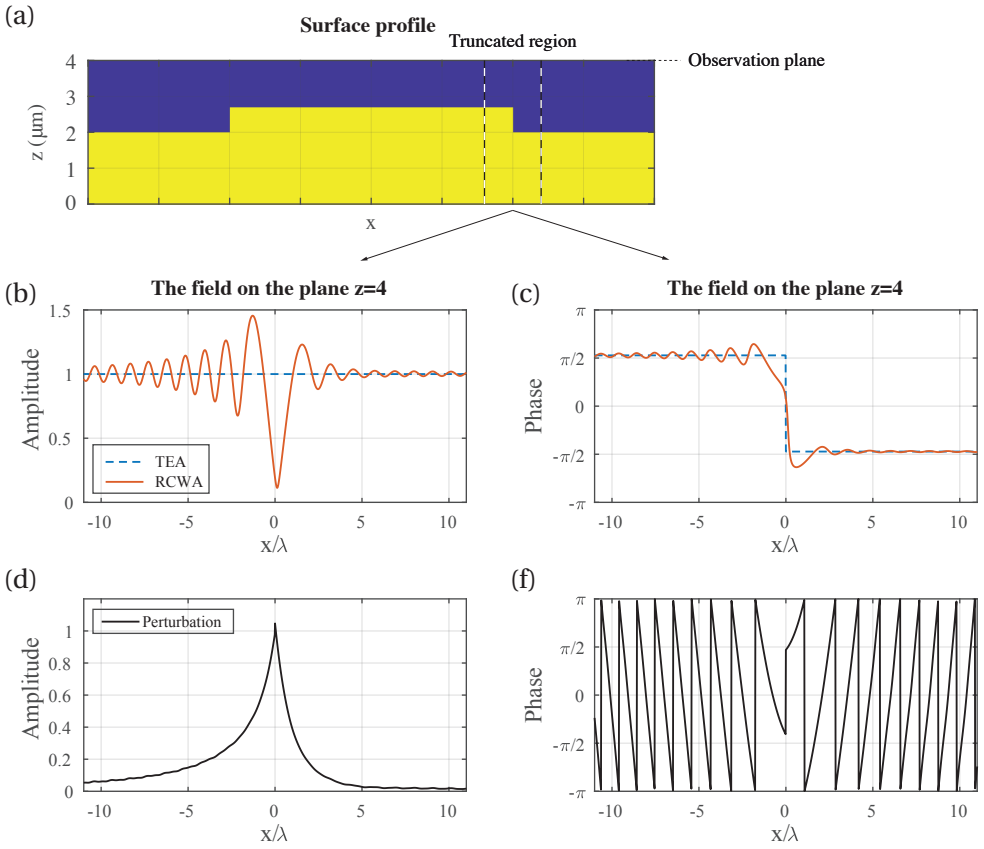


Figure 3.1 – (a) The surface profile with sharp transition points. observation plane and truncated region are represented. (b) The amplitude and (c) phase of the electric field in TE-polarization and after the sharp vertical surface profile with a transition point corresponding to a phase delay of $\pi$ radians calculated by RCWA (red line) and TEA (blue dotted line). The (d) amplitude and (e) phase of corresponding perturbations in Eq. (3.1) are shown.

### 3.1.2 Perturbations in the Fourier domain

We calculate the effect of a single perturbation from a transition in the Fourier domain and finally combine the perturbations associated with all transitions in the diffractive elements. For periodic structures such as grating, the Fourier spectrum is discrete, and the complex amplitudes due to transitions in both left-side and right-side of a ridge $p_1, p_2$ in Fourier domain are given by

$$P_m = \frac{1}{\Lambda}\int_0^{\Lambda} p_1(x)\exp(-i2\pi mx/\Lambda)dx \tag{3.3a}$$

$$P_{-m} = \frac{1}{\Lambda}\int_0^{\Lambda} p_2(x)\exp(-i2\pi mx/\Lambda)dx \tag{3.3b}$$

where $m$ is the index of the diffraction order and $\Lambda$ is grating period of the element. The Fourier coefficient of complex amplitudes caused by a transition in right-side of a ridge $p_2(x)$ is $P_{-m}$ because the $p_2(x)$ is an even function of $p_1(x)$.

According to Fourier shift theorem [30, 137], if the transition is located at $x = x_k$ instead of at the origin, this transverse shift of transition implies multiplication of $P_m$ or $P_{-m}$ by factor of $\exp(-i2\pi mx_k/\Lambda)$. Therefore, the superposition of Fourier domain corresponding to the total field $U(x)$ in Eq. (3.2) is expressed as a sum of the Fourier coefficient of field calculated by TEA and the perturbations:

$$\begin{aligned} A_m &= \frac{1}{\Lambda}\int_0^{\Lambda} U(x)\exp\left(-i\frac{2\pi mx}{\Lambda}\right)dx \\ &= T_m + D_m \end{aligned} \tag{3.4}$$

where $T_m$ and $D_m$ is the Fourier coefficient of the field calculated by TEA and the field perturbations contribution, respectively.

$$T_m = \frac{1}{\Lambda}\int_0^{\Lambda} U^T(x)\exp\left(-i\frac{2\pi mx}{\Lambda}\right)dx \tag{3.5a}$$

$$D_m = P_m\sum_{k=1}^{K}\exp(-i2\pi mx_{2k-1}/\Lambda) + P_{-m}\sum_{k=1}^{K}\exp(-i2\pi mx_{2k}/\Lambda) \tag{3.5b}$$

Once the Fourier coefficient of the step-transition perturbation $P_m$ and $P_{-m}$ in Eq. (3.3) is calculated and no further RCWA calculations are necessary no matter how many the features in the diffractive element. It permits the computation of the diffraction amplitude $A_m$ from the Fourier coefficient obtained by TEA simply by adding precalculated Fourier domain contributions $P-m$ and $Pm$ from left- and right-side step transition, with appropriate phase shifts depending on the location $x_{2k-1}$ and $x_{2k}$ of the transitions.

### 3.1.3 Diffraction efficiency

The diffraction efficiencies $\eta_m$ can be express as

$$\eta_m = |A_m|^2 = |T_m|^2 + |D_m|^2 + T_m^* D_m + T_m D_m^* \tag{3.6}$$

where the $m$:th order Fourier coefficients $T_m$ and $D_m$ are given by Eqs. (3.4) and (3.5). In binary grating case such as Figure 2.4, we can represent the square module of the Fourier coefficients in the following form:

$$|T_m|^2 = \Phi_m{}^2 (C_{1m}{}^2 + S_{1m}{}^2) \tag{3.7a}$$

$$\begin{aligned} |D_m|^2 = {} & |P_m|^2 (C_{2m}{}^2 + S_{2m}{}^2) + |P_{-m}|^2 (C_{3m}{}^2 + S_{3m}{}^2) \\ & + 2\,\mathrm{Re}(P_m P_{-m}^*)(C_{2m}C_{3m} + S_{2m}S_{3m}) \\ & - 2\,\mathrm{Im}(P_m P_{-m}^*)(C_{2m}S_{3m} - S_{2m}C_{3m}) \end{aligned} \tag{3.7b}$$

$$\begin{aligned} T_m^* D_m + T_m D_m^* = {} & \Phi_m \left[ 2\,\mathrm{Re}(P_m)\left(C_{1m}C_{2m} + S_{1m}S_{2m}\right) + 2\,\mathrm{Re}(P_{-m})\left(C_{1m}C_{3m} + S_{1m}S_{3m}\right) \right. \\ & \left. + 2\,\mathrm{Im}(P_m)\left(C_{1m}S_{2m} - S_{1m}C_{2m}\right) + 2\,\mathrm{Im}(P_{-m})\left(C_{1m}S_{3m} - S_{1m}C_{3m}\right) \right] \end{aligned} \tag{3.7c}$$

where

$$\Phi_m = \sin\left(\Delta\phi/2\right)/\pi m \tag{3.8a}$$

$$C_{1m} = \sum_{k=1}^{2K} (-1)^k \cos(2\pi m x_k/\Lambda), \qquad S_{1m} = \sum_{k=1}^{2K} (-1)^k \sin(2\pi m x_k/\Lambda) \tag{3.8b}$$

$$C_{2m} = \sum_{k=1}^{K} \cos(2\pi m x_{2k-1}/\Lambda), \qquad S_{2m} = \sum_{k=1}^{K} \sin(2\pi m x_{2k-1}/\Lambda) \tag{3.8c}$$

$$C_{3m} = \sum_{k=1}^{K} \cos(2\pi m x_{2k}/\Lambda), \qquad S_{3m} = \sum_{k=1}^{K} \sin(2\pi m x_{2k}/\Lambda) \tag{3.8d}$$

where the $\Delta\phi$ is the difference between phase $\phi_1$ and $\phi_2$ which are the phase of an electric field in the air and dielectric material, respectively and $2K$ is the number of transition point in structure. The Fourier coefficients $P_m$ and $P_{-m}$ of field perturbation are given by Eq. (3.3), which are constant values with respect to transition point $x_k$. Thus the values $\mathrm{Re}(P_m)$, $\mathrm{Re}(P_{-m})$, $\mathrm{Im}(P_m)$, $\mathrm{Im}(P_{-m})$, $\mathrm{Re}(P_m P_{-m}^*)$ and $\mathrm{Im}(P_m P_{-m}^*)$ also constant with respect to transition point $x_k$. The Equation (3.7) is only valid in $m \neq 0$. The diffraction efficiency in zero order $\eta_0$ is

expressed as

$$\begin{aligned}\eta_0 &= |T_0|^2 + |D_0|^2 + T_0^* D_0 + T_0 D_0^* \\ &= 1 - 4Q(1-Q)\sin^2(\Delta\phi/2) + 4K^2|P_0|^2 \\ &\quad - 4K\cdot \mathrm{Re}(P_0)\left\{\cos\phi_1 + 2\sin\left(\Delta\phi/2\right)\sin\left(\phi_s/2\right)Q\right\} \\ &\quad - 4K\cdot \mathrm{Im}(P_0)\left\{\sin\phi_1 - 2\sin\left(\Delta\phi/2\right)\cos\left(\phi_s/2\right)Q\right\}\end{aligned} \tag{3.9}$$

where $Q = \sum_{k=1}^{2K}(-1)^k x_k$ and $\phi_s = \phi_1 + \phi_2$. Therefore the diffraction efficiency $\eta_m$ can be expressed as a function as the transition point $x_k$.

## 3.2 Inverse design based on STPA

We furthermore focus on the fact that this Fourier-domain contribution from step transition $P_m$ doesn't contain explicit dependence on transition point $x_k$. This point is highly useful when calculating the gradient of diffraction efficiencies with respect to transitions positions which are design parameters in our examples. We define the FOM to optimize DOEs creating diffraction pattern with uniform intensity distribution:

$$F(\mathbf{x}_k) = \sum_{m=-M}^{M}\left[\eta_m(\mathbf{x}_k) - \eta_{\mathrm{obj}}\right]^2 \tag{3.10}$$

where $F$ represents the difference between the calculated diffraction efficiency $\eta_m$ and the target diffraction efficiency $\eta_{\mathrm{obj}}$ in diffraction orders with respect to the set of transition positions $\mathbf{x}_k = [x_1 \cdots x_k \cdots x_{2K}]$. The gradient of the FOM with respect to transition positions $\nabla_{\mathbf{x}_k} F$ is crucial in determining the search direction to optima. For example, if the total number of transitions $2K$ is large, it may easily become computationally heavy to calculate the gradient by RCWA analysis. The STPA, however, allows expressing the variation for a diffraction efficiency with respect to transition positions as an analytical solution so that it can calculate the gradient straightforwardly. This point is highly useful when calculating the gradient of diffraction efficiencies with respect to transitions positions $\nabla_{\mathbf{x}_k} F = \left[\frac{\partial F}{\partial x_1}, \cdots, \frac{\partial F}{\partial x_k}, \cdots, \frac{\partial F}{\partial x_{2K}}\right]$ to optimize the structures. To find these derivatives, we apply chain rule when differentiating the FOM:

$$\frac{\partial F}{\partial x_k} = \sum_{m=-M}^{M}\frac{\partial F}{\partial \eta_m}\cdot\frac{\partial \eta_m}{\partial x_k} = \sum_{m=-M}^{M}\frac{\partial F}{\partial \eta_m}\cdot\frac{\partial |T_m + D_m|^2}{\partial x_k} \tag{3.11}$$

where the first term $\frac{\partial F}{\partial \eta_m}$ is easily calculated by using Eq. (2.64) and the second term $\frac{\partial |T_m + D_m|^2}{\partial x_k}$ is also expressed by an analytical equation because because $P_m$ and $P_{-m}$ don't include the dependence on the position of transition point $x_k$. We represent the derivatives of the diffraction efficiencies as

$$\frac{\partial \eta_m}{\partial x_k} = \frac{\partial |T_m + D_m|^2}{\partial x_k} = \frac{\partial |T_m|^2}{\partial x_k} + \frac{\partial |D_m|^2}{\partial x_k} + \frac{\partial T_m^* D_m}{\partial x_k} + \frac{\partial T_m D_m^*}{\partial x_k} \tag{3.12}$$

where the diffraction efficiency $\eta_m$ is a function with respect to transition point $x_k$ in our examples. Thus we can partially differentiate each term of $\eta_m$ with respect to $x_k$. when $m \neq 0$, we can develop the derivatives as

$$\frac{\partial |T_m|^2}{\partial x_k} = 2{\Phi_m}^2 (C_{1m} {C_1}'_m + S_{1m} {S_1}'_m) \tag{3.13a}$$

$$\frac{\partial |D_m|^2}{\partial x_k} = \begin{cases} |P_m|^2 \left(C_{2m} C'_m + S_{2m} S'_m\right) \\ +2\,\mathrm{Re}\left(P_m P^*_{-m}\right)\left(C_{3m} C'_m + S_{3m} S'_m\right) \\ -2\,\mathrm{Im}\left(P_m P^*_{-m}\right)\left(S_{3m} C'_m - C_{3m} S'_m\right), \\ \qquad\qquad \text{for } k = 1,3,\cdots,2K-1 \\ |P_{-m}|^2 \left(C_{3m} C'_m + S_{3m} S'_m\right) \\ +2\,\mathrm{Re}\left(P_m P^*_{-m}\right)\left(C_{2m} C'_m + S_{2m} S'_m\right) \\ -2\,\mathrm{Im}\left(P_m P^*_{-m}\right)\left(C_{2m} S'_m - S_{2m} C'_m\right), \\ \qquad\qquad \text{for } k = 2,4,\cdots,2K \end{cases} \tag{3.13b}$$

$$\frac{\partial T^*_m D_m}{\partial x_k} + \frac{\partial T_m D^*_m}{\partial x_k} = \begin{cases} 2\Phi_m \left[\mathrm{Re}(P_m)\left(C_{1m} C'_m + C_{2m} {C_1}'_m + S_{1m} S'_m + S_{2m} {S_1}'_m\right)\right. \\ \quad + \mathrm{Im}(P_m)\left(C_{1m} S'_m - S_{1m} C'_m - C_{2m} {S_1}'_m + S_{2m} {C_1}'_m\right) \\ \quad + \mathrm{Re}(P_{-m})\left(C_{3m} {C_1}'_m + S_{3m} {S_1}'_m\right) \\ \quad \left. + \mathrm{Im}(P_{-m})\left(S_{3m} {C_1}'_m - C_{3m} {S_1}'_m\right)\right], \\ \qquad\qquad \text{for } k = 1,3,\cdots,2K-1 \\ 2\Phi_m \left[\mathrm{Re}(P_{-m})\left(C_{3m} {C_1}'_m + C_{1m} C'_m + S_{3m} {S_1}'_m + S_{1m} S'_m\right)\right. \\ \quad + \mathrm{Im}(P_{-m})\left(S_{3m} {C_1}'_m + C_{1m} S'_m - C_{3m} {S_1}'_m - S_{1m} C'_m\right) \\ \quad + \mathrm{Re}(P_m)\left(C_{2m} {C_1}'_m + S_{2m} {S_1}'_m\right) \\ \quad \left. + \mathrm{Im}(P_m)\left(S_{2m} {C_1}'_m - C_{2m} {S_1}'_m\right)\right], \\ \qquad\qquad \text{for } k = 2,4,\cdots,2K \end{cases} \tag{3.13c}$$

where

$${C_1}'_m = -\frac{2\pi m}{\Lambda}(-1)^k \sin(2\pi m x_k/\Lambda), \qquad {S_1}'_m = \frac{2\pi m}{\Lambda}(-1)^k \cos(2\pi m x_k/\Lambda) \tag{3.14a}$$

$$C'_m = -\frac{2\pi m}{\Lambda}\sin(2\pi m x_k/\Lambda), \qquad S'_m = \frac{2\pi m}{\Lambda}\cos(2\pi m x_k/\Lambda). \tag{3.14b}$$

The other variables are given by Eq. (3.8). If $m = 0$, the derivatives of the diffraction efficiency

in zero order is represented to

$$\begin{aligned}\frac{\partial \eta_0}{\partial x_k} =& -4Q'(1-2Q)\sin^2(\Delta\phi/2) \\ &-8K\cdot \mathrm{Re}(P_m)\sin\big(\Delta\phi/2\big)\sin\big(\phi_s/2\big)Q' \\ &+8K\cdot \mathrm{Im}(P_m)\sin\big(\Delta\phi/2\big)\cos\big(\phi_s/2\big)Q'\end{aligned} \tag{3.15}$$

where $Q=\sum_{k=1}^{2K}(-1)^k x_k$, $Q'=\frac{(-1)^k}{\Lambda}$, and $\phi_s=\phi_1+\phi_2$. Therefore, we can express the gradient of diffraction efficiency with respect to transition points based on STPA as an analytical solution.

It is feasible to calculate the gradient straightforwardly with accuracy as much as the approach based on the rigorous method if most of the features of the structure are bigger than the wavelength of the incident light. The obtained gradient was used in optimization based on the limited-memory Broyden-Fletcher-Goldfarb-Shanno (L-BFGS) algorithm [129, 130]. The workflow of inverse design based on STPA is shown in Fig. 3.2.

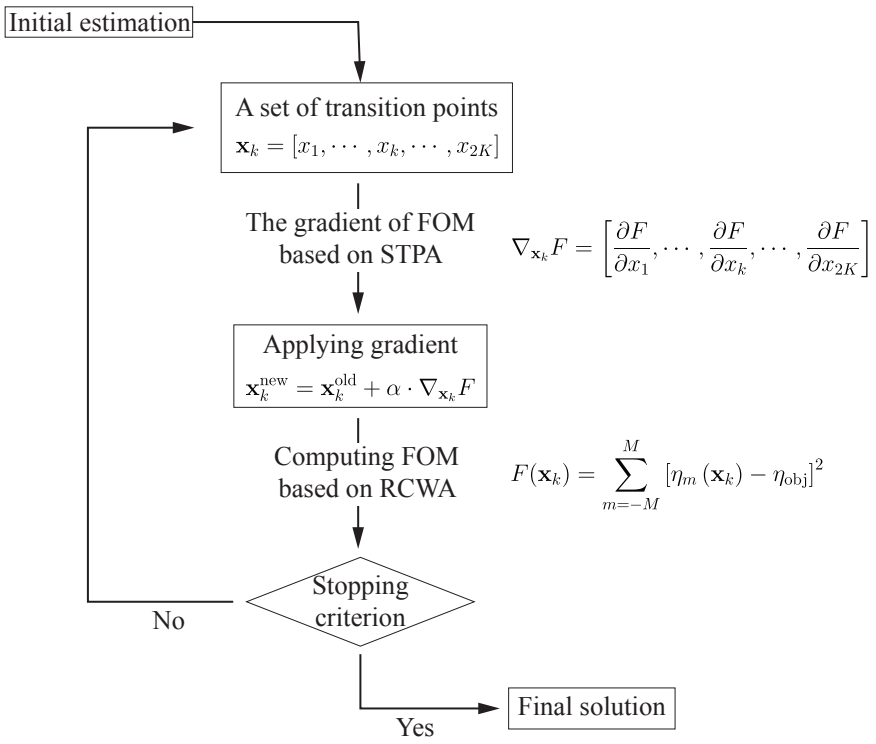


Figure 3.2 – Flowchart for optimization based on STPA

## 3.3 Optimization results : one dimensional (1D) diffractive fan-out elements

Using the proposed optimization approaches, we can design various multi-spot array generators. In general, a diffractive beam splitter creating a larger number of spots requires a more complex structure, i.e., gratings with many features. To verify our method is valid in high dimensional optimization problems, we show the optimization results of fan-out grating generating many spots.

### 3.3.1 Initial design and parameters

With the gradient-based optimization, the elements are optimized within local parametric space to produce the final solution,i.e., local optima. The setting of the initial design thus affects the optimization results. the 1D fan-out grating designed by IFTA is no more valid in wide angle fan-out gratings. Nonetheless, it may be a good candidate for the starting point for the optimization method. Therefore, we prepared surface profiles of 1D fan-out grating designed by IFTA for the initial design of this optimization method.

In binary grating, the depth of the features is normally selected $d = \lambda(n_2 - n_1)/2$ obtaining a $\pi$ phase shift between binary levels. When the grating period is shrunk to generate a wide angle diffraction pattern, we need to modify the depth to adjust the 0-th order, which is often most sensitive to change, in such a manner that the 0-th order can be brought within the range between maximum and minimum diffraction efficiency. If it is not possible, in this case, one can adjust the fill factor or change the polarity of the grating, i.e., exchange the grooves with the ridges. Because the polarity typically has an effect on the diffraction pattern in the non-paraxial domain. In Fig. 3.3, the diffraction efficiency of zeroth order is varied by the depth of features. The black lines indicate maximum and minimum of diffraction efficiency excluding 0-th order,i.e., in off-axis, and the black dashed line is the average of all diffraction efficiency. We adjust the depth in the initial design before running the optimization. Thus, we don't include the depth value to design parameters which are updated during the optimization process.

We select fused silica ($SiO_2$) as material. The refractive index of $SiO_2$ is assumed as $n_2 = 1.46$. Transverse electric (TE)-polarized (i.e., E-field component along the y-axis) or Transverse magnetic (TM)-polarized monochromatic light with a wavelength of $\lambda = 633\,\text{nm}$ is an incident plane wave from the substrate side with normal incidence angle. We optimize 3 different kinds of beam splitters with the depth of the features $d = 692\,\text{nm}$. The target grating periods and maximal diffraction angles are shown in Table 3.1. The maximal diffraction angle $\theta_{\max}$ is illuminated in Fig. 3.4(a), for example, the maximal diffraction angle of $1:117$ diffractive beam splitter are $10.58°$ at $58^{\text{th}}$ order from $0^{\text{th}}$ order. The selected diffraction angles are already beyond the paraxial domain, the designs created by TEA-based IFTA are no more valid. The Fig. 3.4(b) presents the performance of one of these fan-out elements as a function of

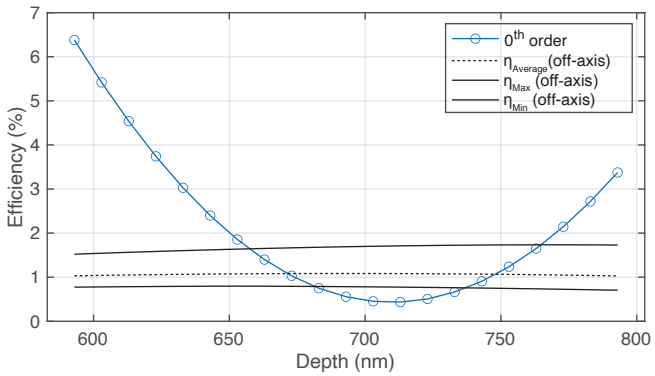


Figure 3.3 – Diffraction efficiency of zeroth order as a function of depth of a 1 : 77 beam splitter

diffraction angle. The dashed line indicate the performance predicted by TEA, which is good estimation in the paraxial domain, i.e., in small diffraction angle. Obviously, the performance of this initial fan-out element is very unsatisfactory with respect to uniformity even when the maximum diffraction angle is over 7°.

Table 3.1 – The specification of the target 1D fan-out elements

| Description | Grating period (μm) | $\theta_{max}$ (°) | Target diffraction orders($^{th}$) |
|---|---|---|---|
| 1 : 77 beam splitter | 100 | 13.92 | -38:38 |
| 1 : 117 beam splitter | 200 | 10.58 | -58:58 |
| 1 : 157 beam splitter | 200 | 14.29 | -78:78 |
| 1 : 197 beam splitter | 400 | 8.92 | -98:98 |

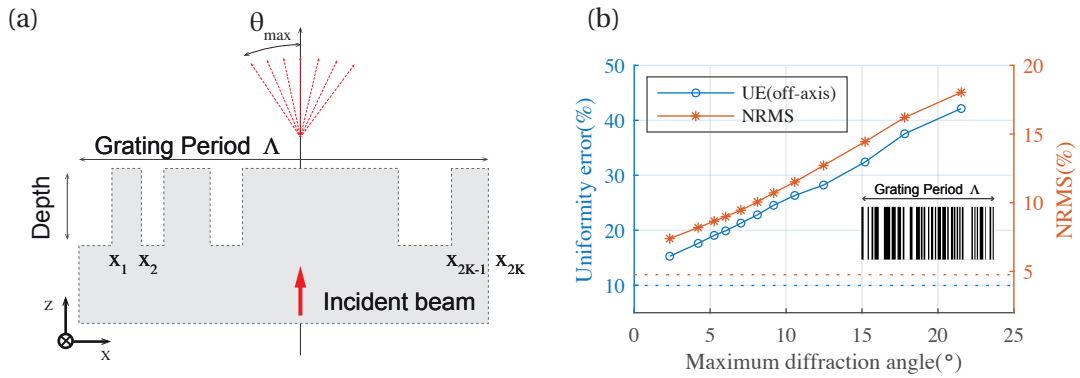


Figure 3.4 – (a) The surface profile of a grating structure in a single period. (b) Uniformity of 1-to-117 diffractive beam splitter designed by TEA-based IFTA as a function of maximum diffraction angle when the grating period Λ decreases. The uniformity error and NRMS calculated using Eq. Eq. (3.16) and Eq. (3.17). The dashed lines indicate the uniformity values calculated based on TEA. The insets show the layout of the single unit cell with a total of 60 transition points.

### 3.3.2 Objective function and evaluation

To obtain the 1D fan-out grating creating uniform diffraction pattern, we use the FOM in Eq. (3.10): $F = \sum_{m=-M}^{M} \left[\eta_m - \eta_{\text{obj}}\right]^2$. By applying Eqs. (2.61) to (2.63), we use two different metrics which are uniformity error (UE) and normalized root-mean-square error (NRMS) $\sigma$ to evaluate the various 1D fan-out elements:

$$UE = \frac{\eta_{\max} - \eta_{\min}}{\eta_{\max} + \eta_{\min}} \tag{3.16}$$

$$\sigma = \sqrt{\frac{1}{2M+1} \sum_{m-M}^{M} \left(\frac{\eta_m - \eta_{\text{obj}}}{\eta_{\text{obj}}}\right)^2} \tag{3.17}$$

where $\eta_{\max}$ and $\eta_{\min}$ represent the maximal and minimum diffraction intensity and $\eta_m$ is diffraction efficiency in orders from $-M$ to $M$ and $\eta_{\text{obj}}$ is target diffraction efficiency and $2M+1$ is the total number of diffraction orders. Lower values of both UE and NRMS indicate less residual variance so that our objective is to minimize UE and NRMS of a 1D diffractive beam splitter design given uniform diffraction efficiency distribution. The UE is the metrics intuitively evaluate the uniformity of diffraction distribution. Sometimes, these metrics fail to measure uniformity. For instance, in case, all efficiencies are identical except in one order (normally, in zeroth order) with the highest or lowest efficiency, UE indicates very poor value. Thus, we use the NRMS to discover the information which is not able to be measured by UE. In addition, the NRMS value is directly related to the FOM.

### 3.3.3 Optimized performances

We apply our optimization tool to create various wide angle diffractive beam splitters mentioned in Table 3.1. To generate these diffractive beam splitters, we use our FOM as in Eq. 2.64 with the uniform intensity distribution of target efficiency $\eta_{\text{obj}}$ and find the local optima using the L-BFGS algorithm with the gradient calculated based on STPA. And we prepare 82 different initial designs in total with 4 different kinds of fan-out gratings designed by TEA-based IFTA.

To verify the validity of the optimization tool based on STPA, we plot in Fig. 3.5 distribution of the final fan-out elements performance, i.e., the uniformity of diffraction pattern, with two metrics: UE and NRMS. In Fig. 3.5, the black dash line indicates the points have an identical value of initial and final elements. In other words, a point located below the dashed line means that there is an improvement in the uniformity of the diffraction distribution after the optimization process. The diffraction efficiencies of initial and final elements are simulated by RCWA for accurate evaluation. We can observe that most cases are significantly improved their uniformity of diffraction pattern through the optimization process. We note that upon optimizing an ensemble of different initial geometries, the final elements from the initial cases with bad performances often exhibit still low performances. As such, the initial

condition affects the optimization results due to gradient-based optimization. Thus, multiple optimization attempts are required to identify devices with exceptional efficiencies.

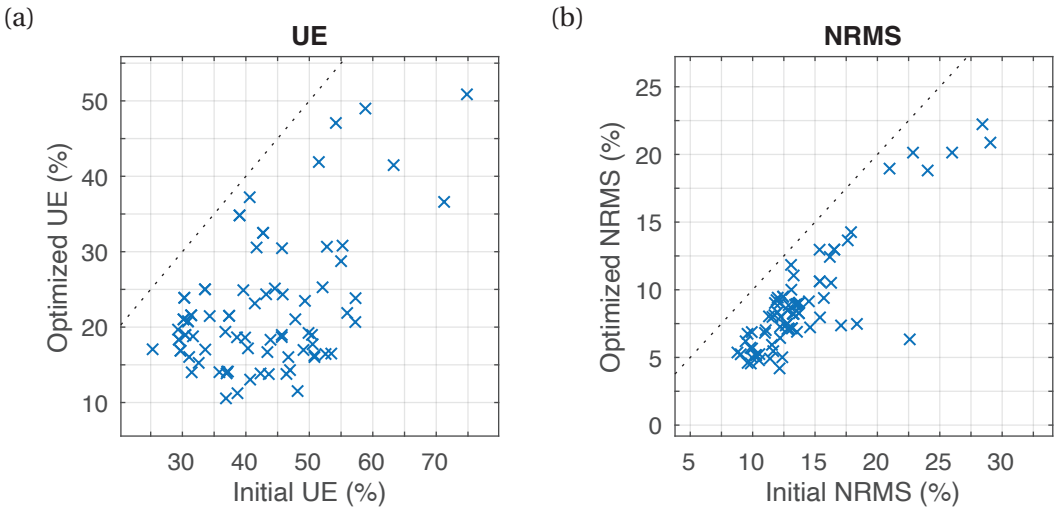


Figure 3.5 – Realization achieved using optimization based on STPA from initial TEA-based IFTA designs of 1D fan-out elements (82 in total) with different metrics: (a) UE and (b) NRMS.

To observe the changes of the FOM and transition positions during the optimization, we represent the details of the optimization process about a $1:117$ diffractive beam splitter in Fig. 3.6. The merit function as a function of the optimization iterations is shown in Fig. 3.6(a). The FOM converged well and the algorithm found the optimum point after 190 iterations. The initial surface profile in a single grating period is illustrated in Fig. 3.6(b). Through the optimization, the change of all transition positions of the structure is plotted in Fig. 3.6(c). The positions of initial transition points are indicated in the black dash line. We thus observe the total number of transitions is 66 and the average change of transition points is around 300 nm after optimization. Finally, the simulated diffraction efficiency distributions of DOEs after optimization is shown in Fig. 3.6(d). We calculated the total diffraction efficiency, UE, and NRMS of optimized diffractive beam splitters using RCWA. The total diffraction efficiency of 117 spots of optimized DOE is 77.35 % and UE from 38.68 % to 10.79 % and NRMS from 12.16 % to 4.18 %, through gradient-based optimization using STPA. The surface profile of optimized design which have critical dimension(CD) (i.e., minimum feature size) is 700 nm and fill factor is 51.16 % is represent in Fig. 3.6(d) inset.

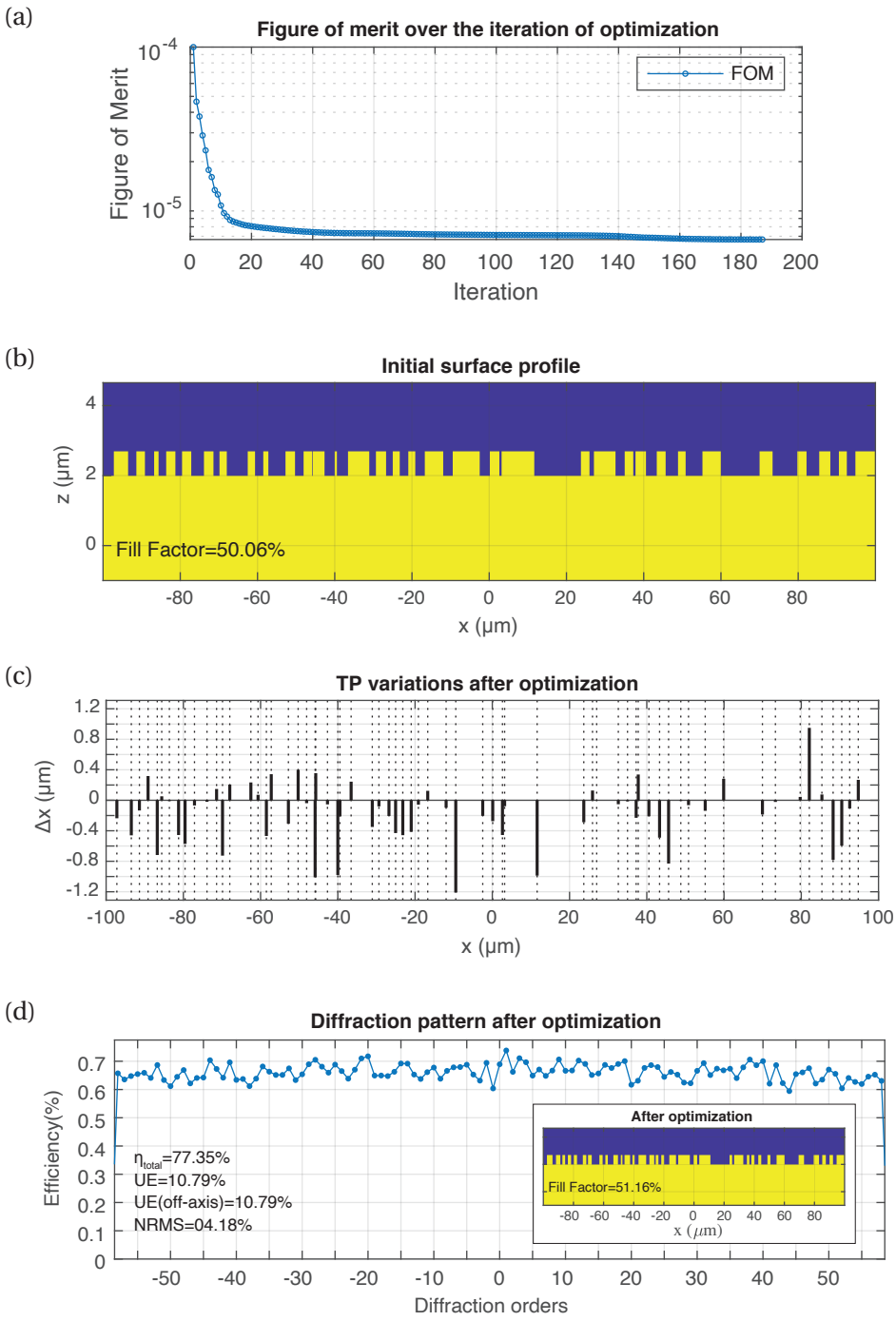


Figure 3.6 – Theoretical analysis of 1 : 117 diffractive beam splitters. (a) the plot of the FOM over the course of the optimization process. (b) The surface profile of the initial element. (c) The variation of transition positions after optimization. The dash lines indicate the transition positions in the single grating period. (d) the calculated efficiency of diffractive beam splitter after optimization. The surface profile of the final element in the inset of (d).

### 3.3.4 Comparison with the gradient from RCWA

Let us compare the gradient of FOM based on the STPA with the numerically calculated gradient based on RCWA. The surface profile of the $1:77$ fan-out grating before optimization is illustrated in Fig. 3.7(a). The numerical derivative is shown in Fig. 3.7(c), which is obtained by computing the FOM after varying slightly each transition point. Hence, to obtain this numerical gradient, the number of transition points, and one more $2K+1$ RCWA calculation is required. By comparing Fig. 3.7(b) and Fig. 3.7(c), both gradients have the same order of magnitude and the same features. In Fig. 3.7(d), the difference between derivatives from STPA and the numerical derivatives from RCWA is calculated. Note that the scale of $y$-axis is 10 times smaller than Fig. 3.7(b) and (c) so that we observe the estimation of gradient from STPA is valid.

Furthermore, we apply gradient-based optimization based on numerical derivatives computed RCWA to optimize the fan-out gratings in order to compare with the optimization tool based on STPA. The uniformity of beam arrays created by elements designed from IFTA based on TEA, followed by optimization, are plotted in Fig. 3.8 with two metrics. We plot together with the uniformity of final design after gradient-based optimization based on RCWA, in this case, the gradient calculated numerically. Therefore, normally around 60 RCWA simulation are required in an iteration during the optimization process. We compared the optimized results by gradient-based on STPA and RCWA. For an accurate comparison, The diffraction efficiencies of final designs are calculated by RCWA. In most cases, the uniformity of these final elements is significantly improved and the uniformity of final design optimized based on STPA are as good as those of optimized based on RCWA. However, the performance of optimization based on STPA is much better than based on RCWA in term of computational effort.

The simulation and optimization steps were written using MATLAB scripts, and the optimization process took less than 20 s using gradient-based optimization by STPA, while taking over 6 h using the optimization with numerical gradient based on RCWA on a machine with 3.60 GHz clock rate and 32 GB RAM. During the optimization, the diffraction pattern for calculating UE and NRMS was evaluated with RCWA solver RETICOLO [138].

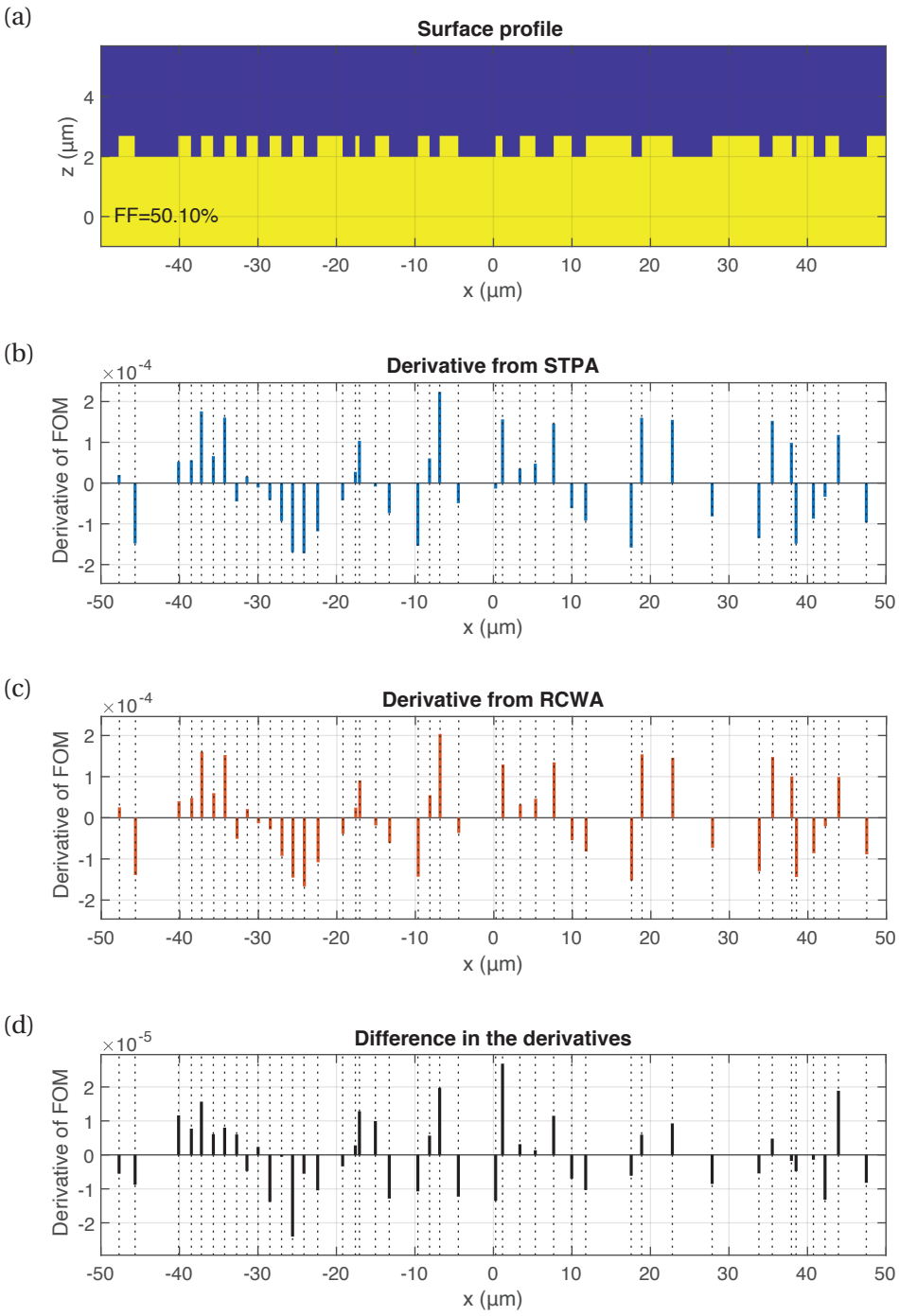


Figure 3.7 – Comparison with the gradient of the FOM with respect to the transition points obtained from STPA and RCWA. The dash lines indicate design variables, i.e., the positions of transition points. (a) The surface profile of 1 : 77 beam splitter before optimization. (b) The derivative of FOM with respect to the positions of transition points. (c) Numerical derivate of the FOM computed by RCWA (d) Difference between (b)STPA and (c)RCWA.

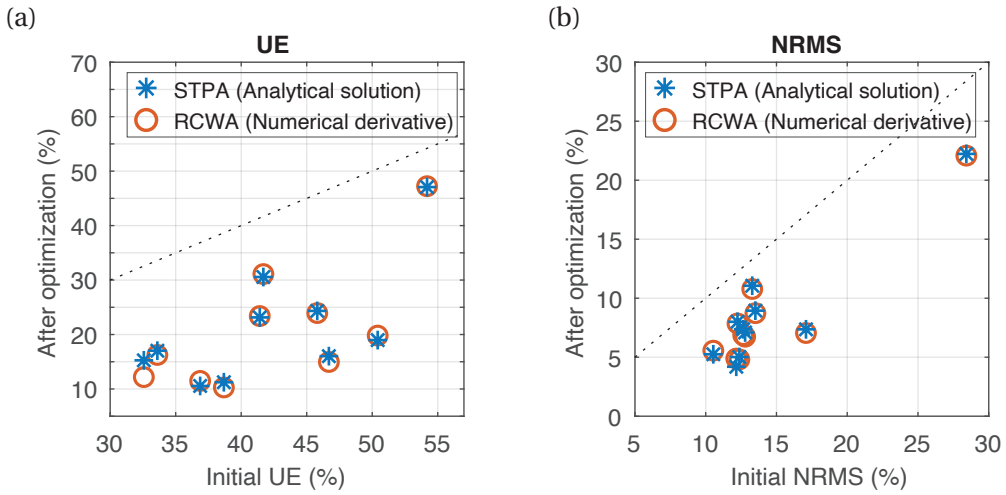


Figure 3.8 – The uniformity of final elements (10 in total) obtained using gradient-based optimization by RCWA and STPA from initial TEA-based IFTA designs with different metrics: (a) UE and (c) NRMS. The gradient-based on RCWA was numerically calculated. The equal uniformity values of initial and optimized elements are indicated by the black dash line.

### 3.3.5 Experimental results

The diffractive beam splitters were fabricated by direct laser writing to obtain $SiO_2$ binary surface relief structures. The elements are optically characterized using a TE-polarized 636 nm wavelength beam from a diode laser. We detect the diffracted light beams using a mobile single-pixel detector with a high dynamic range. In Fig. 3.9, a detector with a pinhole aperture is mounted on a translation stage under computer control. By scanning the detector to the center of each of the spots, it is possible to measure the power contained in each of the spots, i.e. diffraction orders in the output array. The size of detector is enough big to cover the beam spot size. When measuring spots in higher order, the shadow effect may prevent the light from reaching the detector due to the large angle. In preparation for this situation, a system was also established to allow the laser source and sample to rotate on behalf of the detector.

To focus on both the simulation and experiment to facilitate a quantitative comparison, we applied loss caused by Fresnel reflection from the interface between air and $SiO_2$ substrate to simulate the overall efficiency of DOEs. The comparison between theoretical and experimental diffraction efficiencies are presented in Fig. 3.10. We represent the total diffraction efficiency, UE, and RMSE of simulated and measured one in Table 3.2. The experimental data show that the DOEs operate with high-performance. The UE and NRMS of beam splitters are 21.42 % and 8.07 %, respectively. For an accurate comparison between theoretical and measured results, we analyze the correlation of these data using mean absolute percentage deviation (MAPD) as a ratio defined by the formula:

$$\mathrm{MAPD} = \frac{1}{M}\sum\left|\frac{\eta_m^S - \eta_m^E}{\eta_m^S}\right| \tag{3.18}$$

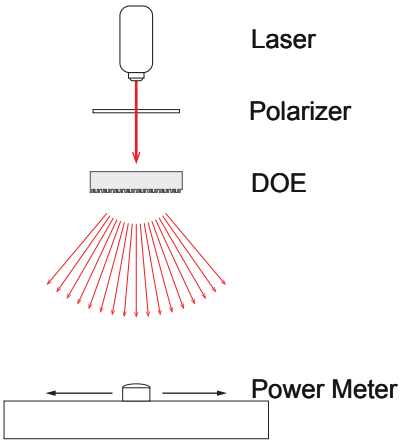


Figure 3.9 – Schematic of equipment used for diffractive array measurements

where $\eta_m^S$,$\eta_m^E$ are simulated and experimental efficiency in $(m)^{\text{th}}$ diffraction orders and $M$ is the total number of diffraction orders. The MAPD of 1-to-117 beam splitters are calculated to the 8.15 %, which shows excellent reproducibility of the simulated results in a quantitative manner. The only noticeable deviation in the measurement is a small mismatch of diffraction efficiency in a few orders due to minor fabrication errors. In general the diffraction efficiency in orders often strongly depends on the errors in fabrication processes, e.g., etching depth, feature width, slope steepness, and feature rounding. Nevertheless, the fabricated samples are based on optimized design overall display experimental performances which are better than the theoretical performances of initial designs before optimization.

Table 3.2 – Comparsion with the simulated and experimental properties of the 1 : 117 beam splitters. The simulated efficiency take into account the loss from Fresnel reflection in the air-$SiO_2$ substrate interface.

| | Simulated | Measured |
|---|---|---|
| Total efficiency (%) | 74.56 | 74.65 |
| UE (%) | 11.74 | 21.42 |
| NRMS (%) | 04.45 | 08.07 |

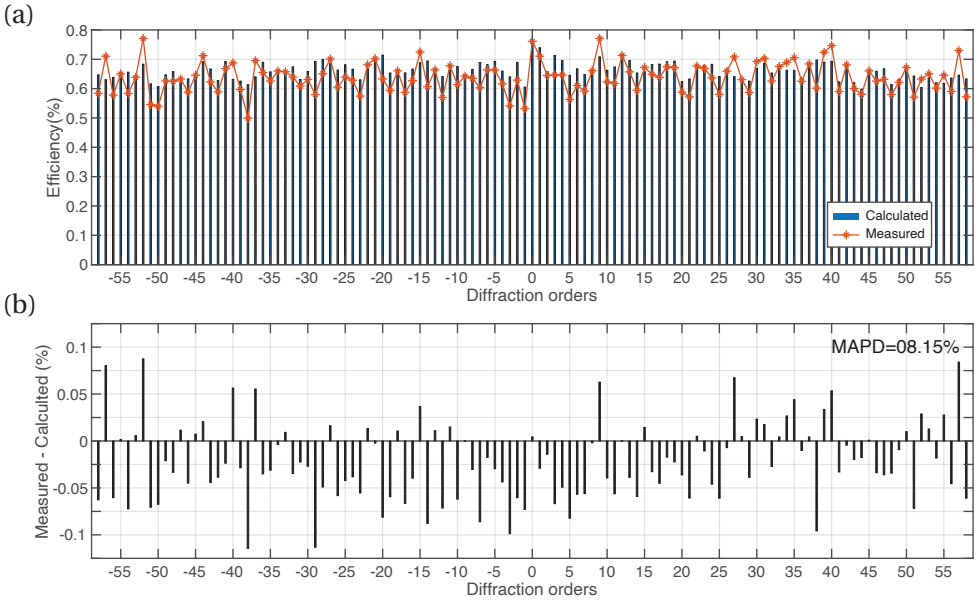


Figure 3.10 – Experimental characterization of 1 : 117 diffractive beam splitter. (a) experimental data (orange star) from profile optimized base on STPA and the simulated data(blue bar). (b) difference between experimental and simulated data in orders.

## 3.4 Discussion of optimization based on STPA

Let us discuss the features of this optimization based on STPA. The derivatives of FOM is calculated based on the STPA so that the accuracy and validity are also following those of STPA. Hence we investigate the conditions for the perturbation method to be established.

Here we use the transition points as a design parameter. We can easily simulate the fabrication errors such as under- or over- etch by changing feature width. To create a robust design toward the fabrication errors, we may include the effect of dilated and eroded features on the gradient.

### 3.4.1 The feature size and accuracy of optimization based on STPA

The performance of this optimization tool is limited by the accuracy of the STPA. Due to the truncation length of perturbation in step transition, the perturbation method becomes inaccurate when the features are smaller than one optical wavelength. Thus, the derivatives based on STPA also get inaccurate if the wavelength scale features are dominant in the structure.

To investigate the validity of gradient from STPA in grating with small features, we compare the degree of improvement between the optimization based on STPA and optimization based on numerical derivatives calculated by RCWA. we apply to optimize the 1 : 37 beam splitter with 25 µm grating period. It have critical dimension (CD) is 315 nm and have several wavelength-scale features. In Fig. 3.11, we observe that there is improvement through optimization using STPA, but the performance of the final design is worse than that of using numerical

derivatives from RCWA. The variation of transition positions after optimization using STPA and numerical derivative based on RCWA from the same initial design is shown in Fig. 3.11(a) and (b), respectively. The dash lines indicate the position of transition points in the initial design. The calculated efficiency of diffractive beam splitter after optimization using STPA and RCWA is represented in Fig. 3.11(c) and (d). The diffraction efficiency is simulated by RCWA with enough Fourier modes for accurate comparison. The final 1 : 37 beam splitter optimized using STPA show the 28.11 % of UE and 18.29 % of NRMS, while the final one optimized using numerical derivatives show the 13.39 % of UE and 8.55 % of NRMS. These values are presented in Table 3.3.

We may thus conclude that at least for the diffractive elements with most of the feature is larger than the wavelength, the optimization based on STPA gives reliable results with low computation effort. But if we create a even wider angle fan-out elements, i.e., the grating become shrunk, the optimization based on STPA may get degraded or doe not work anymore.

Table 3.3 – The uniformity of final 1 : 37 beam splitter obtained using gradient-based optimization by RCWA and STPA.

| | Initial | Optimized | |
|---|---|---|---|
| | | using STPA | using RCWA |
| GP (µm) | | 25 | |
| $\theta_{max}$ (°) | | 27 | |
| CD (nm) | 315 | 260 | 390 |
| $\eta_{total}$ (%) | 80.71 | 80.71 | 80.73 |
| UE (%) | 34.58 | 28.11 | 18.29 |
| NRMS (%) | 18.09 | 13.39 | 08.55 |

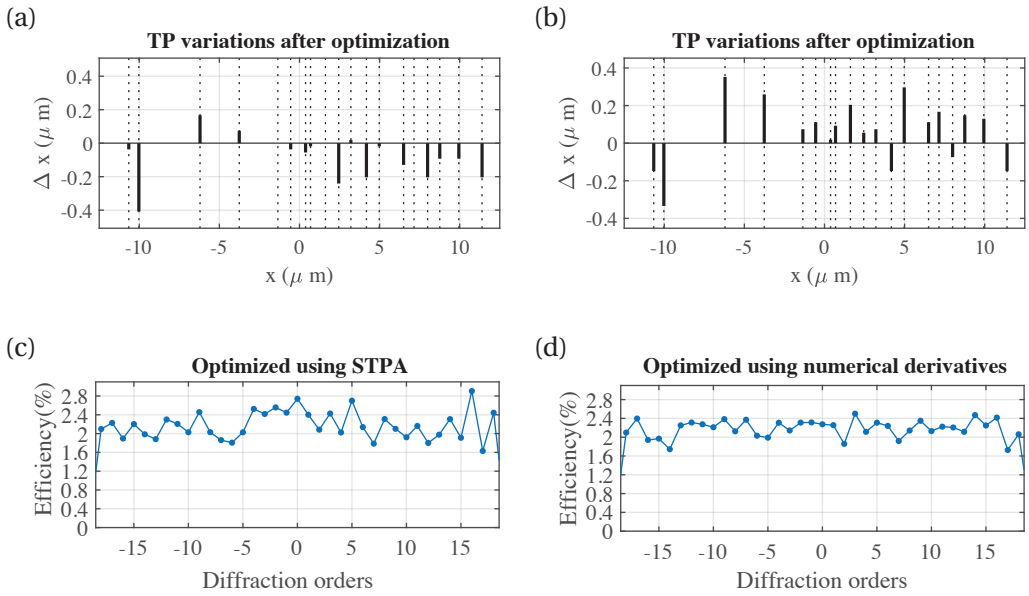


Figure 3.11 – The variation of transition positions after optimization using (a) STPA and (b) numerical derivative based on RCWA. The dash lines indicate the transition positions in initial design. The calculated efficiency of diffractive beam splitter after optimization using (c) STPA and (d) RCWA.

### 3.4.2 Fabrication errors

In general, the spot diffraction efficiency strongly depends on the fabrication errors. The fabrication errors are often inevitable during the process. To investigate the effect of such fabrication errors on the diffraction pattern, we simulated an under- or over-etched effect on the width of features simply by shifting transition points, as shown in Fig. 3.12(a). Here, we consider the under- and over-etched effect in varying the width of features, not the depths. The variation in the etch width is $\Delta x_k$ in which under-etch $+\Delta x_k$ and over-etch $-\Delta x_k$ effect produces the dilated and eroded features in the structure. Thus, the dilated, intermediate, and eroded designs, which mimic under-, normal-, and over-etching in the manufacturing process. For instance, the etch width is $\Delta x_k = +20nm$ so that the width of features are increased as 40 nm and fill factor also is increased.

The simulated results of an optimized 1 : 117 fan-out element with 100 µm grating period with varying the etch width are represented in Fig. 3.12(b), (c), and (d). Through this analysis, we observe how sensitive this beam splitter is to fabrication errors. The UE and NRMS are dramatically degraded when the design is dilated or eroded. We may create more robust design from fabrication error using combined gradient of FOM with respect to design variables from dilated, intermediate, and eroded designs.

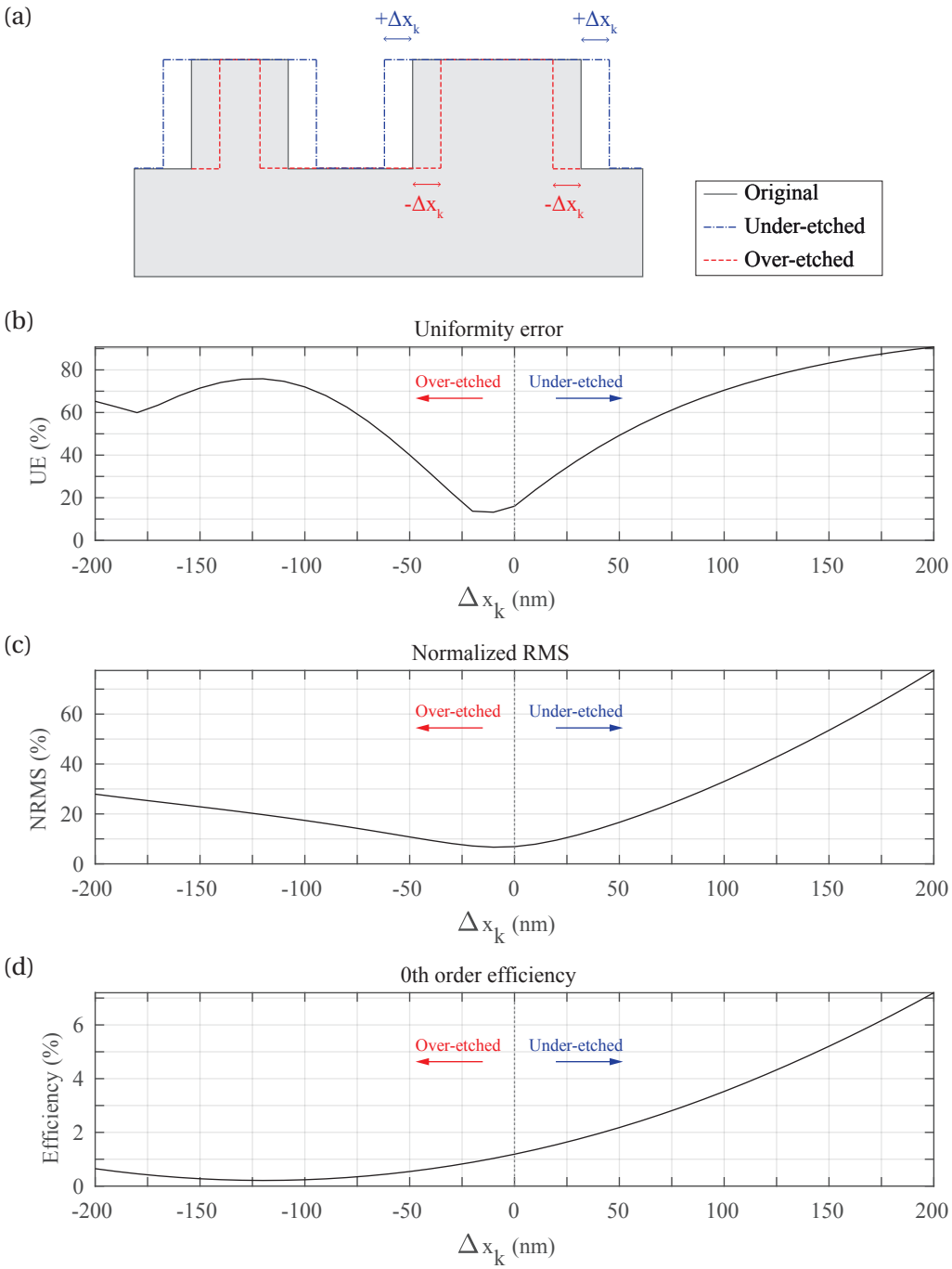


Figure 3.12 – (a) Schematic of the effect of under- or over- etching to the surface profile and the width of features. Simulated results of a 1 : 77 beam splitter with varing $\Delta x_k$ : (b) UE, (c) NRMS, and (d)Diffraction efficiency in 0th order

## 3.5 Summary

In summary, we utilized the STPA in optimizing the optical elements, which is able to create wide angle diffractive optical elements at a very low computational cost. We explored properties of the optimization method, such as efficient computation for the gradient of the target function with respect to transition positions with Fourier-domain local field perturbation. As a case study, we applied gradient-based optimization with STPA to 1-117 beam splitter with a non-paraxial diffraction angle, i.e., maximal diffraction angle is 11° from the center, respectively. The optimized beam splitters show considerable improvement of uniformity while maintaining the initial diffraction efficiency. The experimental results obtained by the illumination of the fabricated optical elements using a laser of 635 nm wavelength with a normal incidence have been compared with the numerical results. Numerical simulation and experimental results were found to be in good agreement and our optimization method can be considered proven to be an effective design tool for wide angle diffractive beam splitters.

However, this method is not suitable to optimize the gratings having a lot of wavelength-scale features. As the design parameters are the set of transition points, we only change the size of the features but we cannot generate or eliminate the features during the optimization process. Sometimes, the improvements through the optimization thus are canceled out due to the fabrication errors. Also, the definition of transition points is difficult to extend to the two-dimensional fan-out grating. Therefore, we introduce the optimization with the adjoint method based on RCWA in the next chapter.

# 4 Optimization based on Adjoint State Method

DOEs with a large diffraction angle require feature sizes down to sub-wavelength dimensions, which require a rigorous electromagnetic computational model for calculation. However, the computational optimization of these diffractive elements is often limited by a large number of design parameters, making parametric optimization practically impossible due to large computation times. The adjoint method allows calculating the gradient of the target function with respect to all design variables with only two electromagnetic simulations, thus enabling gradient-based optimization.

## 4.1 Adjoint state method

We give a brief introduction to the mathematics behind the adjoint method before applying to our specific cases. We often wish to compute some function $f(\boldsymbol{x}, \mathbf{p})$ based on the solution $\boldsymbol{x}$ the design parameters $\mathbf{p}$ and , which are given the solution $\boldsymbol{x}$ of partial differential equation or some other set of $M$ equations parameterized by $N$ variables $\mathbf{p}$. However, we want to know more than just the value of $f$, especially we also want to know its gradient $\nabla_{\mathbf{p}} f$ for inverse design process. Adjoint state methods give an efficient way to evaluate $\nabla_{\mathbf{p}} f$ with a cost independent of the number of parameters $N$ and usually comparable to the cost of solving for $\boldsymbol{x}$ once.

### 4.1.1 Mathematical introduction

Let us suppose the column-vector $\boldsymbol{x}$ solves the $M \times M$ linear system of equation $A\boldsymbol{x} = \mathbf{b}$ where $A$ and $\mathbf{b}$ depend on a set of parameters describing the system, $\mathbf{p}$. The gradient can be expressed by $\nabla_p F = \frac{\partial f}{\partial \mathbf{p}} + \frac{\partial f}{\partial \boldsymbol{x}} \frac{\partial \boldsymbol{x}}{\partial \mathbf{p}}$ where partial derivatives $\frac{\partial f}{\partial \boldsymbol{x}}$ is a row vector, $\frac{\partial \boldsymbol{x}}{\partial \mathbf{p}}$ is an $M \times N$ matrix. Since $f$ is a given function, $\frac{\partial f}{\partial \boldsymbol{p}}$ and $\frac{\partial f}{\partial \mathbf{p}}$ are often easy to compute. On the other hand, computing $\frac{\partial \boldsymbol{x}}{\partial \mathbf{p}}$ is demanding: evaluating it directly by differentiating $A\boldsymbol{x} = \mathbf{b}$ by parameters $\mathbf{p}$ gives $\frac{\partial \boldsymbol{x}}{\partial \mathbf{p}} = A^{-1}(\frac{\partial \mathbf{b}}{\partial \mathbf{p}} - \frac{\partial A}{\partial \mathbf{p}} \boldsymbol{x})$. We multiply a $M \times M$ by a $M \times N$ matrix, which costs $O(M^2 N)$ works, or equivalently we have multiplications of $A^{-1}$ by N times. However, this can be ameliorated

simply by parenthesizing in a different way as following

$$\frac{\partial f}{\partial \boldsymbol{x}}\frac{\partial \boldsymbol{x}}{\partial \mathbf{p}} = \frac{\partial f}{\partial \boldsymbol{x}}\left[A^{-1}\left(\frac{\partial \mathbf{b}}{\partial \mathbf{p}} - \frac{\partial A}{\partial \mathbf{p}}\boldsymbol{x}\right)\right] = \left[\frac{\partial f}{\partial \boldsymbol{x}}A^{-1}\right]\left(\frac{\partial \mathbf{b}}{\partial \mathbf{p}} - \frac{\partial A}{\partial \mathbf{p}}\boldsymbol{x}\right) \tag{4.1}$$

In the last expression of Eq. (4.1), if we first multiply $\boldsymbol{x}_{\text{adj}}^T = \frac{\partial f}{\partial \boldsymbol{x}}A^{-1}$ that corresponds to only a single solution of an adjoint equation

$$A^T\boldsymbol{x}_{\text{adj}} = \left(\frac{\partial f}{\partial \boldsymbol{x}}\right)^T. \tag{4.2}$$

Then we multiply a single vector $\boldsymbol{x}_{\text{adj}}^T$ by our $M \times N$ matrix for only $O(MP)$ work.

In the case of performing the inverse problem of electromagnetic devices, **A** represents Maxwell's equations in the presence of the device, $\boldsymbol{x}$ are the electromagnetic fields, and **b** is the source driving the system.

### 4.1.2 Adjoint method for diffractive optical elements

In this section, we show the mathematical framework of adjoint method using in our wide-angle DOEs optimizations. The diffraction efficiencies $\eta$ can be obtained by transmitted power flow going to the diffraction order represented by plane wave $\mathbf{E}, \mathbf{H}$ from the Poynting vector expression,

$$\begin{aligned}\eta &= |t|^2 \\ &= \frac{1}{4|\Lambda|^2}\left|\iint_\Lambda \left[\boldsymbol{E}\left(\boldsymbol{r'}\right)\times\boldsymbol{H}_i^*\left(\boldsymbol{r'}\right) + \boldsymbol{E}_i^*\left(\boldsymbol{r'}\right)\times\boldsymbol{H}\left(\boldsymbol{r'}\right)\right]\cdot\mathbf{n}_z\,\mathrm{d}\boldsymbol{r'}\right|^2.\end{aligned} \tag{4.3}$$

where both fields $\boldsymbol{E}, \boldsymbol{H}$ are evaluated at location $\mathbf{r}'$ on the $z = h$ plane above the grating and the overlap integral is performed for a single grating period in Fig. 4.1(a). For the sake of simplicity, we assume the permittivity distribution does not depend on the y-axis. The $k$-vector of $\mathbf{E_i}, \mathbf{H_i}$ is $(k_x, k_y, k_z)$ and transmitted amplitude $t$ is normalized by $\frac{1}{2}\left|\left(\mathbf{E_i}\times\mathbf{H_i^*} + \mathbf{E_i^*}\times\mathbf{H_i}\right)\cdot\mathbf{n_z}\right| = 1$, where $\mathbf{n_z}$ is unit vector along $z$-axis.

To obtain the change of $\eta$ for a small perturbation in permittivity $\Delta\epsilon$ in grating, we use the Green's function. we can calculate electromagnetic field in isotropic medium from given illumination by using time-independant Maxwell's equation:

$$\boldsymbol{\nabla}\times\boldsymbol{E} = ik_0\mu(\boldsymbol{r})\boldsymbol{H} \tag{4.4a}$$

$$\boldsymbol{\nabla}\times\boldsymbol{H} = -ik_0\epsilon(\boldsymbol{r})\boldsymbol{E} \tag{4.4b}$$

where $\mu(\boldsymbol{r})$ and $\epsilon(\boldsymbol{r})$ is permeability and permittivity with location $\boldsymbol{r} = (x, y, z)$. For small perturbation in permeability and permittivity, the variation of elctromagnetic field is the

solution of following equations:

$$\nabla \times (\boldsymbol{E} + \Delta\boldsymbol{E}) = ik_0 \left[\mu(\boldsymbol{r}) + \Delta\mu(\boldsymbol{r})\right](\boldsymbol{H} + \Delta\boldsymbol{H}) \tag{4.5a}$$

$$\nabla \times (\boldsymbol{H} + \Delta\boldsymbol{H}) = -ik_0 \left[\epsilon(\boldsymbol{r}) + \Delta\epsilon(\boldsymbol{r})\right](\boldsymbol{E} + \Delta\boldsymbol{E}). \tag{4.5b}$$

We can simplify Eq. (4.5) by neglecting the $O(\Delta^2)$ terms because we consider the cases of the permettivity and permeability is optimized instead of the boundary between two homogeneous media. Hence the equation becomes:

$$\nabla \times \Delta\boldsymbol{E} = ik_0 \left[\mu(\boldsymbol{r})\Delta\boldsymbol{H} + \Delta\mu(\boldsymbol{r})\boldsymbol{H}\right] \tag{4.6a}$$

$$\nabla \times \Delta\boldsymbol{H} = -ik_0 \left[\epsilon(\boldsymbol{r})\Delta\boldsymbol{E} + \Delta\epsilon(\boldsymbol{r})\boldsymbol{E}\right] \tag{4.6b}$$

which is a valid approximation if the change in the electromagnetic field from $\Delta\mu$ and $\Delta\epsilon$ is sufficiently small. The addition of this tiny perturbation $\Delta\mu$ and $\Delta\epsilon$ at location $\boldsymbol{r}$ can be treated as the dipole with polarization density $\boldsymbol{P}$ and a magnetization density $\boldsymbol{M}$ given by:

$$\boldsymbol{P}(\boldsymbol{r}) = \Delta\epsilon(\boldsymbol{r})\boldsymbol{E}(\boldsymbol{r}) \tag{4.7a}$$

$$\boldsymbol{M}(\boldsymbol{r}) = \Delta\mu(\boldsymbol{r})\boldsymbol{H}(\boldsymbol{r}). \tag{4.7b}$$

By introducing Green's tensors, this dipole produces scattered fields to location $\boldsymbol{r'}$ ,which are described by:

$$\Delta\boldsymbol{E}\left(\boldsymbol{r'}\right) = \hat{\boldsymbol{G}}_{EP}\left(\boldsymbol{r'}, \boldsymbol{r}\right)\boldsymbol{P}(r) + \hat{\boldsymbol{G}}_{EM}\left(\boldsymbol{r'}, \boldsymbol{r}\right)\boldsymbol{M}(r) \tag{4.8a}$$

$$\Delta\boldsymbol{H}\left(\boldsymbol{r'}\right) = \hat{\boldsymbol{G}}_{HP}\left(\boldsymbol{r'}, \boldsymbol{r}\right)\boldsymbol{P}(r) + \hat{\boldsymbol{G}}_{HM}\left(\boldsymbol{r'}, \boldsymbol{r}\right)\boldsymbol{M}(r) \tag{4.8b}$$

where $\boldsymbol{M}(\boldsymbol{r})$ terms can be omitted because $\Delta\mu(\boldsymbol{r}) = 0$ in our material. In addition, the Green's tensors in a reciprocal medium can be expressed by:

$$\hat{\boldsymbol{G}}_{EP}\left(\boldsymbol{r'}, \boldsymbol{r}\right) = \hat{\boldsymbol{G}}_{EP}^{T}\left(\boldsymbol{r}, \boldsymbol{r'}\right) \tag{4.9a}$$

$$\hat{\boldsymbol{G}}_{HP}\left(\boldsymbol{r'}, \boldsymbol{r}\right) = -\hat{\boldsymbol{G}}_{EM}^{T}\left(\boldsymbol{r}, \boldsymbol{r'}\right) \tag{4.9b}$$

The details of these properties are proved in Chapter 7 in Ref.[139].

By applying Eqs. (4.5) and (4.6) to Eq. (4.3), the change of $\eta$ for a small perturbation in permittivity $\Delta\epsilon$ at a location $\boldsymbol{r}$ in the grating layer, i.e., the layer 2 in Fig. 4.1(a), is given by:

$$\Delta\eta = \frac{1}{2|\Lambda|}\,\mathrm{Re}\left\{t^* \iint_{\Lambda}\left[\Delta\boldsymbol{E}\left(\boldsymbol{r'}\right) \times \boldsymbol{H}_i^*\left(\boldsymbol{r'}\right) + \boldsymbol{E}_i^*\left(\boldsymbol{r'}\right) \times \Delta\boldsymbol{H}\left(\boldsymbol{r'}\right)\right] \cdot \mathbf{n_z}\,\mathrm{d}\boldsymbol{r'}\right\} \tag{4.10}$$

Using Eq. (4.7) and Eq. (4.8), the derivative of diffraction efficiency with respect to permittivity is

$$\frac{\partial\eta}{\partial\epsilon(\boldsymbol{r})} = \frac{1}{2|\Lambda|}\,\mathrm{Re}\left\{t^* \iint_{\Lambda}\left[\hat{\boldsymbol{G}}_{EP}(\boldsymbol{r'}, \boldsymbol{r})\boldsymbol{E}(\boldsymbol{r}) \times \boldsymbol{H}_i^*(\boldsymbol{r'}) + \boldsymbol{E}_i^*(\boldsymbol{r'}) \times \hat{\boldsymbol{G}}_{HP}(\boldsymbol{r'}, \boldsymbol{r})\boldsymbol{E}(\boldsymbol{r})\right] \cdot \mathbf{n_z}\,\mathrm{d}\boldsymbol{r'}\right\}. \tag{4.11}$$

Applying the triple product rule of vector identities and reciprocity of Green's tensor in Eq. (4.9), we obtain as following

$$\frac{\partial \eta}{\partial \epsilon(\boldsymbol{r})} = \frac{1}{2|\Lambda|}\mathrm{Re}\left(t^* \iint_{\Lambda} \left\{\hat{\boldsymbol{G}}_{EP}(\boldsymbol{r},\boldsymbol{r}')\left[\boldsymbol{H}_i^*(\boldsymbol{r}')\times \mathbf{n}_z\right] + \hat{\boldsymbol{G}}_{EM}(\boldsymbol{r},\boldsymbol{r}')\left[\boldsymbol{E}_i^*(\boldsymbol{r}')\times \mathbf{n}_z\right]\right\} \mathrm{d}\boldsymbol{r}\cdot \boldsymbol{E}(\boldsymbol{r})\right) \tag{4.12a}$$

$$= \frac{1}{2|\Lambda|}\mathrm{Re}\left\{t^* \boldsymbol{E}_{\mathrm{adj}}(\boldsymbol{r})\cdot \boldsymbol{E}(\boldsymbol{r})\right\}, \tag{4.12b}$$

where the adjoint field $\boldsymbol{E}_{\mathrm{adj}}$ is

$$\iint_{\Lambda} \left\{\hat{\boldsymbol{G}}_{EP}(\boldsymbol{r},\boldsymbol{r}')\left[\boldsymbol{H}_i^*(\boldsymbol{r}')\times \mathbf{n}_z\right] + \hat{\boldsymbol{G}}_{EM}(\boldsymbol{r},\boldsymbol{r}')\left[\boldsymbol{E}_i^*(\boldsymbol{r}')\times \mathbf{n}_z\right]\right\} \mathrm{d}\boldsymbol{r}\,. \tag{4.13}$$

It can be obtained by an solution of Maxwell's equation with illumination condition which is a plane wave generated by the polarization $(\boldsymbol{H}_i^*(\boldsymbol{r}')\times \mathbf{n}_z)$ and magnetization densities $(\boldsymbol{E}_i^*(\boldsymbol{r}')\times \mathbf{n}_z)$ from dipole expression. Thus, the adjoint field $\boldsymbol{E}_{\mathrm{adj}}(r)$ can be obtained by an auxiliary rigorous electromagnetic simulation. The Eq.4.12 shows that one requires the derivative of diffraction efficiency from only two simulations, one direct $\boldsymbol{E}(r)$ and adjoint $\boldsymbol{E}_{\mathrm{adj}}(r)$ to evaluate the derivatives for all pixels in illustrate in Fig. 4.1.

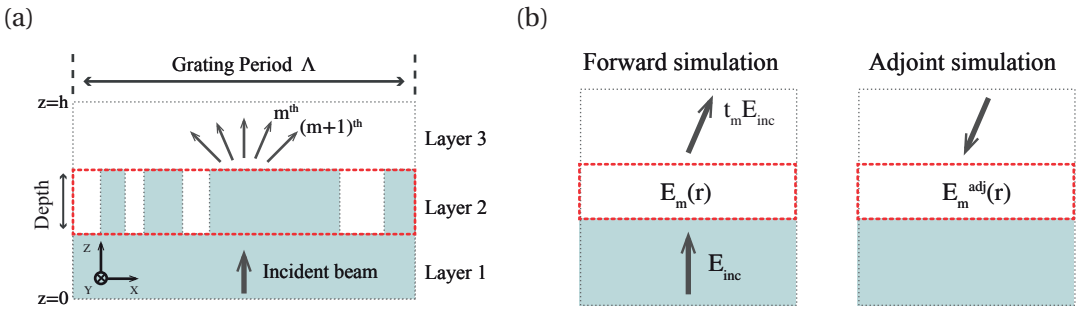


Figure 4.1 – (a) The surface profile of a grating structure in a single period. (b) Schematic of the forward and adjoint simulations in RCWA.

## 4.2 Topology optimization

We employ spatial filtering[140] and projection function[141] during the optimization. We discuss our method for driving the dielectric continuum to discrete values of dielectric material and air and maintaining the fabricable minimum feature size over the iterative process. For the optimization, the starting point is a structure designed IFTA with applying a spatial filter to generate the dielectric continuum. We update a design density $\boldsymbol{\rho}$ which has a value from 0 to 1, rather than updating the permittivity distribution $\boldsymbol{\epsilon}$ directly (see Fig. 4.2(a)). For generating a structure with larger feature sizes, a spatial loss-pass filter can be applied to $\boldsymbol{\rho}$ to create a

filtered density $\tilde{\boldsymbol{\rho}}$ :

$$\tilde{\rho}_i = \frac{\sum_{j\in\mathbb{N}_i} \boldsymbol{W}_{ij}\rho_j}{\sum_{j\in\mathbb{N}_i} \boldsymbol{W}_{ij}} \tag{4.14}$$

where $\mathbb{N}_i$ denotes the design region, and $\boldsymbol{W}_{ij}$ is the weighting matrix, defined for a blurring radius of $R$ as

$$\boldsymbol{W}_{ij} = R - \left|r_i - r_j\right| \tag{4.15}$$

with $\left|r_i - r_j\right|$ being the distance between pixel $i$ and $j$. This defines a spatial filter on $\boldsymbol{\rho}$ with the effect of smoothing out features with a length scale below $R$. The effect of this filter with 300 nm radius of $R$ on a sample design density distribution is illustrated in Fig. 4.2(b). The filtered geometry becomes then a binary pattern using projection function. We define $\bar{\boldsymbol{\rho}}$ as the projected density, which is created from blurred density $\tilde{\boldsymbol{\rho}}$ as

$$\bar{\rho}_i = \frac{\tanh\left(\beta\gamma\right) + \tanh\left(\beta\left[\tilde{\rho}_i - \gamma\right]\right)}{\tanh\left(\beta\gamma\right) + \tanh\left(\beta\left[1-\gamma\right]\right)} \tag{4.16}$$

where a threshold factor $\gamma$ between 0 and 1 which controls the threshold of the projection, typically 0.5, and $\beta$ controls the strength of the projection, bigger value delivers harder binarization. The projected density distribution in Fig. 4.2(c) is recreated from blurred pattern in Fig. 4.2(b) with $\gamma = 0.5$ and $\beta = 300$. We also observe that the combination of circular spatial blurring filter and projection function can remove tiny features. The final relative permittivity distribution from the projected pattern is shown in Fig. 4.2(d). In addition, we can describe an analytical solution of the derivatives $\frac{\partial\boldsymbol{\epsilon}}{\partial\bar{\boldsymbol{\rho}}}$, $\frac{\partial\bar{\boldsymbol{\rho}}}{\partial\tilde{\boldsymbol{\rho}}}$, $\frac{\partial\tilde{\boldsymbol{\rho}}}{\partial\boldsymbol{\rho}}$, these filters [141] can be combined with the derivatives of figure of merit calculated by adjoint method. The obtained gradient was used in optimization based on the limited-memory Broyden-Fletcher-Goldfarb-Shanno (L-BFGS) algorithm[129, 130].

In these filter and projection functions, we can control the strength of the projection so that the binary structure is gradually obtained by updating the strength factor over several iterations during the optimization process. The optimization is performed in an iterative approach and typically $100-200$ iterations are used to achieve convergence. The starting points in gradient optimization are designs from IFTA optimizations with applied spatial filter and projection function. To obtain final design density with binary value, we choose sufficiently large $\beta_{max}$.

The full optimization procedure can be written in Algorithm 1.

**Algorithm 1:** The iterative optimization implementation for wide-angle DOEs

**Input :** the design density $\rho$

**Output :** $\operatorname{argmin}_{\rho} F(\boldsymbol{\eta}_{mn}, \boldsymbol{\rho})$

Initialize the design variable $\boldsymbol{\rho}$
$i \leftarrow 0$ // iteration counter
**while** $\beta \leq \beta_{max}$ **do**
  $i \leftarrow i + 1$
  $\frac{\partial F}{\partial \epsilon} = \frac{\partial F}{\partial \eta} \cdot \frac{\partial \eta}{\partial \epsilon}$ // using adjoint method
  $\frac{\partial \epsilon}{\partial \rho} = \sum \frac{\partial \epsilon}{\partial \bar{\rho}} \cdot \frac{\partial \bar{\rho}}{\partial \tilde{\rho}} \cdot \frac{\partial \tilde{\rho}}{\partial \rho}$ // spatial filter and projection
  $\frac{\mathrm{d}F}{\mathrm{d}vb*\rho} = \frac{\mathrm{d}F}{\mathrm{d}\boldsymbol{\epsilon}} \cdot \frac{\mathrm{d}vb*\epsilon}{\mathrm{d}vb*\rho}$ // calculate the sensitivities
  update $\boldsymbol{\rho}_i$ // by using L-BFGS
  **if** $i \mod 10 = 0$ **then**
    $\beta \leftarrow 2\beta$ // update the projection strength

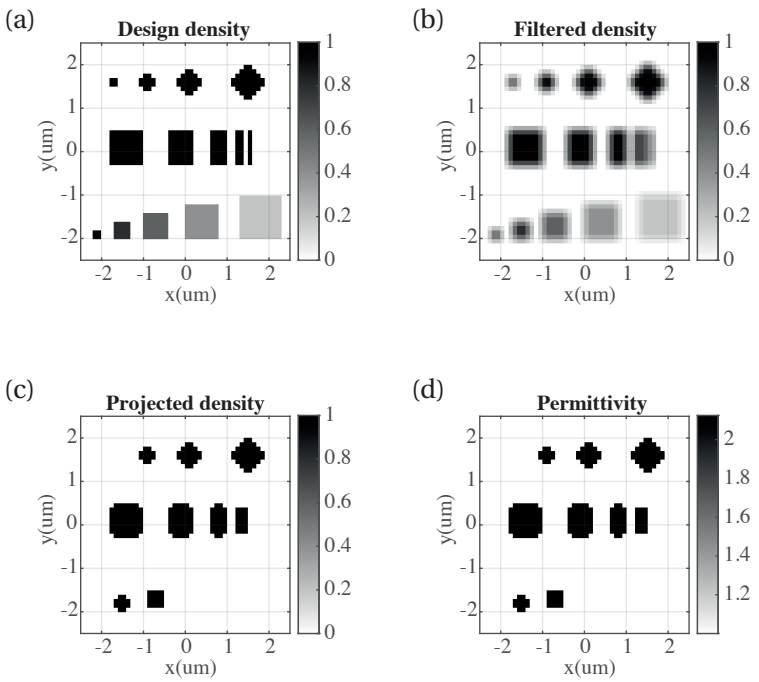


Figure 4.2 – spatial filter and projection of example design density. (a)the initial design density $\boldsymbol{\rho}$ before processing. (b) the density after applying the spatial filter, $\tilde{\boldsymbol{\rho}}$. (c) the density after applying projection, $\bar{\boldsymbol{\rho}}$. (d) the final relative permittivity $\boldsymbol{\epsilon}$.

## 4.3 Inverse design of 1D fan-out gratings

As a case study, we optimize wide angle 1D fan-out grating creating various diffraction pattern, we use thus figure of merit in Eq. (2.64): $F = \sum_{m=-M}^{M} \left[\eta_m - \eta_{\text{obj}}\right]^2$. We optimized wide angle 1D fan-out gratings generating even-numbered spot array with uniform intensity using the proposed optimization tool. Hence, the $\eta_{\text{obj}}$ is high intensity in odd diffraction orders and suppressed intensity in even diffraction orders.

To evaluate DOEs with various diffraction efficiency distribution, we define uniformity error (UE) and normalized root-mean-square error (NRMS) in Eqs. (2.62) and (2.63) : $UE = \frac{\eta_{\max} - \eta_{\min}}{\eta_{\max} + \eta_{\min}}$ and $NRMS = \sqrt{\frac{1}{T}\sum_m \left(\frac{\eta_m - \eta_{\text{obj}}}{\eta_{\text{obj}}}\right)^2}$, where we only consider the high intensity orders, i.e., odd diffraction orders not the suppressed orders. Lower values of both UE and NRMS indicate less residual variance so that our objective is to minimize UE and NRMS of a DOE design given certain diffraction efficiency distribution. We also use the signal-to-noise ratio (SNR) especially for the even-numbered beam splitter as following

$$\text{SNR} = 10\log\frac{\eta_{\text{signal}}}{\eta_{\text{noise}}} = 10\log\frac{\sum_{m=-M}^{M}\eta_{2m}}{\sum_{m=-M}^{M}\eta_{2m+1}}, \tag{4.17}$$

where the $\eta_{\text{signal}}$ is the sum of diffraction efficiencies in target orders and the $\eta_{\text{noise}}$ is the sum of diffraction efficiencies in suppressed orders.

Regarding the grating structure, we select fused silica ($SiO_2$) as material. The refractive index of $SiO_2$ is assumed as $n_2 = 1.45$. Linear polarized monochromatic light with a wavelength of $\lambda = 1064\,\text{nm}$ is an incident plane wave from the substrate side with a normal incidence angle. The target grating periods and maximal diffraction angles are shown in Table 4.1. The maximal diffraction angle $\theta_{\max}$ is around 24° from zeroth order to $15^{\text{th}}$ order when the grating period is $50\,\mu\text{m}$.

Table 4.1 – The specification of the target 1D fan-out element creating even-numbered spot array

| Description | Grating period (μm) | $\theta_{\max}$ (°) | Target diffraction orders($^{\text{th}}$) |
|---|---|---|---|
| 1 : 16 beam splitter | 50 | 24 | -15:15 |

### 4.3.1 Even-numbered spot array illuminator

Here, we design the wide angle beam splitter generating even-numbered spot array using the optimization based on the adjoint method. The even-numbered array contains an even number of spots along one direction, where high intensity orders alternate with suppressed orders. In the paraxial domain, the translational symmetry with $\pi$ phase offset in binary grating produces the even-numbered spot array[142]. We thus express a translational shift

thus relates the second half-period to the first half-period as

$$\Phi(x) = \Phi\left(x - \frac{1}{2}\Lambda\right) + \pi, \qquad \frac{1}{2}\Lambda \le x \le \Lambda \tag{4.18}$$

where $\Lambda$ is the grating period, $\Phi(x)$ phase shift due to the structure at location $x$. An example of translational symmetry in a binary grating is shown in Fig. 4.3 Obviously, this design is not suitable for wide-angle fan-out grating, but we can still use this for the initial starting point for the optimization process.

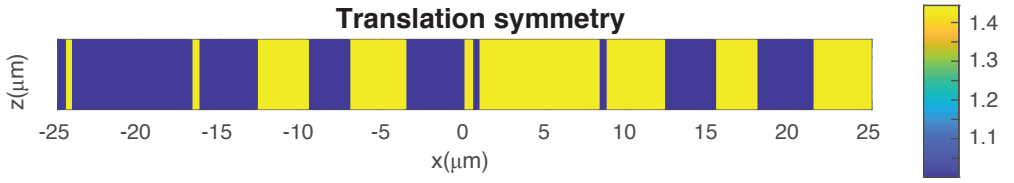


Figure 4.3 – Surface profile one period of a binary grating area with translation symmetry about the period midpoint $x = 0$

### 4.3.2 Optimization results

To evaluate the validity of the optimization tool, we summarize the distribution of the final fan-out elements performance in Fig. 4.4 with three metrics: UE, NRMS, and SNR. In Fig. 4.4, the black dash line indicates the points have an identical value of initial and final elements. In UE and NRMS plot in Fig. 4.4(a) and (b), a point located below the dashed line means that there is an improvement in the uniformity of the diffraction distribution after the optimization process and SNR plot in Fig. 4.4(c), a point located above the dashed line means that there is an improvement in sharpness of spot array pattern. Some elements have high SNR values at the initial, but it is often due to a strong intensity in zeroth order with enormously week intensity in suppressed orders. Hence, the high SNR value does not always guarantee the high-performance even-numbered beam splitter.

We can observe that most cases are significantly improved their uniformity of diffraction pattern through the optimization with the adjoint method. We note that upon optimizing an ensemble of different initial geometries, the final elements from even initial cases with bad performances can be achieved with exceptional performances. As such, the optimization with the adjoint method is more powerful than the optimization tool presented in the previous chapter because there is more chance for improvements by using the refractive index in the pixels as design parameters.

To observe the progress of the FOM over the optimization iterations, the details of the optimization process about a $1:16$ diffractive beam splitter is given in Fig. 4.5. The merit function as a function of the optimization iterations is shown in Fig. 4.5(a). The projection strength factor $\beta$ incrementally increases every 10 or satisfied the criteria for binarization. The update

of this factor is indicated by the black dash line in Fig. 4.5(a). The FOM converged well and the algorithm found the optimum point after 220 iterations in this case. The final design which have critical dimension (CD) (i.e., minimum feature size) is 780 nm and fill factor is 45.25 % is represent in Fig. 3.6(b). Finally, the simulated diffraction efficiency distributions of optimized fan-out element is shown in Fig. 4.5(c).

For an accurate comparison, we calculated the total diffraction efficiency, UE, NRMS, and SNR of initial and optimized even-numbered diffractive beam splitters. In Table 4.1, the optimized DOE has significantly improvements which are the total diffraction efficiency of 16 spots from 75.56 % to 77.44 % and UE from 99.27 % to 4.74 % and NRMS from 90.88 % to 2.63 % and SNR from 14.16 dB to 19.86 dB, through gradient-based optimization using adjoint method.

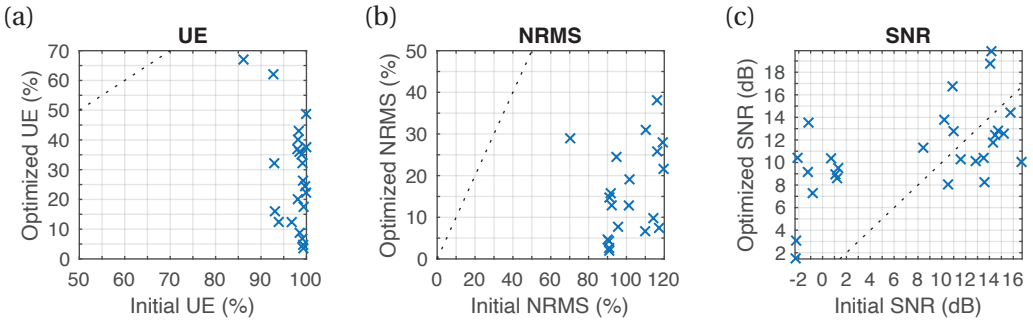


Figure 4.4 – Realization achieved using optimization with adjoint method from initial translation symmetry designs of even-numbered spot array illuminators (27 in total) with different metrics: (a) UE, (b) NRMS, and (c) SNR.

Table 4.2 – Comparison with the initial and optimized properties of the 1 : 16 even-numbered beam splitters.

| | Initial | Optimized |
|---|---|---|
| $\eta_{\text{total}}$(%) | 75.56 | 77.44 |
| UE (%) | 99.27 | 04.74 |
| NRMS (%) | 90.88 | 02.63 |
| SNR(dB) | 14.16 | 19.86 |

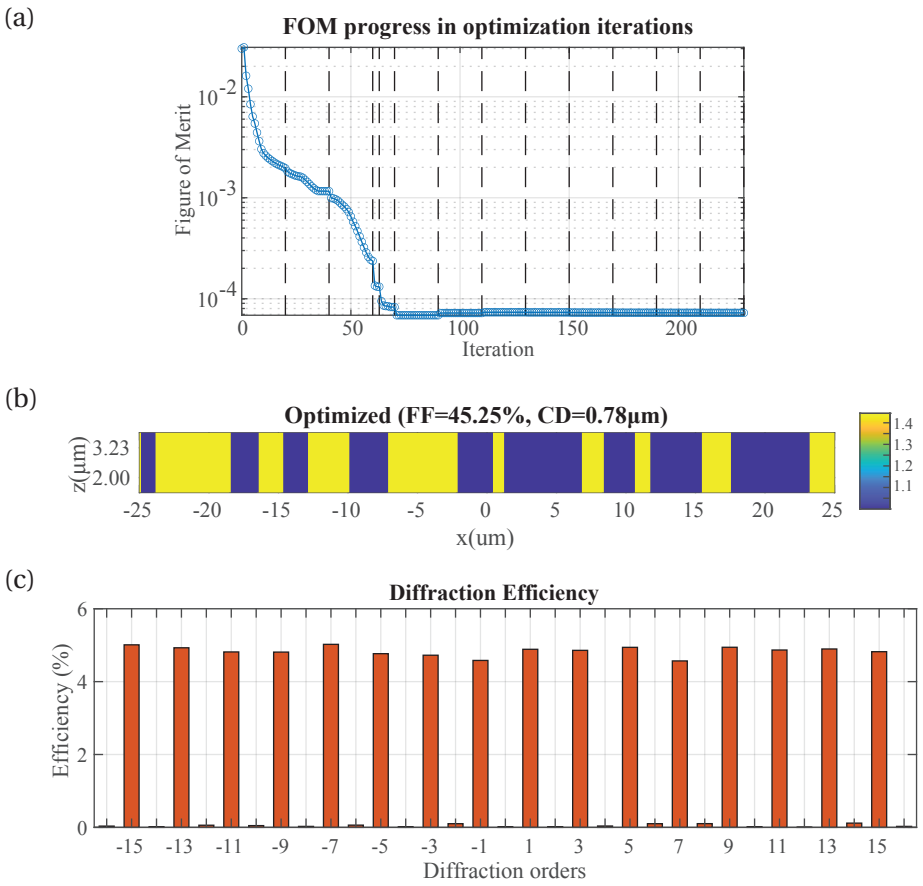


Figure 4.5 – (a) The plot of the figure of merit over the course of the optimization process in 1 : 16 beam splitter. (b) The surface profile of the final element. (d) The calculated efficiency of diffractive beam splitter after optimization.

## 4.4 Inverse design of 2D diffractive beam splitters

To obtain the 2D fan-out grating creating various diffraction pattern, we use figure of merit in Eq. (2.64): $F = \sum_{m=-N}^{N} \sum_{m=-M}^{M} \left[\eta_{mn} - \eta_{\text{obj}}\right]^2$. Two kinds of 2D fan-out gratings were selected for verification of the proposed design approach. The first one is a common multi-spot generator which creates an array of spots with equal intensity distribution, and the other generates a two-dimensional array of spots with the multilevel intensity distribution. To evaluate DOEs with various diffraction efficiency distribution, we define uniformity error (UE) and normalized root-mean-square error (NRMS) in Eqs. (2.62) and (2.63) : $UE = \frac{\eta_{\max} - \eta_{\min}}{\eta_{\max} + \eta_{\min}}$ and $NRMS = \sqrt{\frac{1}{T} \sum_{m,n} \left( \frac{\eta_{mn} - \eta_{\text{obj}}}{\eta_{\text{obj}}} \right)^2}$. We use NRMS because normalizing root-mean-square error facilitates the comparison among various diffraction efficiency distributions with different scales from diverse DOEs. Lower values of both UE and NRMS indicate less residual variance so that our objective is to minimize UE and NRMS of a DOE design given certain diffraction efficiency distribution. Fused silica ($SiO_2$) was selected as a material for DOE. The refractive index of $SiO_2$ is assumed as $n_2 = 1.45$. TE- or TM-polarized monochromatic light with a

wavelength of $\lambda = 940\,\text{nm}$ is an incident wave from the substrate side with a normal incidence angle. The grating period is $5\,\mu\text{m} \times 5\,\mu\text{m}$ and the pixel size is $100\,\text{nm} \times 100\,\text{nm}$. The depth of the grating was selected as $d = 1.18\,\mu\text{m}$. Thus, the maximal diffraction angle of $7 \times 7$ and $7 \times 5$ diffractive beam splitter are about 53° at $(3,3)^{\text{th}}$ order and 43° at $(2,3)^{\text{th}}$ order from $(0,0)^{\text{th}}$ order, respectively. The diffraction angle in vertical and horizotal are shown in the Table 4.3.

Table 4.3 – The diffraction angle of the target 2D fan-out elements

| Description | Grating period (μm) | Diffraction angle (°) | | |
|---|---|---|---|---|
| | | in horizontal | in vertical | in diagonal |
| $5 \times 7$ beam splitter | $5 \times 5$ | 22 | 34 | 43 |
| $7 \times 7$ beam splitter | $5 \times 5$ | 34 | 34 | 53 |

### 4.4.1 Fan-out elements with uniform intensity distribution

To apply the optimization method, we prepared two kinds of two-dimensional fan-out gratings calculated by IFTA for initial designs. One kind is a square multi-spot generators which creates a 7x7 array of spots with equal intensity, the other generates a 5x7 non-square array of spots. To optimization these diffractive beam splitter, we define our figure of merit as Eq. 2.64 with the uniform intensity distribution of target efficiency $\eta_{\text{obj}}$ and find the local optima using L-BFGS with the gradient calculated by the adjoint method. The objective of this design is to create a grating structure that can accurately diffract the incident light into 49 in different directions with equal intensity distribution. Figure 4.6(a) shows the merit function as a function of the optimization iterations of $7 \times 7$ diffractive beam splitters. To minimize the modifications of the adjoint sensitivity, the projection strength factor $\beta$ incrementally increases every 10 iterations for binarization. This function results in immediate effects in the figure of merit, which can be visualized as disconnections on the dash lines. The figure of merit converged well and the algorithm found the optimum point after 80 iterations in this case. The simulated diffraction efficiency distributions of DOEs before and after optimization is shown in Fig 4.6(b) and 4.6(c), respectively. These results are calculated for normally incident TE-polarized light, i.e. the electric field component along the y-axis. In the diffraction pattern, the maximal diffraction angle is about 53° at $(3,3)^{\text{th}}$ order spot from the center. The diffraction efficiency in orders before and after optimization are presented in Table 4.4.

For an accurate evaluation, we calculated the total diffraction efficiency, UE, and NRMS of the initial and optimized diffractive beam splitter. The total diffraction efficiency of 49 spots of initial and optimized $7 \times 7$ spot-array generators are 79.96 %, and 79.71 %, respectively. This optimized element thus has no degradation in total efficiency while there is considerable improvement in UE from 63.79% to 16.35% and NRMS from 32.62% to 7.74%, through adjoint-based optimization.

Furthermore, we applied this algorithm to optimize the beam-splitters creating non-square arrays. One of the optimized results is shown in Fig. 4.7. The convergence plot over the

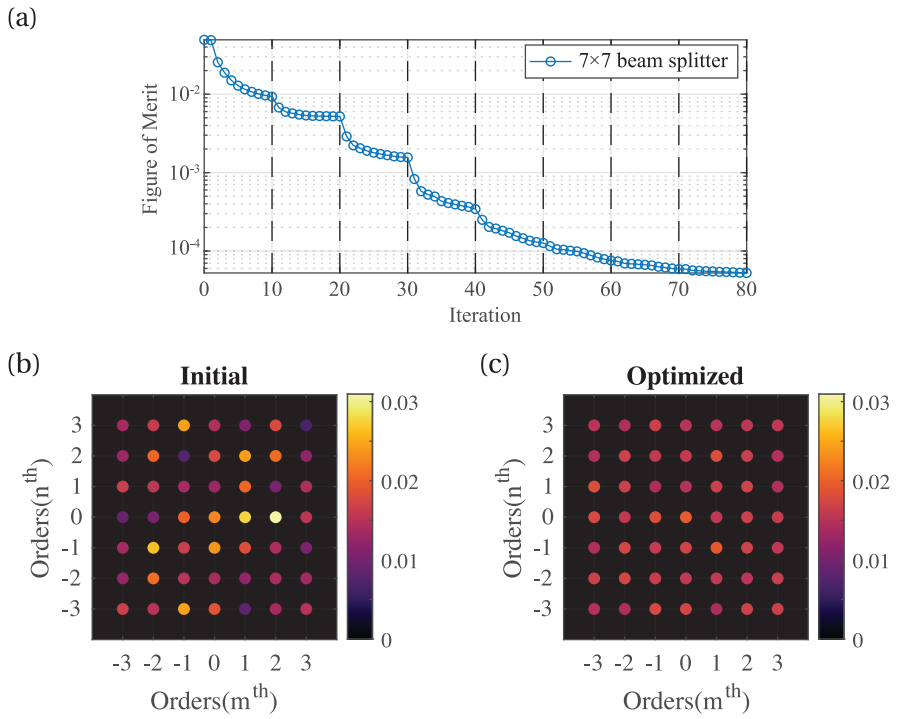


Figure 4.6 – Theoretical analysis of wide angle 7 × 7 diffractive beam splitters. (a) Plot of figure of merit over the course of the optimization process of 7 × 7 diffractive beam splitter. The simulated efficiency of diffractive beam splitter (b) before and (c) after optimization.

optimization of a 5x7 beam splitter is presented in Fig. 4.7(a). Over the course of multiple iterations, the dielectric continuum in the device converges to the dielectric constant of either silica or air. The simulated diffraction pattern from initial dielectric distribution and the final one after optimization is presented in Fig. 4.7(b) and (c), respectively. We can observe the diffraction pattern distribution of optimized design is a nearly identical intensity to every target spot. The diffraction efficiency in target orders are given in Table 4.5. Over the optimization process, 7 × 5 spot-array generator also has significant improvement in UE from 81.1% to 6.98% and NRMS from 37.93% to 3.78%. Moreover, the total diffraction efficiency of 35 spots created by this fan-out element slightly increase from 74.45% to 78.48%. The numerical accuracy of these theoretical values, calculated by RCWA solver and has less than 0.2% error due to computing with enough large number of Fourier harmonic modes.

By comparison, ref [71] achieved 17.4 % of uniformity error and 71.4 % of total efficiency in 5 × 5 beam splitter with maximal 35° of diffraction angle using a genetic algorithm which is one kind of meta-heuristic optimization often required high computation cost. Thus, gradient-based optimization with adjoint-state-method, with much lower computational cost, is able to yield better results, i.e. better uniformity, higher efficiency, and larger angle, than optimization based on genetic algorithm.

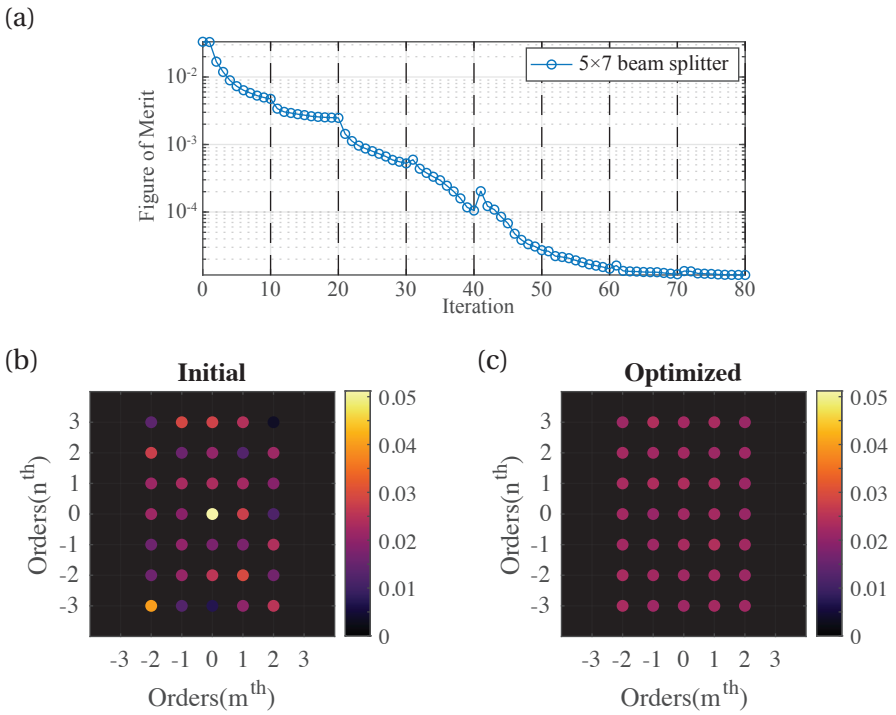


Figure 4.7 – Theoretical analysis of wide angle 7 × 7 diffractive beam splitters. (a) Plot of figure of merit over the course of the optimization process of 7 × 7 diffractive beam splitter. The simulated efficiency of diffractive beam splitter (b) before and (c) after optimization.

Table 4.4 – The diffraction efficiencies of 7 × 7 beam spitter before and after optimization

Initial

| $n$ \ $m$ | -3 | -2 | -1 | 0 | 1 | 2 | 3 |
|---|---|---|---|---|---|---|---|
| -3 | 1.67 % | 1.53 % | 2.47 % | 1.87 % | 0.82 % | 1.38 % | 1.50 % |
| -2 | 1.24 % | 2.10 % | 1.53 % | 1.40 % | 1.23 % | 1.41 % | 1.36 % |
| -1 | 1.38 % | 2.66 % | 1.65 % | 2.37 % | 1.83 % | 1.43 % | 1.07 % |
| 0 | 0.90 % | 1.05 % | 2.00 % | 2.26 % | 2.77 % | 3.09 % | 1.55 % |
| 1 | 1.65 % | 1.56 % | 1.38 % | 1.32 % | 2.04 % | 1.05 % | 1.44 % |
| 2 | 1.29 % | 2.03 % | 0.77 % | 1.75 % | 2.42 % | 2.09 % | 1.20 % |
| 3 | 1.37 % | 1.62 % | 2.45 % | 1.46 % | 1.07 % | 1.77 % | 0.68 % |

Optimized

| $n$ \ $m$ | -3 | -2 | -1 | 0 | 1 | 2 | 3 |
|---|---|---|---|---|---|---|---|
| -3 | 1.47 % | 1.45 % | 1.76 % | 1.74 % | 1.41 % | 1.69 % | 1.68 % |
| -2 | 1.68 % | 1.74 % | 1.64 % | 1.58 % | 1.58 % | 1.54 % | 1.65 % |
| -1 | 1.44 % | 1.74 % | 1.61 % | 1.71 % | 1.93 % | 1.68 % | 1.58 % |
| 0 | 1.75 % | 1.60 % | 1.82 % | 1.96 % | 1.58 % | 1.68 % | 1.62 % |
| 1 | 1.82 % | 1.67 % | 1.43 % | 1.50 % | 1.67 % | 1.70 % | 1.46 % |
| 2 | 1.48 % | 1.68 % | 1.59 % | 1.62 % | 1.82 % | 1.65 % | 1.47 % |
| 3 | 1.53 % | 1.44 % | 1.67 % | 1.53 % | 1.52 % | 1.56 % | 1.58 % |

Table 4.5 – The diffraction efficiencies of 5 × 7 beam spitter before and after optimization

Initial

| $n$ \ $m$ | -2 | -1 | 0 | 1 | 2 |
|---|---|---|---|---|---|
| -3 | 4.02 % | 1.23 % | 0.72 % | 2.00 % | 2.54 % |
| -2 | 1.58 % | 2.07 % | 2.55 % | 2.94 % | 1.63 % |
| -1 | 1.59 % | 2.02 % | 1.73 % | 1.76 % | 2.42 % |
| 0 | 2.19 % | 1.93 % | 5.12 % | 2.76 % | 1.17 % |
| 1 | 2.15 % | 2.29 % | 2.32 % | 2.24 % | 1.89 % |
| 2 | 2.76 % | 1.55 % | 2.03 % | 1.25 % | 2.16 % |
| 3 | 1.38 % | 2.89 % | 2.80 % | 2.45 % | 0.35 % |

Optimized

| $n$ \ $m$ | -2 | -1 | 0 | 1 | 2 |
|---|---|---|---|---|---|
| -3 | 2.30 % | 2.19 % | 2.19 % | 2.28 % | 2.21 % |
| -2 | 2.32 % | 2.24 % | 2.21 % | 2.27 % | 2.16 % |
| -1 | 2.24 % | 2.19 % | 2.28 % | 2.41 % | 2.22 % |
| 0 | 2.26 % | 2.09 % | 2.22 % | 2.27 % | 2.11 % |
| 1 | 2.32 % | 2.35 % | 2.36 % | 2.33 % | 2.15 % |
| 2 | 2.27 % | 2.20 % | 2.23 % | 2.17 % | 2.19 % |
| 3 | 2.18 % | 2.38 % | 2.25 % | 2.31 % | 2.13 % |

### 4.4.2 Fan-out elements with tailored intensity distribution

We applied our optimization method to the diffractive beam splitter with tailored power distribution corresponding to Fig.4.8. As listed in Table 4.6, we specify different 9 groups have spot array with a specific intensity ratio, where group A, B, C, D, E, B', C', D' and E' have 1.0, 1.5, 2.0, 2.5, 1.0, 1.5, 2.0, 2.5 and 1.0 of intensity ratio, respectively.

Table 4.6 – The target efficiency depends on groups in beam splitter with tailored intensity distribution

| Groups | A | B<br>B' | C<br>C' | D<br>D' | E<br>E' |
|---|---|---|---|---|---|
| Efficiency ratio | 1.0 | 1.5 | 2.0 | 2.5 | 1.0 |
| Target efficiency (%) | 1.63 | 2.45 | 3.27 | 4.08 | 1.63 |

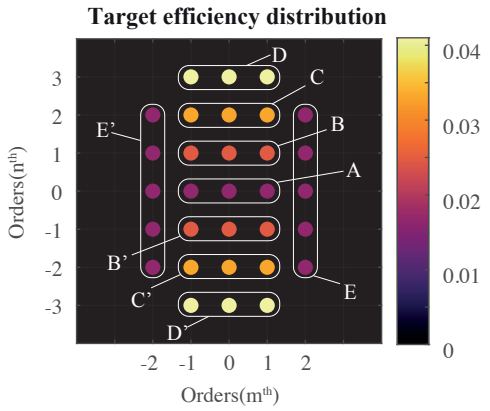


Figure 4.8 – The target diffraction pattern for diffractive beam splitter with designated intensity distribution. The target efficiency depends on the groups, where group A, B, C, D, E, B', C', D' and E' have 1.0, 1.5, 2.0, 2.5, 1.0, 1.5, 2.0, 2.5 and 1.0 of intensity ratio, respectively. (see Table 4.6)

To optimize this diffractive beam splitter, we also use the figure of merit function in Eq. 2.64 with target efficiency distribution of above entries (see Table 4.6). Over the course of multiple iterations, the dielectric continuum in the device converges to the dielectric constant of either silica or air from the initial dielectric distribution designed by IFTA. We finally obtain a diffraction pattern distribution of optimized design nearly identical to the target pattern. The optimization convergence and the geometry of the fan-out element during optimization are shown in the Fig. 4.9. The optimization process is performed iteratively and typically takes 100 – 200 iterations to achieve convergence. Figure 4.9(a) shows the merit function as a function of the optimization iterations for beam-splitter generating the tailored spot array in the main text. The dash lines indicate the updating of projection strength $\beta$. The patterns in a single period of the element at different stages of the process are presented in Fig. 4.9(b).

The geometry and the simulated diffraction efficiency distributions of diffractive beam splitters

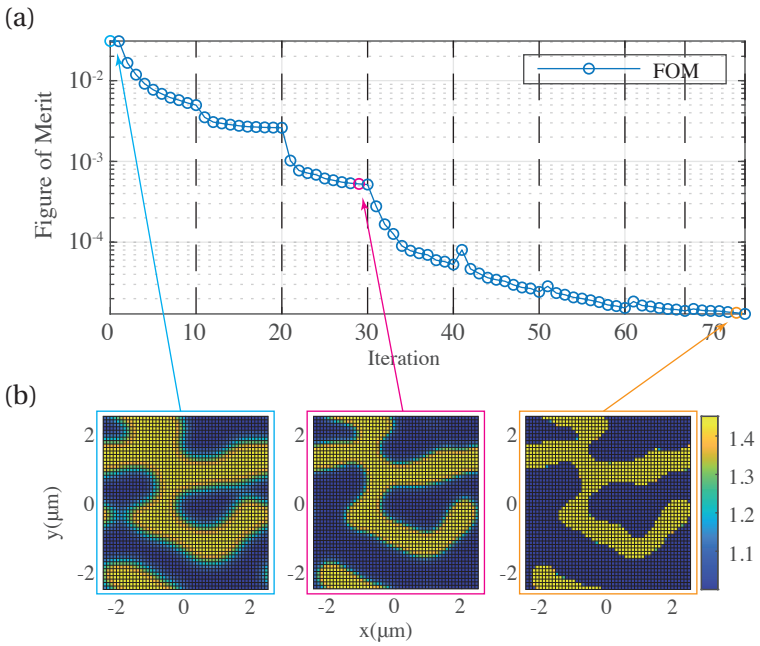


Figure 4.9 – (a) a plot of the figure of merit over the course of the optimization process for the beam splitter with tailored intensity distribution. (b) Three figures show refractive indices distributions of the device at different stages of the optimization process.

after optimization is shown in Fig. 4.10. We optimize the elements in different polarized incident wave: TE- and TM-polarization. The final geometry and diffraction efficiency for TE-polarized incident wave is presented in Fig. 4.10(a) and (b). The fill factor of the dielectric material of this element is 34.08 %. In addition, total efficiency of this fan-out element slightly increases from 75.20 % to 78.28 % and UE and NRMS consequently reach 8.45 % from 74.73 % and 4.14 % from 55.15 %.

The optimized geometry and diffraction efficiency for TM-polarized incident wave is presented in Fig. 4.10(c) and (d). Quantitatively, total efficiency of this DOE slightly increases from 71.99 % to 77.65 % and UE and NRMS consequently reach 13.30 % from 85.48 % and 4.74 % from 54.98 %. The fill factor of the dielectric material of the element is 32.00 %.

These results prove that the optimization algorithm is suitable for designing wide-angle diffractive beam splitters with various shapes of spot array and intensity distributions. For instance, the proposed optimization strategy can be also used for an even number of fan-out beam splitters, with a zero intensity in zeroth order. Based on optimized designs, we fabricated and characterized diffractive beam-splitters. The details of the experimental results are presented in the following section.

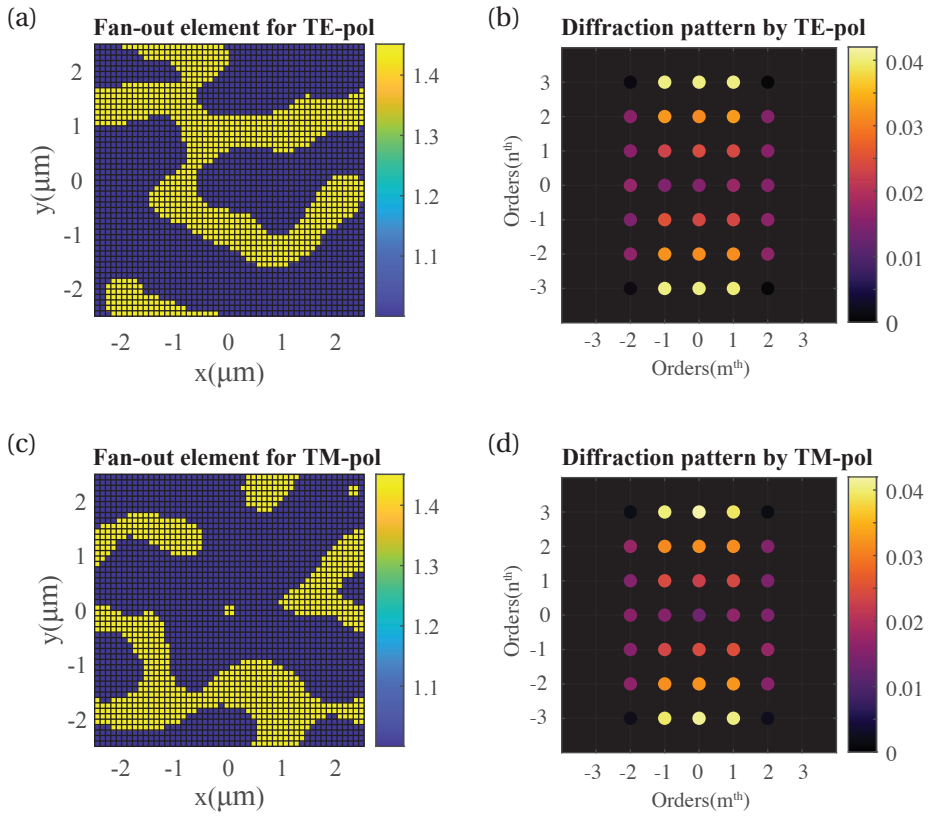


Figure 4.10 – Theoretical analysis of diffractive beam splitters with tailored intensity distribution. (a) Top view of a two-dimensional binary grating for TE-polarized incident wave. The color bar indicates the refractive index. (b) The calculated efficiency of diffractive beam splitter of (a) with TE-pol incident wave. (c) Top view of fan-out element for TM-polarized incident wave. (d) The calculated diffraction distribution from the fan-out element in (c) with TM-pol incident wave.

### 4.4.3 Experimental results

The diffractive beam splitters were fabricated by lithography using electron-beam and dry etching to create a chromium etch mask, and then by reactive ion etching to obtain $SiO_2$ binary surface relief structures. The optical elements are optically characterized using a TE- and TM-polarized 940 nm wavelength beam as our input source. We detect the diffracted light beams using a mobile single-pixel detector with a high dynamic range. To focus on both the simulation and experiment to facilitate a quantitative comparison, we applied the loss by Fresnel reflection from the interface between air and $SiO_2$ substrate to simulated efficiency of DOEs.

Experimental diffraction efficiencies of $7 \times 7$ beam splitter and $5 \times 7$ beam splitter are shown in Fig. 4.11, respectively. The experimental data show that these devices operate with good uniformity which is close to the theoretical values. The $7 \times 7$ beam splitter sample has a total efficiency of 75.35 %, UE of 23.35 %, and NRMS of 12.76 %. The $5 \times 7$ beam splitter sample has a total efficiency of 73.86 %, UE of 14.42 %, and NRMS of 10.50 %. The properties based on the measurement are considerably close to the results obtained by calculation in the previous section. The comparison between theoretical and experimental diffraction efficiencies of $7 \times 7$ and $5 \times 7$ beam-splitter creating uniform intensity array is presented in Table 4.7. To exclude the effects which may occur during measurement such as Fresnel reflection loss and power detector offset, the measured efficiency is normalized. The results of the comparison show that the experimental results have a strong correlation with the designs. Little discrepancies between the experimental and theoretical efficiencies are due in part to minor geometric imperfections in the fabricated device. In general the diffraction efficiency in orders often strongly depends on the errors in fabrication processes, e.g., etching depth, feature width, slope steepness, and feature rounding. Overall, the optimized samples display experimental performances which are significantly higher than the theoretical performances of initial devices before optimization.

Table 4.7 – Comparison with the theoretical and experimental properties of the $7 \times 7$ and $5 \times 7$ beam splitters. The calculated efficiency takes into account the loss from Fresnel reflection in the air-$SiO_2$ substrate interface.

| | $7 \times 7$ beam splitter | | $5 \times 7$ beam splitter | |
|---|---|---|---|---|
| | Calculated | Measured | Calculated | Measured |
| Diffraction efficiency (%) | 77.01 | 75.35 | 75.83 | 73.86 |
| UE (%) | 16.35 | 23.35 | 06.98 | 14.42 |
| NRMS (%) | 08.35 | 12.76 | 06.10 | 10.50 |

For an accurate comparison between theoretical and measured results, we analyze the correlation of these data using mean absolute percentage deviation (MAPD) as a ratio defined by

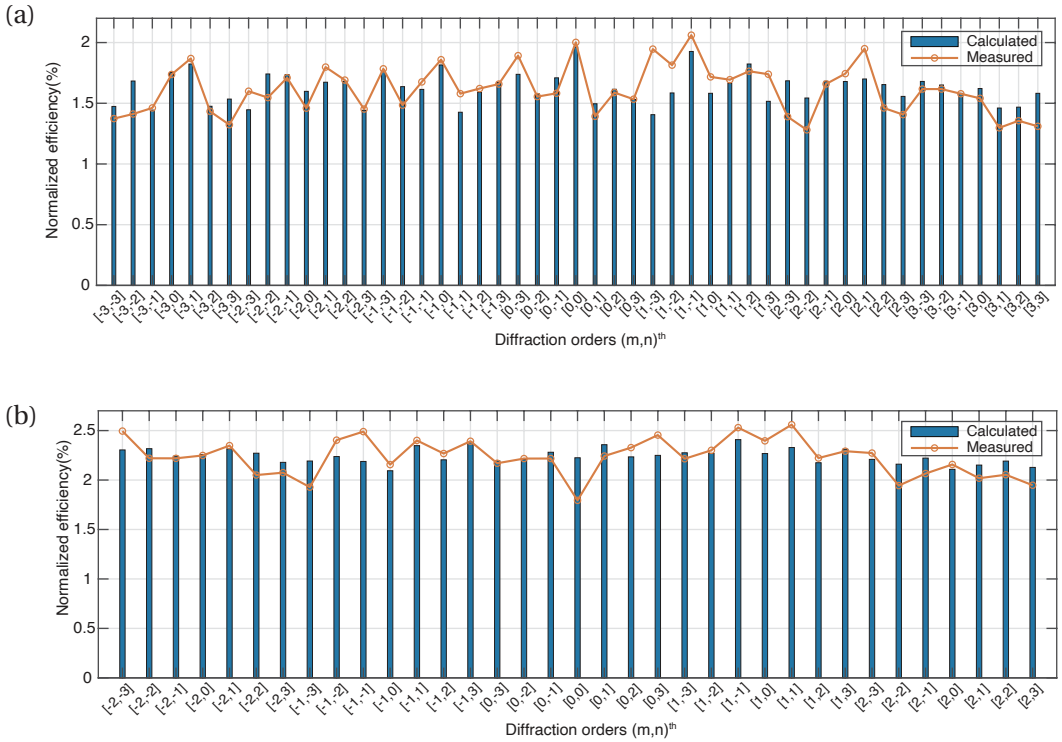


Figure 4.11 – Experimental characterization of fan-out grating devices. The measured (orange line) and simulated efficiency (blue bar) of (c) 7x7 beam splitter and (d) 5x7 beam splitter.

the formula:

$$\mathrm{MAPD} = \frac{1}{T}\sum\left|\frac{\eta^{S}_{mn}-\eta^{E}_{mn}}{\eta^{S}_{mn}}\right| \tag{4.19}$$

where $\eta^{S}_{mn}$,$\eta^{E}_{mn}$ are simulated and experimental efficiency in $(m,n)^{\mathrm{th}}$ diffraction orders and $T$ is the total number of diffraction orders in 2D array. The MAPDs of $7\times7$ and $7\times5$ beam splitters are calculated to 7.24 % and 5.00 %, respectively, which represents measurements demonstrate excellent reproducibility of the simulated results in a quantitative manner.

We also measured the diffraction efficiency of tailored-intensity-level beam splitters fabricated based on optimized design. A scanning electron microscopy (SEM) image of the optical elements are presented in Fig. 4.12(a) and (c), and theoretical and experimental diffraction efficiencies of the beam splitters with array groups and their objective efficiency are summarized in 3.10(b) and (d). Tilted SEM images of the beam-splitter show vertical sidewalls, indicative of high-quality etching.

The experimental plot shows that these elements operate with excellent agreement with respect to the objective in the overall intensity distributions. For an accurate comparison, we present the total diffraction efficiency, UE, and RMSE of simulated and measured one in Table 4.8. The UE and NRMS of the fabricated sample are measured to 14.54 % and 9.81 %,

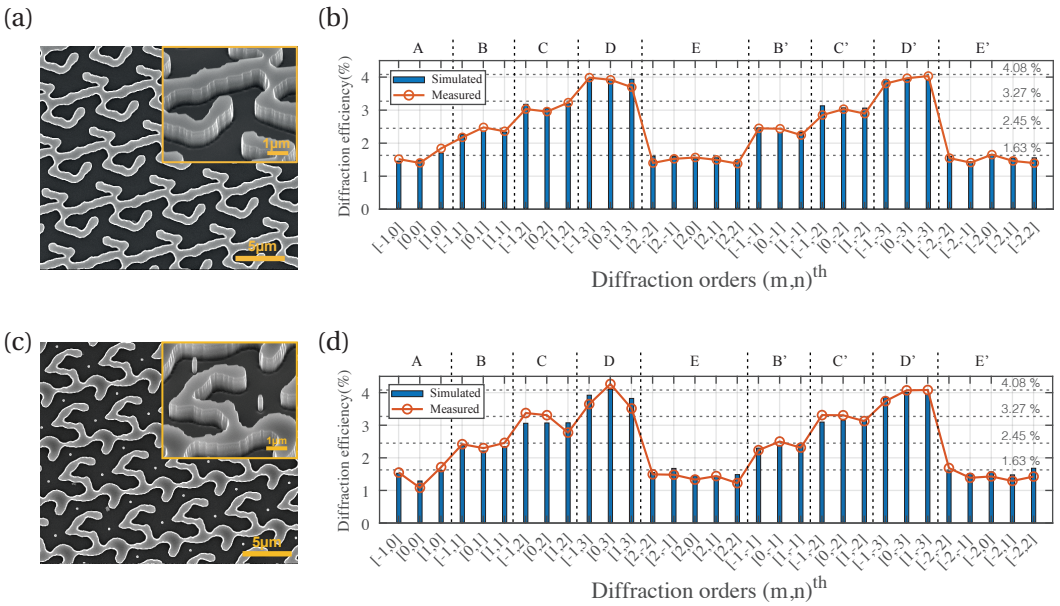


Figure 4.12 – Experimental characterization of the diffractive beam splitter with designated intensity distribution. Scanning electron microscopy images of the diffractive beam splitters for (a)TE-polarized and (c) TM-polarized incident waves. Top insets: magnified tilted-view image of a grating unit cell. The measured (orange line) and simulated (blue bar) efficiency of a beam splitter with tailored power distribution from (b)TE-polarized (d)TM-polarized incident wave. The dash lines indicate the groups and their target efficiency

respectively. Moreover, the results of the comparison show that the experimental results have a strong correlation with the theoretical results, where the MAPD of this beam splitter is calculated to 5.99 %. The only noticeable deviation in the measurement is a small mismatch of diffraction efficiency in a few orders that emerge due to minor fabrication errors. In general the diffraction efficiency in orders often strongly depends on the errors in fabrication processes, e.g., etching depth, feature width, slope steepness, and feature rounding. Nevertheless, the fabricated samples based on optimized design overall display experimental performances which are significantly higher than the theoretical performances of initial designs before optimization. In other words, our methodology can readily create robust high-performance, multifunctional optical elements with wide-angle spot array that show theoretical and experimental performances that far exceed the previous record for manufacturable diffractive beam splitters recently reported [71–73], at much less computational cost than previous methods.

Table 4.8 – Comparison with the simulated and experimental properties of the beam splitters with tailored power distribution. The simulated efficiency take into account the loss from Fresnel reflection in the air-$SiO_2$ substrate interface.

| | Beam splitter for TE-pol | | Beam splitter for TM-pol | |
|---|---|---|---|---|
| | Calculated | Measured | Calculated | Measured |
| Diffraction efficiency (%) | 75.63 | 74.20 | 75.02 | 74.16 |
| UE (%) | 08.46 | 14.54 | 13.30 | 23.11 |
| NRMS (%) | 06.57 | 09.81 | 08.13 | 12.75 |

## 4.5 Summary

In summary, we utilized the adjoint state method in optimizing the topology of optical elements, which is able to create high-performance, multi-functional wide-angle DOEs at a very low computational cost. We explored properties of the optimization method, such as efficient computation for the gradient of the target function with respect to high-dimensional design parameters with rigorous diffraction theory, and discussed the optimization method can readily extend to not only the diffraction beam splitter with equal intensity distribution but also DOE with the tailored intensity distribution. As a case study, we applied gradient-based optimization with adjoint-state method to $7\times7$, $7\times5$ beam splitter and designated-power-level beam splitter with non-paraxial diffraction angle, i.e. maximal diffraction angle is 53°, 43° and 37° from center, respectively. The optimized beam splitters show considerable improvement of uniformity while maintaining the initial diffraction efficiency. The experimental results obtained by the illumination of the fabricated optical elements using an incident laser of 940 nm wavelength with a normal incident angle have been compared with the numerical results. As numerical simulation and experimental results were found to be in excellent agreement, our optimization method can be considered proven to be an effective design tool for wide-angle diffractive beam splitters creating various diffraction distributions. We envision that these methods in diffractive optics will extend to other high-performance, multi-functional optical elements which will enable the next generation of photonics systems such as compact optical sensors.

# 5 Conclusion

This thesis aimed to develop optimization tools for wide diffraction angle diffractive optical elements (DOEs) beyond the limits of scalar paraxial diffraction theory. For this purpose, we have examined optimization methodologies based on both the approximate step transition perturbation approach (STPA) and rigorous coupled-wave analysis (RCWA) which have shown computationally efficient, accurate performances, and overcoming the limits of the conventional tools based on scalar diffraction theory such as thin element approximation (TEA).

## 5.1 Summary

The gradient-based optimizations have been one of the most important computational optimization techniques to design a structure based on certain specifications, which can lead to the discovery of many structures with superior performance. With gradient-based optimization, the inverse problem in a large number of design parameters space can be solved if we efficiently obtain the gradient of the figure of merit with respect to design variables. These methodologies are realized by the STPA, in which the gradient of a merit function with respect to design parameters can be expressed analytically, and by the adjoint method, in which the gradient of an objective function with respect to all design variables can be computed using only two rigorous electromagnetic simulations.

One- (1D) and two-dimensional (2D) diffractive elements were used to analyze the potential of our approaches. The optical functionality of these elements is beam splitting which allowed an easy interpretation of the quality by the parameters of diffraction efficiency and uniformity of diffraction distribution. We have focused on designing the binary, i.e., 2-level microstructures because they are easier to fabricate than multi-level or continuous surface structures and thus are attractive for many optical systems.

We first clarified the limits of TEA by comparing it with the simulated fields after the vertical transition in surface profile using TEA and RCWA. The difference between the fields computed

from TEA and RCWA was expressed by field perturbation. The STPA is a model that combines the TEA with these perturbation distributions after the surface profile of the elements. If we used the positions of transition points as design parameters in the fan-out elements, we can describe an analytical solution of diffraction efficiency with respect to the positions of transition points of the optical element due to this perturbation contribution term in STPA. It was allowed us to calculate the gradient straightforwardly with accuracy. Applying these optimization tools to various 1D diffractive beam splitters, we obtained the optimized solutions with considerable improvement in uniformity of diffraction pattern distribution.

We then discussed the adjoint method with RCWA to optimize the elements with smaller features or 2D fan-out elements. Due to the adjoint method, we can compute the gradient of the figure of merit with respect to design parameters efficiently even using rigorous diffraction calculation, independently of the number of design parameters. Hence, the permittivity distribution in the geometry of fan-out gratings is used in design variables during the optimization. With the adjoint method, to compute the derivatives of diffraction efficiency with respect to the permittivity at all pixels in a grating, two RCWA simulations are required. Fabrication constraints were added to the optimization to ensure that the final output converges to a binary structure with feasible features. We applied gradient-based optimization with the adjoint method to wide angle 2D beam splitters with maximal diffraction angle was up to 53° from the center to diagonal edges, which is beyond the limit of the scalar paraxial diffraction regime. The optimized beam splitters showed considerable improvement of uniformity while maintaining the initial diffraction efficiency. In addition, we proved to create tailored-power-level beam splitters meeting the application's requirement using this optimization method.

The evaluation of our approaches was done by testing the optical performances of fabricated elements. The results of the experimental characterization were compared to the simulated diffraction distributions and optical efficiencies of the elements. The results of the comparison showed that the experimental results have a strong correlation with the designs.

## 5.2 Outlook

The results of this thesis show that the wide-angle DOEs are realized by our approaches. While the fan-out gratings with various diffraction pattern distribution are presented in this thesis, some challenging tasks remain to extend these approaches to various diffractive optical elements more than a binary fan-out element for normal incident monochromatic wave.

For instance, to create multilevel structures i.e., 8-level or 16-level elements, quantization methodologies would be required to making the final structure have multilevel depth during the optimization process in the optimization based on adjoint method cases. In addition, New fabrication constraints or penalty functions would be studied to design robust and feasible features to survive during the fabrication process.

One may demand multi-function DOEs such as a fan-out grating creating different diffraction

patterns depends on the polarization of incident wave or different wavelength. Then, the multi-objective FOM would be defined to incorporate several FOMs together during the optimization process. Among various merit functions, the effect of the weighted ratio of each FOM would be studied to create high performance multi-function DOEs. Furthermore, one can ask that the robust DOEs in broadband illumination or various incident angle? Solving these challenges would allow us to access the potential of this technology for a new generation of DOEs as well as to resolve potential technological drawbacks such as the wavelength sensitivity of the DOEs. These solutions to challenges would be possible to implement with our approaches or we may use other optimization techniques such as deep learning.

# Publications

## Journal papers

D. C. Kim, A. Hermerschmidt, P. Dyachenko, and T. Scharf. “Inverse design of diffractive optical elements using step-transition perturbation approach”. *Advanced Optical Technologies*, 2020. DOI: 10.1515/aot-2020-0046

D. C. Kim, A. Hermerschmidt, P. Dyachenko, and T. Scharf. “Inverse design and demonstration of high-performance wide-angle diffractive optical elements”. *Optics Express* 28, p. 22321, 2020. DOI: 10.1364/OE.394442

M. Symeonidis, W. Nakagawa, D. C. Kim, A. Hermerschmidt, and T. Scharf. “High-resolution interference microscopy of binary phase diffractive optical elements”. *OSA Continuum* 2, p. 2496, 2019. DOI: 10.1364/OSAC.2.002496

## Proceedings and conference presentations

D. C. Kim, A. Hermerschmidt, P. Dyachenko, and T. Scharf. “Adjoint method and inverse design for diffractive beam splitters”. In: *Components and Packaging for Laser Systems VI.*. Ed. by A. L. Glebov and P. O. Leisher. Vol. 1126115. February. SPIE, Feb. 2020. P. 41. DOI: 10.1117/12.2543367

D. C. Kim, A. Hermerschmidt, P. Dyachenko, and T. Scharf. “Adjoint-based Optimization for Diffractive Beam-Splitters”. In: *2019 24th Microoptics Conference (MOC)*.. Nov. 2019. Pp. 266–267. DOI: 10.23919/MOC46630.2019.8982782

D. C. Kim, P. Dyachenko, A. Hermerschmidt, and T. Scharf. “Design and analysis of binary fan-out gratings based on step-transition perturbation approach”. In: *Laser Resonators, Microresonators, and Beam Control XXI.*. Ed. by A. V. Kudryashov, A. H. Paxton, and V. S. Ilchenko. March. SPIE, Mar. 2019. P. 55. DOI: 10.1117/12.2507925

M. Symeonidis, D. C. Kim, A. Hermerschmidt, M.-S. Kim, and T. Scharf. “Diffractive optical elements investigation in the phase domain”. In: *Optical Components and Materials XVI.*. Ed. by M. J. Digonnet and S. Jiang. February. SPIE, Feb. 2019. P. 72. DOI: 10.1117/12.2509668

D. C. Kim, P. Dyachenko, A. Hermerschmidt, and T. Scharf. *Gradient-based optimization with step-transition perturbation approach for 1D binary diffractive beam splitters.* Paper presented at European Optical Society Biennial Meeting 2018, Delft, Netherlands. 2018, Oct

# Bibliography


[1] D. C. Kim, A. Hermerschmidt, P. Dyachenko, and T. Scharf. “Inverse design and demonstration of high-performance wide-angle diffractive optical elements”. *Optics Express* 28, p. 22321, 2020. DOI: 10.1364/OE.394442. (See pp. 1, 83).

[2] D. C. Kim, A. Hermerschmidt, P. Dyachenko, and T. Scharf. “Inverse design of diffractive optical elements using step-transition perturbation approach”. *Advanced Optical Technologies*, 2020. DOI: 10.1515/aot-2020-0046. (See pp. 1, 83).

[3] D. C. Kim, A. Hermerschmidt, P. Dyachenko, and T. Scharf. “Adjoint method and inverse design for diffractive beam splitters”. In: *Components and Packaging for Laser Systems VI*. Ed. by A. L. Glebov and P. O. Leisher. Vol. 1126115. February. SPIE, Feb. 2020. P. 41. DOI: 10.1117/12.2543367. (See pp. 1, 83).

[4] D. C. Kim, P. Dyachenko, A. Hermerschmidt, and T. Scharf. “Design and analysis of binary fan-out gratings based on step-transition perturbation approach”. In: *Laser Resonators, Microresonators, and Beam Control XXI*. Ed. by A. V. Kudryashov, A. H. Paxton, and V. S. Ilchenko. March. SPIE, Mar. 2019. P. 55. DOI: 10.1117/12.2507925. (See pp. 1, 83).

[5] C. J. Alleyne and A. G. Kirk. “Rigorous coupled wave analysis applied to transmission efficiency of diffractive beam array relays for free-space optical interconnects”. *Appl. Opt.* 44, pp. 1200–1206, 2005. DOI: 10.1364/AO.44.001200. (See p. 1).

[6] M. Beyerlein, N. Lindlein, and J. Schwider. “Dual-wave-front computer-generated holograms for quasi-absolute testing of aspherics”. *Appl. Opt.* 41, pp. 2440–2447, 2002. DOI: 10.1364/AO.41.002440. (See p. 1).

[7] Z. Ghadyani, I. Vartiainen, I. Harder, W. Iff, A. Berger, N. Lindlein, et al. “Concentric ring metal grating for generating radially polarized light”. *Appl. Opt.* 50, pp. 2451–2457, 2011. DOI: 10.1364/AO.50.002451. (See p. 1).

[8] Z. Ghadyani, S. Dmitriev, N. Lindlein, G. Leuchs, O. Rusina, and I. Harder. “Discontinuous space variant sub-wavelength structures for generating radially polarized light in visible region”. *Journal of the European Optical Society: Rapid Publications* 6, p. 11041, 2011. DOI: 10.2971/jeos.2011.11041. (See p. 1).

[9] G. S. Khan, K. Mantel, I. Harder, N. Lindlein, and J. Schwider. "Design considerations for the absolute testing approach of aspherics using combined diffractive optical elements". *Appl. Opt.* 46, pp. 7040–7048, 2007. DOI: 10.1364/AO.46.007040. (See p. 1).

[10] E. Y. Lam and A. K. K. Wong. "Computation lithography: virtual reality and virtual virtuality". *Opt. Express* 17, pp. 12259–12268, 2009. DOI: 10.1364/OE.17.012259. (See p. 1).

[11] D. Lehr, M. Helgert, M. Sundermann, C. Morhard, C. Pacholski, J. P. Spatz, et al. "Simulating different manufactured antireflective sub-wavelength structures considering the influence of local topographic variations". *Opt. Express* 18, pp. 23878–23890, 2010. DOI: 10.1364/OE.18.023878. (See p. 1).

[12] Y. Sheng, D. Feng, and S. Larochelle. "Analysis and synthesis of circular diffractive lens with local linear grating model and rigorous coupled-wave theory". *J. Opt. Soc. Am. A* 14, pp. 1562–1568, 1997. DOI: 10.1364/JOSAA.14.001562. (See p. 1).

[13] F. Simon, G. Khan, K. Mantel, N. Lindlein, and J. Schwider. "Quasi-absolute measurement of aspheres with a combined diffractive optical element as reference". *Appl. Opt.* 45, pp. 8606–8612, 2006. DOI: 10.1364/AO.45.008606. (See p. 1).

[14] E. Hecht. *Optics*. 4th ed. Addison-Wesley, 2002. Chap. 1. (See p. 1).

[15] A. Tbakhi and S. S. Amr. "Ibn Al-Haytham: Father of Modern Optics". *Annals of Saudi Medicine* 27, pp. 464–467, 2007. DOI: 10.5144/0256-4947.2007.464. (See p. 2).

[16] F. Grimaldi. *Physico-mathesis de lumine, coloribus, et iride, aliisque adnexis libri duo: opus posthumum*. Ex typographia haeredis Victorii Benatii, impensis Hieronymi Berniae, 1665. (See p. 2).

[17] R. Hooke, J. Allestry, and J. Martyn. *Micrographia, or, Some physiological descriptions of minute bodies made by magnifying glasses :with observations and inquiries thereupon*. 1665. (See p. 2).

[18] C. Huygens. *Traité de la lumière, où sont expliquées les causes de ce qui luy arrive dans la réflexion, et dans la réfraction, et particulièrement dans l'étrange réfraction du cristal d'Islande: Avec un discours de la cause de la pesanteur*. Pierre van der Aa, 1690. (See p. 2).

[19] T. Young. "The Bakerian Lecture: On the Theory of Light and Colours". *Philosophical Transactions of the Royal Society of London* 92, pp. 12–48, 1802. (See p. 2).

[20] A. Fresnel, H. de Senarmont, and É. Verdet. *Oeuvres complètes d'Augustin Fresnel*. Oeuvres complètes d'Augustin Fresnel v. 1. Impr. Impériale, 1866. (See p. 2).

[21] F. Arago, J. Barral, and P. Flourens. *Œuvres complètes de François Arago*. Œuvres complètes de François Arago v. 8. Gide et J. Baudry, 1858. (See p. 2).

[22] G. Kirchhoff. "Zur Theorie der Lichtstrahlen". *Annalen der Physik* 254, pp. 663–695, 1883. DOI: 10.1002/andp.18832540409. (See p. 2).

[23] J. C. Maxwell. "On physical lines of force". *Philosophical Magazine*, 2010. DOI: 10.1080/14786431003659180. (See pp. 2, 7).

[24] F. Hopkinson and D. Rittenhouse. “An Optical Problem, Proposed by Mr. Hopkinson, and Solved by Mr. Rittenhouse”. *Transactions of the American Philosophical Society* 2, pp. 201–206, 1786. (See p. 2).

[25] J. von Fraunhofer. *Neue Modifikation des Lichtes durch gegenseitige Einwirkung und Beugung der Strahlen, und Gesetze derselben*. Lentner, 1822. (See p. 2).

[26] D. Gabor. “A New Microscopic Principle”. *Nature* 161, pp. 777–778, 1948. DOI: 10.1038/161777a0. (See p. 2).

[27] D. Gabor. “Microscopy by reconstructed wave-fronts”. *Proceedings of the Royal Society of London. Series A. Mathematical and Physical Sciences* 197, pp. 454–487, 1949. DOI: 10.1098/rspa.1949.0075. (See p. 2).

[28] T. Mulvey. “Gabor’s Pessimistic 1942 View of Electron Microscopy and How He Stumbled on the Nobel Prize”. In: *Advances in Imaging and Electron Physics*. 1995. Pp. 259–283. DOI: 10.1016/S1076-5670(08)70113-7. (See p. 2).

[29] E. N. Leith and J. Upatnieks. “Reconstructed Wavefronts and Communication Theory*”. *J. Opt. Soc. Am.* 52, pp. 1123–1130, 1962. DOI: 10.1364/JOSA.52.001123. (See p. 2).

[30] A. W. Lohmann and D. P. Paris. “Binary Fraunhofer Holograms, Generated by Computer”. *Applied Optics* 6, p. 1739, 1967. DOI: 10.1364/AO.6.001739. (See pp. 2, 38).

[31] B. R. Brown and A. W. Lohmann. “Computer-generated Binary Holograms*”. *IBM J. Res. Develop.* 13, pp. 160–168, 1969. DOI: 10.1147/rd.132.0160. (See p. 2).

[32] L. B. Lesem, P. M. Hirsch, and J. A. Jordan. “The Kinoform: A New Wavefront Reconstruction Device”. *IBM Journal of Research and Development* 13, pp. 150–155, 1969. DOI: 10.1147/rd.132.0150. (See p. 2).

[33] H. Dammann. “Blazed Synthetic Phase-Only Holograms”. *Optik*, 1970. (See p. 2).

[34] J. W. Goodman and A. M. Silvestri. “Some Effects of Fourier-domain Phase Quantization”. *IBM Journal of Research and Development* 14, pp. 478–484, 1970. DOI: 10.1147/rd.145.0478. (See p. 2).

[35] L. B. Lesem, P. M. Hirsch, and J. A. Jordan. “Scientific Applications: Computer synthesis of Holograms for 3-D display”. *Communications of the ACM* 11, pp. 661–674, 1968. DOI: 10.1145/364096.364111. (See p. 2).

[36] R. W. Gerchberg and W. O. Saxton. “A practical algorithm for the determination of phase from image and diffraction plane pictures”. *Optik* 35, pp. 237–246, 1972. DOI: 10.1070/QE2009v039n06ABEH013642. (See pp. 2, 30).

[37] N. C. Gallagher and B. Liu. “Method for Computing Kinoforms that Reduces Image Reconstruction Error”. *Applied Optics* 12, p. 2328, 1973. DOI: 10.1364/AO.12.002328. (See p. 2).

[38] F. Wyrowski. “Diffractive optical elements: iterative calculation of quantized, blazed phase structures”. *Journal of the Optical Society of America A* 7, p. 961, 1990. DOI: 10.1364/JOSAA.7.000961. (See p. 2).

[39] U. Mahlab, H. J. Caulfield, and J. Shamir. “Genetic algorithm for optical pattern recognition”. *Optics Letters* 16, p. 648, 1991. DOI: 10.1364/OL.16.000648. (See p. 2).

[40] D. R. Brown and A. D. Kathman. “Multielement diffractive optical designs using evolutionary programming”. In: *Diffractive and Holographic Optics Technology II*. Ed. by I. Cindrich and S. H. Lee. Apr. 1995. Pp. 17–27. DOI: 10.1117/12.207476. (See p. 2).

[41] S. Mellin and G. Nordin. “Limits of scalar diffraction theory and an iterative angular spectrum algorithm for finite aperture diffractive optical element design”. *Optics Express*, 2001. DOI: 10.1364/oe.8.000705. (See pp. 2, 4).

[42] M. T. Gale and K. Knop. “The Fabrication Of Fine Lens Arrays By Laser Beam Writing”. In: *Industrial Applications of Laser Technology*. Ed. by W. F. Fagan. Vol. 0398. October 1983. Oct. 1983. Pp. 347–353. DOI: 10.1117/12.935397. (See p. 2).

[43] V. P. Koronkevich, V. P. Kiryanov, V. P. Korolkov, A. G. Poleshchuk, V. V. Cherkashin, E. G. Churin, et al. “Fabrication of diffractive optical elements by direct laser-writing with circular scanning”. In: *5th International Workshop on Digital Image Processing and Computer Graphics (DIP-94)*. Ed. by N. A. Kuznetsov and V. A. Soifer. Vol. 2363. January 1995. Jan. 1995. Pp. 290–297. DOI: 10.1117/12.199647. (See p. 2).

[44] P. P. Clark and C. Londoño. “Production of kinoforms by single point diamond machining”. *Optics News* 15, 39_1, 1989. DOI: 10.1364/ON.15.12.0039_1. (See p. 2).

[45] S. M. Arnold. “Electron Beam Fabrication Of Computer-Generated Holograms”. *Optical Engineering* 24, pp. 339–343, 1985. DOI: 10.1117/12.7973578. (See p. 2).

[46] G. E. Moore. “Lithography and the future of Moore’s law”. In: *Electron-Beam, X-Ray, EUV, and Ion-Beam Submicrometer Lithographies for Manufacturing V*. Ed. by J. M. Warlaumont. Vol. 2437. International Society for Optics and Photonics. SPIE, 1995. Pp. 2–17. DOI: 10.1117/12.209151. (See p. 2).

[47] P. Twardowski, B. Serio, V. Raulot, and M. Guilhem. “Three-dimensional shape measurement based on light patterns projection using diffractive optical elements”. In: *Micro-Optics 2010*. Ed. by H. Thienpont, P. Van Daele, J. Mohr, and H. Zappe. Vol. 7716. May 2010. International Society for Optics and Photonics. SPIE, Apr. 2010. P. 77162I. DOI: 10.1117/12.854906. (See p. 3).

[48] O. Barlev and M. A. Golub. “Multifunctional binary diffractive optical elements for structured light projectors”. *Optics Express* 26, p. 21092, 2018. DOI: 10.1364/oe.26.021092. (See pp. 3, 4).

[49] S. Thibault, A. Arfaoui, and P. Desaulniers. “Cross-diffractive optical elements for wide angle geometric camera calibration”. *Optics Letters* 36, p. 4770, 2011. DOI: 10.1364/ol.36.004770. (See p. 3).

[50] F. Wyrowski and O. Bryngdahl. “Iterative Fourier-transform algorithm applied to computer holography”. *Journal of the Optical Society of America A* 5, p. 1058, 1988. DOI: 10.1364/JOSAA.5.001058. (See pp. 3, 30).

[51] M. Skeren, I. Richter, and P. Fiala. “Iterative Fourier transform algorithm: comparison of various approaches”. *Journal of Modern Optics* 49, pp. 1851–1870, 2002. DOI: 10.1080/09500340210140542. (See p. 3).

[52] S. BÜHLING and F. WYROWSKI. “Improved transmission design algorithms by utilizing variable-strength projections”. *Journal of Modern Optics* 49, pp. 1871–1892, 2002. DOI: 10.1080/09500340210140551. (See p. 3).

[53] J. W. Goodman. “Introduction to Fourier optics”. *Introduction to Fourier optics, 3rd ed., by JW Goodman. Englewood, CO: Roberts & Co. Publishers, 2005* 1, 2005. (See p. 3).

[54] G. Swanson. “Binary Optics Technology: Theoretical Limits on the Diffraction Efficiency of Multilevel Diffractive Optical Elements”. In: 1991. (See p. 3).

[55] A. Hermerschmidt, S. Krüger, and G. Wernicke. “Binary diffractive beam splitters with arbitrary diffraction angles”. *Optics Letters* 32, p. 448, 2007. DOI: 10.1364/OL.32.000448. (See p. 3).

[56] G.-N. Nguyen, K. Heggarty, A. Bacher, P.-J. Jakobs, D. Häringer, P. Gérard, et al. “Iterative scalar nonparaxial algorithm for the design of Fourier phase elements”. *Opt. Lett.* 39, pp. 5551–5554, 2014. DOI: 10.1364/OL.39.005551. (See p. 3).

[57] D. A. Pommet, M. G. Moharam, and E. B. Grann. “Limits of scalar diffraction theory for diffractive phase elements”. *Journal of the Optical Society of America A* 11, p. 1827, 1994. DOI: 10.1364/JOSAA.11.001827. (See pp. 3, 4).

[58] T. Vallius, P. Vahimaa, and M. Honkanen. “Electromagnetic approach to the thin element approximation”. *Journal of Modern Optics* 51, pp. 2079–2092, 2004. DOI: 10.1080/09500340412331286612. (See pp. 3, 36).

[59] M. G. Moharam and T. K. Gaylord. “Rigorous coupled-wave analysis of planar-grating diffraction”. *J. Opt. Soc. Am.* 71, pp. 811–818, 1981. DOI: 10.1364/JOSA.71.000811. (See pp. 3, 20).

[60] M. G. Moharam and T. K. Gaylord. “Diffraction analysis of dielectric surface-relief gratings”. *J. Opt. Soc. Am.* 72, pp. 1385–1392, 1982. DOI: 10.1364/JOSA.72.001385. (See pp. 3, 20).

[61] M. G. Moharam, E. B. Grann, D. A. Pommet, and T. K. Gaylord. “Formulation for stable and efficient implementation of the rigorous coupled-wave analysis of binary gratings”. *J. Opt. Soc. Am. A* 12, pp. 1068–1076, 1995. DOI: 10.1364/JOSAA.12.001068. (See pp. 3, 28).

[62] P. Lalanne and G. M. Morris. “Highly improved convergence of the coupled-wave method for TM polarization”. *Journal of the Optical Society of America A* 13, p. 779, 1996. DOI: 10.1364/JOSAA.13.000779. (See pp. 3, 20).

[63] L. Li. “New formulation of the Fourier modal method for crossed surface-relief gratings”. *Journal of the Optical Society of America A* 14, p. 2758, 1997. DOI: 10.1364/JOSAA.14.002758. (See pp. 3, 20, 23, 24, 26, 28).

[64] V. Liu and S. Fan. “S 4: A free electromagnetic solver for layered periodic structures”. *Computer Physics Communications* 183, pp. 2233–2244, 2012. DOI: 10.1016/j.cpc.2012.04.026. (See p. 3).

[65] W. Iff, T. Kämpfe, Y. Jourlin, and A. V. Tishchenko. “Memory sparing, fast scattering formalism for rigorous diffraction modeling”. *Journal of Optics* 19, p. 075602, 2017. DOI: 10.1088/2040-8986/aa7012. (See p. 3).

[66] A. Junker and K.-H. Brenner. “Achieving a high mode count in the exact electromagnetic simulation of diffractive optical elements”. *J. Opt. Soc. Am. A* 35, pp. 377–385, 2018. DOI: 10.1364/JOSAA.35.000377. (See p. 3).

[67] J. Jiang and G. Nordin. “A rigorous unidirectional method for designing finite aperture diffractive optical elements”. *Optics Express* 7, p. 237, 2000. DOI: 10.1364/oe.7.000237. (See p. 3).

[68] M. E. Testorf and M. A. Fiddy. “Efficient optimization of diffractive optical elements based on rigorous diffraction models”. *Journal of the Optical Society of America A* 18, p. 2908, 2001. DOI: 10.1364/josaa.18.002908. (See p. 3).

[69] D. Feng, Y. Yan, G. Jin, and S. Fan. “Design and fabrication of continuous-profile diffractive micro-optical elements as a beam splitter”. *Applied Optics* 43, pp. 5476–5480, 2004. DOI: 10.1364/AO.43.005476. (See p. 3).

[70] E. Noponen and J. Turunen. “Eigenmode method for electromagnetic synthesis of diffractive elements with three-dimensional profiles”. *J. Opt. Soc. Am. A* 11, pp. 2494–2502, 1994. DOI: 10.1364/JOSAA.11.002494. (See pp. 3, 20, 23).

[71] H. Hao, Z. Tingting, S. Qiang, and Y. Xiaodong. “Wide angle 2D beam splitter design based on vector diffraction theory”. *Optics Communications* 434, pp. 28–35, 2019. DOI: 10.1016/j.optcom.2018.10.026. (See pp. 3, 68, 76).

[72] G. Zhang, Q. Song, L. Wei, and X. Yin. “Inverse optimization for designing wide angle diffractive optical element”. In: *Eleventh International Conference on Information Optics and Photonics (CIOP 2019)*. Ed. by H. Wang. December 2019. SPIE, Dec. 2019. P. 117. DOI: 10.1117/12.2548299. (See pp. 3, 76).

[73] Z. Liu, Z. Zhu, and W. Cai. “Topological encoding method for data-driven photonics inverse design”. *Opt. Express* 28, pp. 4825–4835, 2020. DOI: 10.1364/OE.387504. (See pp. 3, 76).

[74] C. M. Lalau-Keraly, S. Bhargava, O. D. Miller, and E. Yablonovitch. “Adjoint shape optimization applied to electromagnetic design”. *Optics Express* 21, p. 21693, 2013. DOI: 10.1364/OE.21.021693. (See pp. 3, 4).

[75] A. Y. Piggott, J. Lu, K. G. Lagoudakis, J. Petykiewicz, T. M. Babinec, and J. Vučković. “Inverse design and demonstration of a compact and broadband on-chip wavelength demultiplexer”. *Nature Photonics* 9, pp. 374–377, 2015. DOI: 10.1038/nphoton.2015.69. (See p. 3).

[76] T. Hughes, G. Veronis, K. P. Wootton, R. Joel England, and S. Fan. "Method for computationally efficient design of dielectric laser accelerator structures". *Optics Express* 25, p. 15414, 2017. DOI: 10.1364/OE.25.015414. (See p. 3).

[77] J. Wang, Y. Shi, T. Hughes, Z. Zhao, and S. Fan. "Adjoint-based optimization of active nanophotonic devices". *Optics Express* 26, p. 3236, 2018. DOI: 10.1364/OE.26.003236. (See p. 3).

[78] Z. Lin, B. Groever, F. Capasso, A. W. Rodriguez, and M. Lončar. "Topology-Optimized Multilayered Metaoptics". *Physical Review Applied* 9, pp. 1–6, 2018. DOI: 10.1103/PhysRevApplied.9.044030. (See p. 3).

[79] A. Michaels and E. Yablonovitch. "Leveraging continuous material averaging for inverse electromagnetic design". *Optics Express* 26, p. 31717, 2018. DOI: 10.1364/oe.26.031717. (See p. 3).

[80] O. Ripoll, V. Kettunen, and H. P. Herzig. "Review of iterative Fourier-transform algorithms for beam shaping applications". *Optical Engineering* 43, 2004. DOI: 10.1117/1.1804543. (See p. 4).

[81] A. Vasara, M. R. Taghizadeh, J. Turunen, J. Westerholm, E. Noponen, H. Ichikawa, et al. "Binary surface-relief gratings for array illumination in digitaloptics". *Appl. Opt.* 31, pp. 3320–3336, 1992. DOI: 10.1364/AO.31.003320. (See pp. 4, 29).

[82] U. Levy, E. Marom, and D. Mendlovic. "Thin element approximation for the analysis of blazed gratings: Simplified model and validity limits". *Optics Communications* 229, pp. 11–21, 2004. DOI: 10.1016/j.optcom.2003.10.017. (See p. 4).

[83] D. F.-. Brosseau, F. Lacroix, M. H. Ayliffe, E. Bernier, B. Robertson, F. A. P. Tooley, et al. "Design, implementation, and characterization of a kinematically aligned, cascaded spot- array generator for a modulator-based free-space optical interconnect". *Applied Optics* 39, p. 733, 2000. DOI: 10.1364/ao.39.000733. (See p. 4).

[84] J. E. Jureller, H. Y. Kim, and N. F. Scherer. "Stochastic scanning multiphoton multifocal microscopy". *Optics Express* 14, p. 3406, 2006. DOI: 10.1364/oe.14.003406. (See p. 4).

[85] Z. Chen, B. Mc Larney, J. Rebling, X. L. Deán-Ben, Q. Zhou, S. Gottschalk, et al. "High-Speed Large-Field Multifocal Illumination Fluorescence Microscopy". *Laser and Photonics Reviews* 1900070, pp. 1–8, 2019. DOI: 10.1002/lpor.201900070. (See p. 4).

[86] M. Bauer, D. Grießbach, A. Hermerschmidt, S. Krüger, M. Scheele, and A. Schischmanow. "Geometrical camera calibration with diffractive optical elements". *Optics Express* 16, p. 20241, 2008. DOI: 10.1364/OE.16.020241. (See p. 4).

[87] F. Wang, Z. Zhang, R. Wang, X. Zeng, X. Yang, S. Lv, et al. "Distortion measurement of optical system using phase diffractive beam splitter". *Opt. Expr.* 27, pp. 29803–29816, 2019. DOI: 10.1364/OE.27.029803. (See p. 4).

[88] R. Vandenhouten, A. Hermerschmidt, and R. Fiebelkorn. “Design and quality metrics of point patterns for coded structured light illumination with diffractive optical elements in optical 3D sensors”. In: *Digital Optical Technologies 2017*. Ed. by B. C. Kress and P. Schelkens. Vol. 10335. International Society for Optics and Photonics. SPIE, 2017. Pp. 264–276. DOI: 10.1117/12.2270248. (See p. 4).

[89] A. J. Devaney and G. C. Sherman. “Plane-Wave Representations for Scalar Wave Fields”. *SIAM Review* 15, pp. 765–786, 1973. DOI: 10.1137/1015096. (See p. 10).

[90] H. Kogelnik and T. Li. “Laser Beams and Resonators”. *Applied Optics*, 1966. DOI: 10.1364/ao.5.001550. (See p. 13).

[91] A. Taflove, S. C. Hagness, and M. Piket-May. “Computational Electromagnetics: The Finite-Difference Time-Domain Method”. In: *The Electrical Engineering Handbook*. Elsevier, 2005. Pp. 629–670. DOI: 10.1016/B978-012170960-0/50046-3. (See p. 20).

[92] H. Ichikawa. “Electromagnetic analysis of diffraction gratings by the finite-difference time-domain method”. *Journal of the Optical Society of America A* 15, p. 152, 1998. DOI: 10.1364/JOSAA.15.000152. (See p. 20).

[93] T. Delort and D. Maystre. “Finite-element method for gratings”. *Journal of the Optical Society of America A* 10, p. 2592, 1993. DOI: 10.1364/JOSAA.10.002592. (See p. 20).

[94] S. Burger, J. Pomplun, and F. Schmidt. In: “Finite Element Methods for Computational Nano-optics”. B. Bhushan, ed. Pp. 837–843. Dordrecht: Springer Netherlands, 2012. DOI: 10.1007/978-90-481-9751-4_17. (See p. 20).

[95] A. C. Polycarpou. “Introduction to the Finite Element Method in Electromagnetics”. *Synthesis Lectures on Computational Electromagnetics* 1, pp. 1–126, 2006. DOI: 10.2200/S00019ED1V01Y200604CEM004. (See p. 20).

[96] W. Shin. “3D Finite-Difference Frequency-Domain Method for Plasmonics and Nanophotonics”. PhD thesis. 2013. (See p. 20).

[97] W. C. Gibson. *The Method of Moments in Electromagnetics*. Chapman and Hall/CRC, July 2014. DOI: 10.1201/b17119. (See p. 20).

[98] K. Hwi, P. Junghyun, and L. Byoungho. *Fourier Modal Method and Its Applications in Computational Nanophotonics*. CRC Press, Dec. 2017. DOI: 10.1201/b11710. (See p. 20).

[99] P. Lalanne. “Improved formulation of the coupled-wave method for two-dimensional gratings”. *Journal of the Optical Society of America A* 14, p. 1592, 1997. DOI: 10.1364/JOSAA.14.001592. (See p. 20).

[100] K. Knop. “Rigorous diffraction theory for transmission phase gratings with deep rectangular grooves”. *Journal of the Optical Society of America* 68, p. 1206, 1978. DOI: 10.1364/JOSA.68.001206. (See p. 20).

[101] S. Peng, T. Tamir, and H. Bertoni. “Theory of periodic dielect waveguides”. *IEEE Transactions on Microwave Theory and Techniques* 23, pp. 123–133, 1975. DOI: 10.1109/TMTT.1975.1128513. (See p. 20).

[102] C. B. Burckhardt. “Diffraction of a Plane Wave at a Sinusoidally Stratified Dielectric Grating”. *Journal of the Optical Society of America* 56, p. 1502, 1966. DOI: 10.1364/JOSA.56.001502. (See p. 20).

[103] F. G. Kaspar. “Diffraction by thick, periodically stratified gratings with complex dielectric constant”. *Journal of the Optical Society of America* 63, p. 37, 1973. DOI: 10.1364/JOSA.63.000037. (See p. 20).

[104] K.-H. Brenner. “Aspects for calculating local absorption with the rigorous coupled-wave method”. *Optics Express* 18, p. 10369, 2010. DOI: 10.1364/OE.18.010369. (See p. 20).

[105] F. Montiel and M. Neviere. “Differential theory of gratings: extension to deep gratings of arbitrary profile and permittivity through the R-matrix propagation algorithm”. *J. Opt. Soc. Am. A* 11, pp. 3241–3250, 1994. DOI: 10.1364/JOSAA.11.003241. (See p. 20).

[106] M. Nevière and E. Popov. *Light Propagation in Periodic Media*. CRC Press, Oct. 2018. DOI: 10.1201/9781482275919. (See p. 20).

[107] .“On the dynamical theory of gratings”. *Proceedings of the Royal Society of London. Series A, Containing Papers of a Mathematical and Physical Character* 79, pp. 399–416, 1907. DOI: 10.1098/rspa.1907.0051. (See p. 20).

[108] L. Li and C. W. Haggans. “Convergence of the coupled-wave method for metallic lamellar diffraction gratings”. *Journal of the Optical Society of America A* 10, p. 1184, 1993. DOI: 10.1364/JOSAA.10.001184. (See p. 20).

[109] L. Li. “Formulation and comparison of two recursive matrix algorithms for modeling layered diffraction gratings”. *Journal of the Optical Society of America A* 13, p. 1024, 1996. DOI: 10.1364/JOSAA.13.001024. (See pp. 20, 27).

[110] G. Granet and B. Guizal. “Efficient implementation of the coupled-wave method for metallic lamellar gratings in TM polarization”. *Journal of the Optical Society of America A*, 1996. DOI: 10.1364/josaa.13.001019. (See p. 20).

[111] L. Li. “Use of Fourier series in the analysis of discontinuous periodic structures”. *Journal of the Optical Society of America A* 13, p. 1870, 1996. DOI: 10.1364/JOSAA.13.001870. (See pp. 20, 23).

[112] E. Popov and M. Nevière. “Grating theory: new equations in Fourier space leading to fast converging results for TM polarization”. *Journal of the Optical Society of America A* 17, p. 1773, 2000. DOI: 10.1364/JOSAA.17.001773. (See p. 20).

[113] R. Redheffer. In: “Difference equations and functional equations in transmission-line theory”. McGraw-Hill, 1961. (See p. 27).

[114] Eberhart and Yuhui Shi. “Particle swarm optimization: developments, applications and resources”. In: *Proceedings of the 2001 Congress on Evolutionary Computation (IEEE Cat. No.01TH8546)*. Vol. 1. May 2001. 81–86 vol. 1. DOI: 10.1109/CEC.2001.934374. (See pp. 29, 32).

[115] O. Bryngdahl. "Optical map transformations". *Optics Communications*, 1974. DOI: 10.1016/0030-4018(74)90046-7. (See p. 29).

[116] J. Turunen, A. Vasara, and J. Westerholm. "Kinoform Phase Relief Synthesis: A Stochastic Method". *Optical Engineering* 28, p. 281162, 1989. (See p. 29).

[117] S. Kirkpatrick, C. D. Gelatt, and M. P. Vecchi. "Optimization by Simulated Annealing". *Science* 220, pp. 671–680, 1983. DOI: 10.1126/science.220.4598.671. (See p. 29).

[118] M. S. Kim and C. C. Guest. "Simulated annealing algorithm for binary phase only filters in pattern classification". *Applied Optics* 29, p. 1203, 1990. DOI: 10.1364/AO.29.001203. (See p. 29).

[119] D. Whitley. "A genetic algorithm tutorial". *Statistics and Computing* 4, pp. 65–85, 1994. DOI: 10.1007/BF00175354. (See pp. 29, 32).

[120] U. Triltsch, A. Phataralaoha, S. Büttgenbach, D. Straube, and H. .-.-J. Franke. "Optimization of lithographic masks using genetic algorithms". *Analog Integrated Circuits and Signal Processing* 48, pp. 49–56, 2006. DOI: 10.1007/s10470-006-8121-x. (See p. 29).

[121] J. W. Rinne, S. Gupta, and P. Wiltzius. "Inverse design for phase mask lithography". *Opt. Express* 16, pp. 663–670, 2008. DOI: 10.1364/OE.16.000663. (See p. 29).

[122] A. Håkansson, H. T. Miyazaki, and J. Sánchez-Dehesa. "Inverse Design for Full Control of Spontaneous Emission Using Light Emitting Scattering Optical Elements". *Phys. Rev. Lett.* 96, p. 153902, 2006. DOI: 10.1103/PhysRevLett.96.153902. (See p. 29).

[123] F. Poletti, V. Finazzi, T. M. Monro, N. G. R. Broderick, V. Tse, and D. J. Richardson. "Inverse design and fabrication tolerances of ultra-flattened dispersion holey fibers". *Opt. Express* 13, pp. 3728–3736, 2005. DOI: 10.1364/OPEX.13.003728. (See p. 29).

[124] J. R. Fienup. "Iterative Method Applied To Image Reconstruction And To Computer-Generated Holograms". *Optical Engineering* 19, pp. 297–305, 1980. DOI: 10.1117/12.7972513. (See p. 30).

[125] J. R. Fienup. "Phase retrieval algorithms: a comparison". *Appl. Opt.* 21, pp. 2758–2769, 1982. DOI: 10.1364/AO.21.002758. (See p. 30).

[126] F. Wyrowski and O. Bryngdahl. "Digital holography as part of diffractive optics". *Reports on Progress in Physics* 54, pp. 1481–1571, 1991. DOI: 10.1088/0034-4885/54/12/001. (See p. 30).

[127] F. Wyrowski. "Design theory of diffractive elements in the paraxial domain". *Journal of the Optical Society of America A* 10, p. 1553, 1993. DOI: 10.1364/JOSAA.10.001553. (See p. 30).

[128] S. Ruder. "An overview of gradient descent optimization algorithms". *CoRR* abs/1609.04747, 2016. (See p. 33).

[129] R. H. Byrd, P. Lu, J. Nocedal, and C. Zhu. "A Limited Memory Algorithm for Bound Constrained Optimization". *SIAM Journal on Scientific Computing* 16, pp. 1190–1208, 1995. DOI: 10.1137/0916069. (See pp. 33, 42, 61).

[130] C. Zhu, R. H. Byrd, P. Lu, and J. Nocedal. "Algorithm 778: L-BFGS-B: Fortran subroutines for large-scale bound-constrained optimization". *ACM Transactions on Mathematical Software* 23, pp. 550–560, 1997. DOI: 10.1145/279232.279236. (See pp. 33, 42, 61).

[131] R. Brereton. "Steepest Ascent, Steepest Descent, and Gradient Methods". In: *Comprehensive Chemometrics*. Elsevier, 2009. Pp. 577–590. DOI: 10.1016/B978-044452701-1.00037-5. (See p. 33).

[132] H. B. Curry. "The method of steepest descent for non-linear minimization problems". *Quarterly of Applied Mathematics* 2, pp. 258–261, 1944. DOI: 10.1090/qam/10667. (See p. 33).

[133] M. Hestenes and E. Stiefel. "Methods of conjugate gradients for solving linear systems". *Journal of Research of the National Bureau of Standards* 49, p. 409, 1952. DOI: 10.6028/jres.049.044. (See p. 33).

[134] T. Vallius, M. Kuittinen, J. Turunen, and V. Kettunen. "Step-transition perturbation approach for pixel-structured nonparaxial diffractive elements". *Journal of the Optical Society of America A* 19, p. 1129, 2002. DOI: 10.1364/JOSAA.19.001129. (See pp. 35, 36).

[135] V. Kettunen, M. Kuittinen, and J. Turunen. "Effects of abrupt surface-profile transitions in nonparaxial diffractive optics". *Journal of the Optical Society of America A* 18, p. 1257, 2001. DOI: 10.1364/JOSAA.18.001257. (See p. 36).

[136] T. Vallius, V. Kettunen, M. Kuittinen, and J. Turunen. "Step-discontinuity approach for non-paraxial diffractive optics". *Journal of Modern Optics* 48, pp. 1195–1210, 2001. DOI: 10.1080/09500340010028080. (See p. 36).

[137] R. L. Easton. *Fourier Methods in Imaging*. John Wiley & Sons, Ltd, Apr. 2010. DOI: 10.1002/9780470660102. (See p. 38).

[138] J.-P. Hugonin and P. Lalanne. *Reticolo software for grating analysis*. Institut d'Optique, Orsay, France, 2005. (See p. 48).

[139] A. Lavrinenko, J. Lægsgaard, N. Gregersen, F. Schmidt, and T. Søndergaard. *Numerical Methods in Photonics*. Optical Sciences and Applications of Light. Taylor & Francis, 2014. (See p. 59).

[140] X. Qian and O. Sigmund. "Topological design of electromechanical actuators with robustness toward over- and under-etching". *Computer Methods in Applied Mechanics and Engineering* 253, pp. 237–251, 2013. DOI: 10.1016/j.cma.2012.08.020. (See p. 60).

[141] F. Wang, B. S. Lazarov, and O. Sigmund. "On projection methods, convergence and robust formulations in topology optimization". *Structural and Multidisciplinary Optimization* 43, pp. 767–784, 2011. DOI: 10.1007/s00158-010-0602-y. (See pp. 60, 61).

[142] R. L. Morrison. "Symmetries that simplify the design of spot array phase gratings". *Journal of the Optical Society of America A* 9, p. 464, 1992. DOI: 10.1364/JOSAA.9.000464. (See p. 63).

[144] D. C. Kim, A. Hermerschmidt, P. Dyachenko, and T. Scharf. “Adjoint-based Optimization for Diffractive Beam-Splitters”. In: *2019 24th Microoptics Conference (MOC)*. Nov. 2019. Pp. 266–267. DOI: 10.23919/MOC46630.2019.8982782. (See p. 83).

[145] M. Symeonidis, D. C. Kim, A. Hermerschmidt, M.-S. Kim, and T. Scharf. “Diffractive optical elements investigation in the phase domain”. In: *Optical Components and Materials XVI*. Ed. by M. J. Digonnet and S. Jiang. February. SPIE, Feb. 2019. P. 72. DOI: 10.1117/12.2509668. (See p. 83).

[146] D. C. Kim, P. Dyachenko, A. Hermerschmidt, and T. Scharf. *Gradient-based optimization with step-transition perturbation approach for 1D binary diffractive beam splitters*. Paper presented at European Optical Society Biennial Meeting 2018, Delft, Netherlands. 2018, Oct. (See p. 84).

# Dong Cheon **Kim**

*Route du Bois 53, 1024 Ecublens, Switzerland*

(+41) 78 237 73 37 | dong.kim@epfl.ch | dongcheonkim

## Summary


I'm a physics researcher with computational expertise and nano-fabrication and interested in Diffractive optics and optimization. Currently, I am PhD candidate in EPFL's photonics doctoral program, my work is focused on developing algorithmic design strategies for diffractive optical elements. When I'm not doing science, you can find me football, skiing, or cooking with various cuisines.


## Education

**Ecole Polytechnique Fédérale de Lausanne (EPFL)** — *Lausanne, Switzerland*

Ph.D in Photonics (in progress) — *Mar. 2017 - Dec. 2020(expected)*

- Research advisor : Dr. Toralf Scharf

**Ecole Polytechnique** — *Palaiseau, France*

Master of Engineering and Technologies — *Feb. 2015 - Dec. 2016*

- Master Thesis at CEA-Leti, Grenoble, France

**Kyung Hee University** — *Seoul, South Korea*

Master of Engineering — *Mar. 2014 - Feb. 2015*

- Dual master's degree program
- GPA: 4.34/4.5

Bachelor of Science in Information Display — *Mar. 2008 - Feb. 2014*

- GPA: 4.0/4.5

## Skills

| | |
|---|---|
| **Platforms** | Matlab, Mathematica, Python, LaTeX, C++, COMSOL, VirturalLab Fusion, Zemax, Synopsys |
| **Characterizations** | UV-Visible Spectroscopy, Photoluminescence, Scanning electron microscopy (SEM), Atomic force microscopy (AFM) |
| **Fabrications** | Photo-lithography, Sputtering, Thermal Evaporation, Wet-etching, Spin-coating |
| **Languages** | Korean (native), English (advanced), French (intermediate), German (basic) |

## Experience

**Nanopthonics and metrology laboratory, EPFL** — *Lausanne, Switzerland*

Research assistant — *Mar. 2017 - Present*

- Proposed theoretical model and corresponding optical elements creating wide-angle beam array for 3-D sensing
- Worked on teaching assistant for bachelor courses (e.g., Optical engineering)
- Wrote scientific journal and respond to referee's revision requests

**Holoeye Photonics AG** — *Berlin, Germany*

Early Stage Reseacher — *Sep. 2017 - Aug. 2019*

- Invented stable and fast design algorithm to create diffractive optical elements
- Investigated and benkmarked commercial optimization tools for diffractive optical elements

**Laboratory of memory components, CEA-Leti** — *Grenoble, France*

Research internship — *Mar. 2016 - Aug. 2016*

- Simulated electro-magentic characteristics of metal-insulator interface

**Laboratory of thin film and interface physics, Ecole Polytechnique** — *Palaiseau, France*

Research internship — *Mar. 2015 - Aug. 2015*

- Researched on fabrication and characterization of perovskite solar-cell

**Advanced display research center, Kyung Hee University** *Seoul, South Korea*

Research assistant *Mar. 2014 - Feb. 2015*

- Helped develop a printing process of thin film solar-cell
- Operated and maintained of vacuum chambers in the ISO 5 cleanroom

## Extracurricular Activity

**NOLOSS project** *European union*

Ph.D Fellow *Mar. 2017 - Mar. 2020*

- Consortium of 4 academic partners and 9 industrial partners across Europe funded by the European Commission
- Worked at the industry partner (Holoeye Phohtonics AG)

**Science school, EKC 2018** *Glasgow, U.K*

Tutor *Aug. 2018*

- Organized the science school for youth in Europe during Europe-Korea conference on science and technology 2018.
- Supervised and helped participates to promote the scientific and technological knowledge and enjoy the program

**Dale Carnegie leadership training** *Seoul, South Korea*

Coach *Jun. 2013*

- Participated in the Dale Carnegie course as a coach who demonstrates the activities and encourages the participants
- Developed a take-charge attitude to initiate confidence and enthusiasm
- Learned and trained skills of communicating effectively and human relations

**Republic of Korea Army** *South Korea*

Honorable discharge *Mar. 2010 - Dec. 2011*

- Fulfilled the military service in Repulbic of Korea Army's communications and IT department

## Awards & Grants

2017 **Fellowship**, Marie Sklodowska-Curie Actions *European Union*

2014 **Scholarship**, Kyung Hee Graduate School *South Korea*

2008 **Scholarship**, National Science & Technology Scholarship *South Korea*

## Selected Courseworks

**Photonics** Deep learning for optical imaging, Image optics, Optical design, Liquid crystal display optics, Optoelectronics

**Micro-engineering** Physics of photovoltaic, Nanomaterials and electronic applications, Semiconductors and device Organic light emitting diode, Integrated circuits

**Physics** Solid State Physics, Electromagnetics, Experimental physics